Politecnico di Torino

in collaboration with

SnT - Interdisciplinary Centre for Security, Reliability and Trust

Master Thesis in Space Engineering

Herschel Resupply Mission

Orbit/Attitude control for rendezvous & docking at the Herschel Space Observatory

Supervisors:

Prof. Lorenzo Casalino
Dr. Davide Menzio

Candidate:

Andrea Siena

For all mankind

Abstract

In future, space exploration will need to rely on In Situ Resource Utilization *(ISRU)* in order to recover in part or fully of necessary resources to extend its missions. For the Moon and, in future, for Mars colonization, relying on in - situ resources is a necessary step to become independent from the Earth. The possibility to produce resources on the Moon is advantageous for those missions that are too far from the Earth to be resupplied. At the SnT Research Centre, the Luxembourg Space Agency is supporting a feasibility study to assess the benefit of on - orbit servicing exploiting lunar resources for the Herschel Space Observatory. The observatory ended its operations in 2013 as a consequence of depleting its coolant. The thesis deals with the orbit/attitude control of a cargo spacecraft *(S/C)*, travelling from the Moon to Herschel, to refill it of the missing coolant. Assuming a linearized three – body dynamics, a rendezvous *(RdV)* trajectory was designed. Considering Herschel's orientation on its orbit, pointing its sunshield in the direction of the Sun, and the need to access to Herschel rear panel to perform the resupply, an approach along the negative x - axis is envisaged, where the primaries lie. A multiple shooting technique has been used to perform a flanking manoeuvre. Moreover both a slew and a tracking manoeuvre have been tested for the attitude control to ensure minimum thrusting error of the cargo spacecraft and a continuous visibility of Herschel. Further works foresee adapting the final approach to align better with the corridor for the docking. Furthermore, the attitude control will try to compensate for the angular rates induced by the movement of the robotic arms.

Sommario

Nel futuro, l'esplorazione spaziale necessiterà dell'utilizzo di risorse in situ per recuperare parzialmente o totalmente i beni necessari ad estendere le missioni. Per la Luna ed, in seguito, per la colonizzazione di Marte, fare affidamento alle risorse in situ è uno step necessario per diventare indipendenti dalla Terra. La possibilità di produrre risorse sulla Luna è vantaggiosa per quelle missioni che risultano essere troppo lontane dalla Terra per quanto riguarda il rifornimento. Al centro di ricerca SnT, l'Agenzia Spaziale Lussemburghese sta supportando uno studio di fattibilità per stabilire il beneficio del rifornimento in orbita sfruttando le risorse lunari per l'Osservatorio Spaziale Herschel. L'osservatorio terminò le sue operazioni nel 2013 a causa dell'esaurimento del refrigerante. La tesi si occupa del controllo orbitale e d'assetto di un veicolo di trasporto spaziale che viaggia dalla Luna ad Herschel per rifornirlo del refrigerante stesso. Assumendo una dinamica dei tre corpi linearizzata una traiettoria di rendezvous è stata definita. Considerando l'orientamento di Herschel sulla sua orbita, con lo scudo solare rivolto verso il Sole, e la necessità di avvicinarsi dal pannello posteriore per effettuare il rifornimento, è stato previsto un approccio lungo la direzione negativa dell'asse x, dove giacciono i corpi primari. Una tecnica di multiple shooting è stata utilizzata per effettuare una manovra di aggiramento. Inoltre una manovra di slew ad una di tracking sono state testate per il controllo d'assetto per assicurare un minimo errore di thrusting ed una continua visibilità di Herschel. Ulteriori studi prevedono l'adattamento dell'avvicinamento finale per allinearsi meglio con il corridoio di approccio per l'attracco. Peraltro, il controllo d'assetto cercherà di compensare la rotazione angolare indotta dal movimento dei bracci robotici.

Ringraziamenti

Come prima cosa vorrei ringraziare il professore Lorenzo Casalino per aver accettato di svolgere il ruolo di relatore ed avermi seguito in questo percorso. Un grande e profondo grazie va anche al mio supervisore, il dottor Davide Menzio, al dottorando Ahmed Mahfouz e a tutto il dipartimento di automazione del centro di ricerca SnT dell'università del Lussemburgo, capeggiato dal professor Holger Voos, per avermi fatto da guida, insegnato come portare avanti un lavoro di ricerca e consigliato durante tutto il periodo di lavoro.
Ringrazio mamma e papà per essere stati con me ogni sera al telefono ad ascoltarmi e spronarmi per superare le giornate più difficili e per avermi permesso di svolgere questo percorso facendo più sacrifici di tutti, per avermi educato ed insegnato a resistere alle difficoltà e rialzarmi quando cado. Ringrazio mio fratello Riccardo per essere stato quella vocina che mi faceva vedere i problemi più grossi come semplici ostacoli da saltare piuttosto che muri. Ringrazio la mia famiglia e in particolare mia zia Valeria per i preziosi consigli su come affrontare questo percorso dall'inizio alla fine.
Ringrazio le mie amiche di sempre Irma e Serena per esserci state in ogni singolo secondo ed avere ascoltato le mie preoccupazioni senza mai stancarsi, per avermi aiutato a crescere come la persona che voglio essere, non quella che devo essere, per levigare tutti i miei difetti e credere nelle mie capacità come fossero una seconda famiglia. Ringrazio Alessandra, Andrea, Babdi, Deborah, Emanuele, Ivonne, Marcello, Monica e tutti gli amici di Torino per avermi fatto ridere, piangere, cantare e suonare in compagnia in tutti questi anni universitari. Ringrazio Francesco, Gianluca, Giovanni e Sabino per tutte le ore passate tra i banchi e le videochiamate a confrontarci sui progetti di gruppo. Ringrazio Elisa, Fiorenzo, Gaetano, Gioele, tutti gli amici di Foggia e tutte le brevi, ma intense conoscenze lussemburghesi. Un grazie spaciale va a Giacomo, collega di tesi, per il tempo passato in ufficio e le traiettorie generate insieme.
Infine ringrazio le mie squadre di pallavolo lussemburghesi e torinesi per avermi accolto e dato una valvola di sfogo quando più ne avevo bisogno.

Table of Contents

List of Tables XI

List of Figures XII

Acronyms XVI

1 Introduction 1

1.1 Thesis outline . . . 7

2 Background 9

2.1 Circular Restricted 3 - Body Problem . . . 9

2.2 Herschel overview . . . 12

2.2.1 The ESA mission . . . 12

2.2.2 Platform and payload . . . 13

2.2.3 Herschel Resupply Mission . . . 15

2.3 Lunar infrastructure . . . 16

2.3.1 Moon base . . . 18

2.3.2 Lunar Gateway . . . 19

2.3.3 Lunar resources . . . 20

2.4 Spice . . . 24

3 Trajectory Design 27

4 Linearization 39

4.1 Taylor series expansion . . . 39

4.2 Hill dynamics . . . 42

4.3 Simulations - Close Proximity Operations . . . 43

4.4 Simulations - Whole Transfer . . . 47

5 Rendezvous 51

5.1 Optimization . . . 54

5.1.1 Optimization variables . . . 54

5.1.2 Constraints . . . 54
5.1.3 Cost function . . . 54
5.1.4 Boundaries . . . 55
5.1.5 Initial Conditions . . . 55
5.1.6 Results . . . 56

6 Attitude Control 65
6.1 Attitude model . . . 66
6.1.1 Dynamics & Kinematics . . . 67
6.1.2 Controller . . . 68
6.1.3 Actuator . . . 68
6.2 Simulations . . . 71
6.2.1 Slew Manoeuvre . . . 71
6.2.2 Tracking Manoeuvre . . . 72
6.2.3 Slew + Tracking . . . 77

7 Conclusions & Future Work 81

A SPICE Kernels 83

B Quaternions Fundamentals 85

C Simulink Blocks 87

List of Tables

1.1 Sun - Earth L_2 missions 6

2.1 Platform 15
2.2 Average concentrations of solar wind volatiles in the lunar regolith where the quoted errors reflect the range ($\pm$ refers to one standard deviation) of values found at different sampling locations 23

3.1 Details of the feasible transfers in terms of angular starting position from the Lissajous, ΔV at Herschel, time of flight, angle and axis of rotation of the direction of the perturbation given 38

5.1 Details on the time of flight, impulses magnitude and errors for the fast rendezvous 58
5.2 Magnitude of the three impulses and total time of flight of the rendezvous phase 59
5.3 Position and Velocity errors from the desired point 60
5.4 Time of flight and magnitudes of the impulses given during each rendezvous manoeuvre 63

6.1 PD gains and Schmidt Trigger parameters 71

List of Figures

2.1 Restricted Three - Body Problem 11
2.2 Sun - Earth Lagrangian points 12
2.3 The Horse and the Dragon 13
2.4 *Left:* Herschel with PLM, cryostat, FPUs, telescope, and SVM. *Middle:* close-up of the PLM. *Right:* Preparation for acoustic testing 14
2.5 Cargo S/C. *Up*: Payload module. *Down*: Service module 17
2.6 Artist concept of the Artemis Base Camp 19
2.7 Full Gateway with Orion approaching 21
2.8 Capture Tent concept for sublimating ice 24
2.9 *Left*: regolith before oxygen extraction. *Right*: regolith after oxygen extraction 25

3.1 Variation of astronomical distance, tangential velocity and angular motion over one revolution 28
3.2 Sun Inertial Frame as extracted from SPICE 29
3.3 Earth - Moon barycenter, Herschel, L_2, Moon in the synodic reference frame 30
3.4 Herschel's orbit projection on the y - z synodic plane 31
3.5 Synodic frame with cylinder for the Moon's orbit 31
3.6 Herschel's orbit interpolation 32
3.7 Transfers obtained perturbing Herschel with a ΔV given in the velocity direction. *Left*: y - z plane. *Right*: y - x plane 33
3.8 Overview of the transfers found reaching the Moon. One for each considered departing point of the orbit 36
3.9 Summary of ΔV and time of flight of each transfer w.r.t. the angular position of the starting point on the Lissajous orbit 36

4.1 Trajectory requiring the lowest impulse at Herschel to reach the Moon among the set 44
4.2 First 5 km from Herschel of the trajectory requiring the lowest impulse to reach the Moon 45

4.3 Position and velocity errors for the CPO trajectory propagated with the linear dynamics obtained via Taylor series expansion 46
4.4 Position and velocity errors for the CPO trajectory propagated with the Hill's dynamics 46
4.5 Comparison between Taylor and Hill's approximations for position and velocity in CPO 48
4.6 Position and velocity linearization errors for the whole trajectory . . 48
4.7 Position and velocity linearization errors for the whole trajectory for different number of resolution of the linear system 49

5.1 Rendezvous regions 52
5.2 Herschel body frame 52
5.3 Optimization Scheme 53
5.4 Volume in which the middle point has been bounded for the optimization 55
5.5 Rendezvous at Herschel on the left side of the Lissajous orbit requiring a high ΔV 57
5.6 Trajectory reaching Herschel on the right side of the Lissajous orbit 57
5.7 Fast Rendezvous 58
5.8 Rendezvous phase 59
5.9 Rendezvous phase - zoom at final approach on the x - z plane . . . 60
5.10 Rendezvous phase - zoom at final approach on the x - y plane . . . 61
5.11 Manifold of rendezvous trajectories lasting from 5 to 10 hours . . . 62
5.12 Velocity error per rendezvous manoeuvre at the final point 62

6.1 Gravity gradient torques on the uncontrolled cargo spacecraft during the rendezvous phase 67
6.2 Projection on the x - y body plane of the cargo spacecraft with the thrusters location 69
6.3 Projection on the y - z body plane of the cargo spacecraft with the thrusters location 70
6.4 Slew manoeuvre 73
6.5 Slew manoeuvre zoomed in the first 4 minutes 73
6.6 Quaternion error, quaternions and angular error starting the control 1500 seconds before reaching the middle point 74
6.7 Control and applied torques starting the control 1500 seconds before reaching the middle point 74
6.8 Control and applied torques during the slew manoeuvre 75
6.9 Tracking manoeuvre 75
6.10 Tracking manoeuvre zoomed in the first 4 minutes 76
6.11 Control and applied torques during the tracking manoeuvre 76

6.12 Quaternion error, quaternions and angular error for the whole manoeuvre . . . 77
6.13 Angular velocity error and angular velocity for the whole manoeuvre 78
6.14 Control and applied torque for the whole manoeuvre . . . 78
6.15 Peaks in the control torques needed to re - align the cargo S/C after the switch in the desired attitude . . . 79

C.1 Simulink model for the attitude control . . . 87
C.2 Rigid body rotational dynamics block . . . 87
C.3 Euler's equations block . . . 88
C.4 Poisson's equations block . . . 88
C.5 Error - quaternion feedback control block . . . 88
C.6 Control block . . . 89
C.7 Actuator block with Schmidt Trigger . . . 89
C.8 Quaternions to angular velocity block . . . 89
C.9 Desired quaternion generation block. The orbit subsystem propagates the RdV manoeuvre, the rotate INERTIAL2BODY subsystem turns the desired attitude vector from the inertial to the body frame and the vec2quat function turns the vector into a quaternion . . . 90

Acronyms

3BP 3 - Body Problem

AI Artificial Intelligence

AS Approach Sphere

ARGON Advanced Rendezvous demonstration using Global positioning system and Optical Navigation

ARIEL Atmospheric Remote - sensing Infrared Exoplanet Large - survey

ATHENA Advanced Telescope for High Energy Astrophysics

AVANTI Autonomous Vision Approach Navigation and Target Identification

BoL Beginning of Life

CNN Convolutional Neural Networks

CoM Center of Mass

CPO Close Proximity Operations

CR3BP Circular Restricted 3 - Body Problem

CVV Cryostat Vacuum Vessel

DoF Degree of Freedom

EM Earth - Moon

EML$_2$ Earth - Moon L_2 Lagrange point

EoL End of Life

ER3BP Elliptical Restricted 3 - Body Problem

ESA European Space Agency

FoV Field of View

FPU Focal Plane Unit

GAIA Global Astrometric Interferometer for Astrophysics

GG Gravity Gradient

GNC Guidance, Navigation & Control

GPS Global Positioning System

HRSM Herschel ReSupply Mission

HSO Herschel Space Observatory

I - HAB International Habitat Module

IRSIS International Rendezvous System Interoperability Standards

ISS International Space Station

IXO International X - ray Observatory

JWST James Webb Space Telescope

KOS Keep Out Sphere

LCA Limit Cycle Amplitude

LEO Low Earth Orbit

LiteBIRD Lite B - mode polarization and Inflation from cosmos background Radiation Detection

LoS Line of Sight

LUVOIR Large UltraViolet Optical Infrared Surveyor

MIB Minimum Impulse Bit

NASA National Aeronautics and Space Administration

ON Optical Navigation

PLATO PLAnetary Transits and Oscillations

PLM PayLoad Module

PRISMA Prototype Research Instruments and Space Mission Advancement

R3BP Restricted 3 - Body Problem

RdV RendezVous

RS Rendezvous Sphere

ROE Relative Orbital Elements

RTG Radioisotope Thermoelectric Generator

S/C Spacecraft

SE Sun - Earth

SEL_2 Sun - Earth L_2 Lagrange point

SK Station - Keeping

SO Space Observatory

SRG Spectrum Roentgen Gamma

ST Schmidt Trigger

SVM SerVice Module

TPF Terrestrial Planet Finder

WMAP Wilkinson Microwave Anisotropy Probe

Chapter 1

Introduction

The current space industry is making great strides in the technological development to reach better and better achievements in the space missions. The focus of the last years is placed on reducing costs and time of the activities to be performed and automatize many of the processes involved. Rendezvous and docking missions fall in this category. The first successful RdV mission was the GEMINI mission [1], accomplished in 1966, when the spacecraft docked to an Agena Target vehicle specifically adapted for this demonstration. From that day on, more and more missions involved RdV between two or more S/Cs for different reasons, such as bringing supplies or crew members to an existing station, debris removal or performing on - orbit activities like refueling, repairing or assembling of new structures.

The Orbital Express programme [2] developed by the National Aeronautics and Space Administration *(NASA)* had the goal of demonstrating and validating key technologies just for these purposes. It consisted of two spacecrafts performing rendezvous and capture in order to replace batteries or refueling propellant. These tasks were accomplished through the use of an autonomous rendezvous and capture system, integrated with a software that dealt with relative range and attitude determination basing on imaging data, as well as a sensor that provided measurements of bearing, range and relative attitude at mid - range distance. The sensor was a combination of video and lasers fired asynchronously at two different wavelengths and successively reflected. The images obtained were then subtracted to remove extraneous light sources and make the corner cubes of the target visible in order to compute its relative position and attitude with respect to the sensor itself.

However, the outcome of the mission remained confidential, making it difficult to assess what has been achieved, but another mission, called Proba - 3 [3], carried out by the European Space Agency *(ESA)*, presents more insights on the topic. The mission aimed at improving formation flying technologies performing solar coronography and formation manoeuvre demonstrations between two S/Cs that would be inserted in a high elliptical orbit as a single rigid body and then separated. Then, formation flying operations would begin with the acquisition of the relative state in terms of position, velocity and attitude. The S/Cs would use visual based sensors to perform operations in the nominal orbit, including breaking of the formation at perigee, due to the excessive perturbations, and a successive acquisition at apogee through two direct transfer manoeuvres. Since the inter - satellite distance between the two vehicles is much less than the orbital radius a linearized model was used for the propagation of the relative trajectory. It consisted of a safe orbit at the end of the separation drift that was then shrunk down, allowing safety and simplicity of the manoeuvre. The simulation results demonstrated the possibility of achieving a two year mission with a ΔV around 10 m/s for the main operations and a ΔV among 100 and 250 mm/s for station - keeping *(SK)* manoeuvres.

In the field of orbital rendezvous, many information can also be found in Gaias and D'Amico's works. They carried out several demonstrations in Low Earth Orbit *(LEO)* to validate autonomous systems based on angles - only measurements to perform far - to mid - range distance RdV activities to a non - cooperative target. ARGON [4] and AVANTI [5, 6, 7] have been conducted during the extended phases of the PRISMA mission for this purpose, obtaining remarkable results. The first demonstration performed an efficient and safe RdV from 30 km to a final hold point of 3 km from the target. The navigation accuracy was combined with a guidance strategy based on relative eccentricity/inclination vector separation method to enhance angles - only navigation. The performances were evaluated exploiting relative GPS techniques that allowed to compare different relative navigation sensors. Turned out that the accuracy of angles - only relative navigation is strictly dependent on the adopted camera hardware, resolution and bias calibration and because of limitations due to the servicer telemetry data - rate budget, the mean along - track separation remained affected by errors larger than what is achievable with a lidar or radar technology.

The second experiment differs from the latter by its complexity since no target tracking data were available and the orbit was lower than ARGON's one, leading to a stronger drag perturbation and the presence of eclipses. The absence of GPS reference data implied that the trajectory could be recognized only through the images taken by the on - board camera and this led to some problems when the distance between chaser and target became larger, since the camera recognized hot spot instead of the target itself. The problem was easily solved using the number of pixels of the image affected by the body, since an hot spot only affects one pixel while the target is spread over many of them. This second test focused on the line of sight measurements and their processing by the dynamical filter and showed that longitudinal errors decrease as the servicer approached the target. In particular at far - range distance the orbit determination exhibited large along -

track errors, up to a few hundred meters, but still being able to accurately estimate the shape of the elliptical relative motion. At mid - range distance the relative trajectory was successfully determined during all approaches until the chaser was 50 m away from the target. For both the experiments Relative Orbital Elements *(ROE)* were considered instead of relative position and velocity, in order to get a deeper geometrical insight on the trajectory. Moreover the Earth oblateness due to the J_2 effect was easily included and the usage of the relative orbit determination and manoeuvre planning software for operators was simplified, since they could deal with slowly varying parameters. Moreover D'Amico obtained important results in the design of a vision - based architecture for pose estimation during close proximity operations *(CPO)* by testing it with the space imagery collected during the aforementioned PRISMA mission. The work aimed at determining the position of the target center of mass and orientation of principal axes with respect to the camera frame of the chaser. Exploiting a weak gradient determination technique to distinguish the S/C in the foreground from the background, and fusing it with the Sobel operator and Hough transform to extract the line segments of smaller parts, D'Amico [8] achieved a higher precision detection, if compared to the previous works, and a reduction of computational time of an order of magnitude. Subsequently he validated the use of Convolutional Neural Networks *(CNN)* with small amounts of Gaussian noise proving that, with the right noise model, CNN have a good potential for pose determination using actual space images. The previous experiments, in fact, were carried out using synthetic imagery, so a test on real images was necessary to state their effective performance. These tasks are vital for on - orbit servicing missions, especially in case of detumbled spacecrafts, since their kinematic is unknown before the launch and no trajectory planning can be done.

All these missions rely on Guidance, Navigation & Control *(GNC)* algorithms and Optical Navigation *(ON)* techniques to be fully automated and allow a more flexible manoeuvre design. Rebordão [9] presented an overall description of ON modes and methods in his work. The main idea is to use objects with reliable ephemerides as beacons, enabling the navigation subsystem to locate the S/C in space and plan subsequent manoeuvres to accomplish a mission. The camera provides line of sight *(LoS)* estimates to the GNC system, which combines them with the output of other sensors to generate the best possible estimation of the state of the S/C. In this perspective, Llop [10] defined an effective GNC system for Earth - Moon *(EM)* libration point missions that reduced operational and ground infrastructure costs. He started with optical measurements of the Moon to perform the state estimation and then used a Target Point control technique to compute correction manoeuvres. The algorithm was tested on a EML_2 Halo orbit and eventually S/C requirements were derived.

In some missions, after rendezvous , docking is performed, in order to join two spacecrafts together. Docking operations have been carried out in the Orbital Express mission [11] through the use of a manipulator system designed to perform autonomous capture of a free - flying satellite and on - orbit replaceable units transfer. The main component of the system was a 6 - Degree of Freedom *(DoF)* rotary joint robotic arm with its control software running on a Manipulator Control Unit. The latter commanded the arm to acquire the visual target using a camera, a frame - grabber and a pose algorithm. Once the acquisition was successful the S/C carrying the arm was put in a drift mode and track & capture operations of the target began. A 6 - DoF estimate of position and orientation was provided and the tip of the arm was commanded towards that point. The arm control law kept the target centered in the camera field of view while reducing range, lateral and angular offsets to it, achieving the suitable relative speed for the capture. This was performed through a grapple fixture, equipped to the target, consisting of a cylindrical body designed to link to the arm end.

A similar approach has been used for the e.Deorbit mission [12], developed by ESA to address the problem of active debris removal. The mission focuses on Envisat, an Earth remote sensing spacecraft which contributed to climate monitoring and research. His heavy mass and low orbit made it hazardous for collisions with active satellites or for uncontrolled re - entry in the Earth atmosphere, so the mission considered a chaser equipped with a GNC system to rendezvous with the target using LoS sensors at far - range distance and adding range measurements and pose estimations at mid - and close - range distance to ultimately dock with Envisat exploiting a robotic arm. The arm grasped a launch adapter ring, adjusting the chaser orientation w.r.t. the target and providing structural rigidity during the deorbiting manoeuvres. A torque controller specified through generalized dynamics impedance prevented the arm from pushing the target away during the clamping sequence. The particularity of this arm laid in its 7 - DoF instead of the usual 6 needed for the task. This redundancy enabled a motion in the null space of the robotic arm that had to be taken into account by the control law.

The work done in this thesis differs from the previous ones because it's adapted to the case of the Herschel Space Observatory *(HSO)*. Herschel is located around the second Sun - Earth Lagrangian point (SEL_2), revolving around it in a Lissajous orbit. Its lifetime was connected to the amount of coolant available in the cryostat to keep the payloads at their operating temperature. Once the observatory ran out of coolant its operations ended. The Herschel ReSupply Mission *(HRSM)* envisaged, aims at refueling the cryostat with the coolant extracted on the Moon. Unlike ARGON, AVANTI, Proba - 3 and Orbital Express, though, Herschel is not into a LEO orbit, thus, in the first part of the thesis, a three - body dynamics is implemented and linearized in order to assess a feasible baseline trajectory on which the Close Proximity Operations are performed to rendezvous in compliance with the constraints of the mission.

Trajectory design in three - body systems has been assessed from many points of view. Due to their uniqueness, in fact, Lagrangian (or libration) points became the focus of many missions, most of the which accomplished in order to settle space telescopes or other observatories like Herschel in a region of space where the equilibrium of forces would allow a reduction of disturbances. Just the last one regarded the James Webb Space Telescope, inserted into a Halo orbit around L_2, but many more have been carried out, as table 1.1 shows. Folta [13], for example, used a dynamical system approach to get reference solutions in the multi - body problem for libration orbits and then used the associated stable and unstable manifolds to generate transfer trajectories towards them. He also found different optimized strategies assessing ΔV and time for both high and low thrust manoeuvres. Both EM and SE systems though, require manoeuvres with high ΔV cost and short optimal spacing. Moreover, adding constraints like performing a RdV manoeuvre, lowers the number of possible transfers and forces the timing to be planned well in advance [14].
Furthermore, during CPO, the dynamics and the subsequent algorithms used can be linearized gaining simplicity and remaining reliable. The Linear Relative targeting algorithm examined by Mand [15], turned out to have a good accuracy and precision by taking into account multi - body effects. Therefore three trajectories were developed in his work to exploit the algorithm for RdV operations near SEL_2. After the trajectory definition, it is important to consider the random aspects of the system and this led to a type of stochastic navigation realized directly perturbing the true states by an error bound. Once this was done, requirements for each trajectory could be derived and the algorithm was chosen according to the mission to be carried out.

Mission	Launch Date	Disposal Date	Purpose	Orbit [km]
Launched				
WMAP	30 June 2001	Oct 2010	Cosmic Microwave Background	Lissajous
Planck	14 May 2009	23 Oct 2013	Cosmic Background Radiation Field	Lissajous
Herschel	14 May 2009	17 June 2013	Far Infrared Telescope	Lissajous 800000
GAIA	19 Dec 2013	31 Dec 2025	Astrometry	Lissajous 340000 x 90000
SRG	13 July 2019	-	Supermassive Black Hole Detection	Halo
JWST	25 Dec 2021	2026	Deep Space Observatory	Halo
Cancelled				
Eddington	-	-	Asteroseismology	Lissajous
Darwin	-	-	Earth-like Planet Detection	-
TPF	-	-	Planet Detection	Halo
Constellation-X IXO	-	-	X - Ray Astronomy	Halo 700000
Programmed				
Euclid	July - Dec 2022	TBD	Dark matter analysis	Halo
PLATO	2026	TBD	Earth-like planet detection	Quasi-Halo
LiteBIRD	2028	TBD	Gravitational waves investigation	Lissajous
ARIEL	2029	TBD	Exoplanets Observation	Large Halo
Comet Interceptor	2029	TBD	Comet Flyby	Halo
ATHENA	2031	TBD	X-Ray Astronomy	Large Halo
LUVOIR	2039	TBD	Space Telescope	-

Table 1.1: Sun - Earth L_2 missions

1.1 Thesis outline

After a swift introduction of the problem and the literature found to support the studies, an overview of the Lunar infrastructure and the environment in which the cargo will operate is presented in Chapter 2. It will also give more details on the mission, describing the first phase of the HRSM with insights on lunar mining activities carried out for the purpose of the mission itself. Following, in Chapter 3, the methodology used for the trajectory design is presented and successively the linearization process is described in Chapter 4. Chapter 5 deals with the close proximity operations presenting the method used for the rendezvous phase. Chapter 6 features the assumptions made for a first assessment of an attitude control technique of the spacecraft during the rendezvous phase. In the end, Chapter 7, draws the conclusions on the results obtained and presents the future iterations of the mission.

Chapter 2

Background

This chapter will deal with the background information needed for the development of the work, starting with the mathematics of the 3 - body problem and moving forward with the description of the observatory in object. Furthermore, the lunar infrastructure and the mining activities assumed for the fulfillment of the mission are described. Finally, the SPICE toolkit used is described.

2.1 Circular Restricted 3 - Body Problem

In the most general case, a body in space undergoes many different forces: gravitational pull, drag, solar pressure, magnetic forces. These forces may vary according to the position of the body and affect its motion, so they must be taken into account to study the evolution of its trajectory, especially if accurate operations have to be carried out. Newton's second law of motion for a moving body with fixed mass suggests that the acceleration $\boldsymbol{a}$ depends on the sum of the forces $\boldsymbol{F}$ acting on the moving body of mass m:

$$\boldsymbol{a} = \frac{\boldsymbol{F}}{m}$$

In the case of a non - inertial spinning reference frame, fictitious terms appear:

$$\ddot{\boldsymbol{r}} + 2\,\boldsymbol{\omega} \times \dot{\boldsymbol{r}} + \boldsymbol{\omega} \times (\boldsymbol{\omega} \times \boldsymbol{r}) + \dot{\boldsymbol{\omega}} \times \boldsymbol{r} = \frac{\boldsymbol{F}}{m} \tag{2.1}$$

where the first term on the left of the equal is the relative inertial acceleration, the second is the Coriolis acceleration, the third is the centripetal acceleration and the last is the Euler acceleration. On the right there is the sum of all the disturbances acting on the body divided by its mass. These disturbances, however, have different magnitude and some of them are negligible in particular conditions. Considering a

S/C moving in the Solar System, the main acting force is the gravitational pull of the closest planets and the Sun, unless the body is really close to the Sun itself. In this case the solar pressure could be significant. For the HRSM the cargo S/C will be travelling between the Moon and the SEL_2 point, thus the main disturbances will be constituted by the Sun, the Earth and the Moon's gravitational pull, whereas the attraction of all the other bodies of the Solar System can be neglected [16]. Furthermore, if the effects of the Moon are included in those of the Earth, the two can be accounted as a single body, obtaining the so called 3 - Body Problem [16]. Considering only the main bodies allows easier calculations that would be too computationally expensive in the most general case and would add unnecessary complexity to the problem. The first main body would be the Sun (m_1), the second the system composed of the Earth and the Moon (m_2) and the third would be the spacecraft (m). Moreover, assuming that $m_1 > m_2 >> m$, the problem addressed becomes the Restricted 3 - Body Problem *(R3BP)*, where the mass of the S/C is neglected. Another simplification is made considering the Earth's orbit as almost circular ($e = 0.0167$) meaning that the eccentricity can be considered null and added at a later time to test its impact on the dynamics. The R3BP becomes the Circular Restricted 3 - Body Problem *(CR3BP)*. Moreover, the equations of motion are usually expressed in a rotating frame, called synodic, centered on the barycenter of the system and rotating with the angular rate of the second primary. Figure 2.1 shows the two frames, inertial and synodic, and the three bodies involved. The total mass can be defined as $M = m_1 + m_2$ and used to normalize the single masses. By doing so the parameter $\mu = m_2/M$ is defined, so that the barycenter of the 3 - body system has coordinates $B = [\mu R \ \ 0 \ \ 0]^{\mathrm{T}}$ w.r.t. the inertial system placed on the main primary, where R is the distance between the two primaries. Accordingly, the coordinates of the three bodies in the synodic frame will be the following:

$$m_1 = \begin{Bmatrix} -\mu R \\ 0 \\ 0 \end{Bmatrix} \qquad m_2 = \begin{Bmatrix} R(1-\mu) \\ 0 \\ 0 \end{Bmatrix} \qquad m = \begin{Bmatrix} x \\ y \\ z \end{Bmatrix} \tag{2.2}$$

The normalization helps expressing the equations in such a way that they are dependent only on one parameter, μ. Therefore the other variables are also normalized, the time relative to the mean motion of the system $\omega = \sqrt{\frac{GM}{R^3}}$, with $G = 6.67 \cdot 10^{-11}$ being the gravitational constant, and the distances relative to R. By doing so, the dimensionless non - linear equations of motion are obtained [16]:

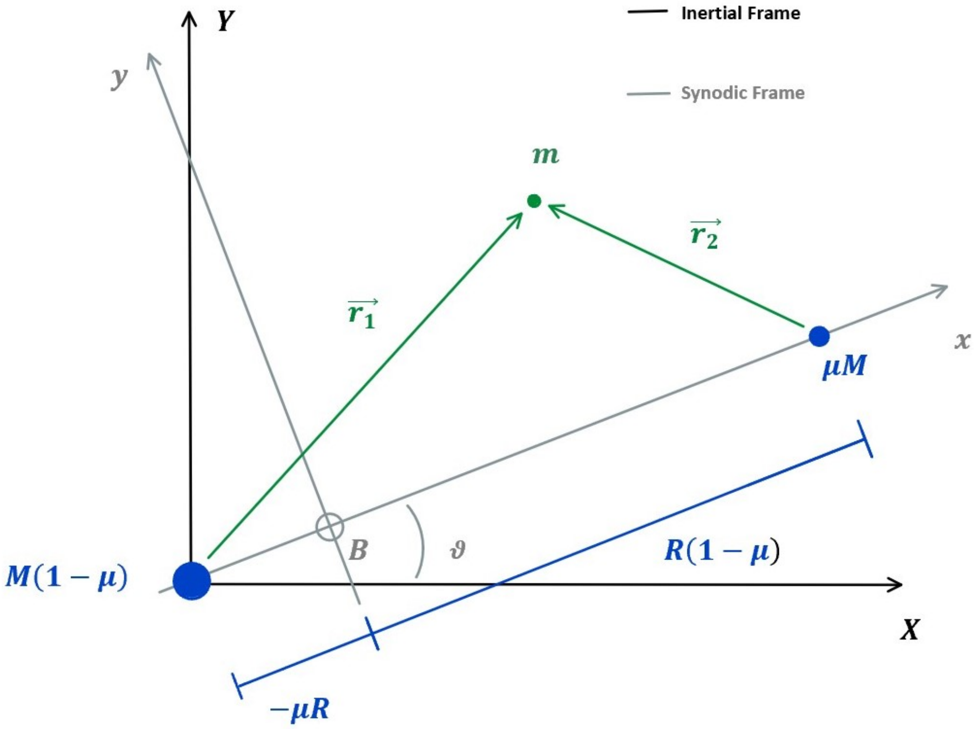

Figure 2.1: Restricted Three - Body Problem

$$
\begin{aligned}
\ddot{x} &= 2\dot{y} + x - \frac{(1-\mu)(x+\mu)}{r_1^3} - \frac{\mu(x-1+\mu)}{r_2^3} \\
\ddot{y} &= -2\dot{x} + y - \frac{(1-\mu)y}{r_1^3} - \frac{\mu y}{r_2^3} \\
\ddot{z} &= -\frac{(1-\mu)z}{r_1^3} - \frac{\mu z}{r_2^3}
\end{aligned}
\tag{2.3}
$$

with r_1 and r_2 being the distances of the S/C respectively from the first and the second primary such that

$$
r_1 = \sqrt{(x+\mu)^2 + y^2 + z^2} \qquad\qquad r_2 = \sqrt{(x-1+\mu)^2 + y^2 + z^2} \tag{2.4}
$$

In 3 - body systems there are five peculiar regions of space called Lagrangian points where the gravitational and centrifugal forces balance each other. These points are named $L_{1\rightarrow 5}$ and can be collinear or equilateral. The first three are collinear points, which means that they are positioned along the x - axis of the system, where the primaries lie. In particular $L_{1,2}$ are located at $[\mp\sqrt[3]{\frac{\mu}{3}} \;\; 0 \;\; 0]^T$ w.r.t. m_2, while L_3 is located at $[-1 \;\; 0 \;\; 0]^T$ w.r.t. m_1. The last two are equilateral points, which means that they are located on the x - y plane, which is the plane of motion of the primaries if the inclination of their orbit is neglected. In particular $L_{4,5}$ are located at $[\frac{1}{2}-\mu \;\; \pm\frac{\sqrt{3}}{2} \;\; 0]^T$ w.r.t. the origin of the reference frame. Figure 2.2 shows the position in space of the five points. As stated before Herschel orbits around the second of these points, which is then the focus of the thesis.

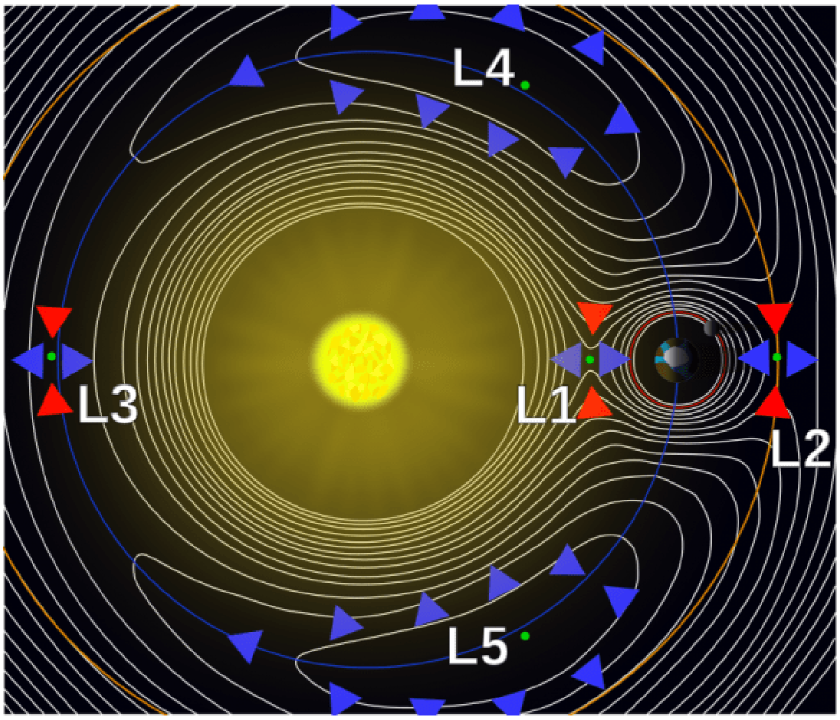

Figure 2.2: Sun - Earth Lagrangian points

2.2 Herschel overview

2.2.1 The ESA mission

HERSCHEL [17] is a space observatory dedicated to collecting measurements in the far - infrared band of the spectrum. Its main goal is to study the chemical composition of planetary systems, observe the birth of new galaxies and stars and follow their evolution. Herschel was launched on 14 May 2009 from Kourou space centre by an Arian V ECA launcher, shared with another telescope, PLANCK. It was put in a 800 000 km Lissajous orbit around Sun - Earth L_2, beyond the Earth -

Moon system, far away from heat and light emissions of our planet, performing every month SK manoeuvres of not more than 1 m/s per year to maintain the orbit due to its instability. Lissajous orbits, in fact, are not naturally stable because the frequency of the motion in the plane is different from the out - of - plane one. An Halo orbit is a specific Lissajous for which this condition is satisfied, but the mission analysis didn't find any advantage in trying to achieve this configuration for the candidate mission. The nominal orbit was chosen among a manifold of different orbits such that its stable manifold touched the best Ariane launch conditions [18]. The mission lifetime was determined by the predicted cryostat service life of 3.5 years. Among the many observations made, Herschel discovered massive objects that were then found out to be the progenitors of the known galaxies, formed at a very early cosmic epoch. The cosmic dust created during the birth of new stars made them shine brightly in the infrared band and allowed Herschel to observe them. In figure 2.3 a pair of these galaxies stand out from the darkness of the universe. They were informally dubbed *The Horse and the Dragon* and are roughly as massive as our Milky Way.

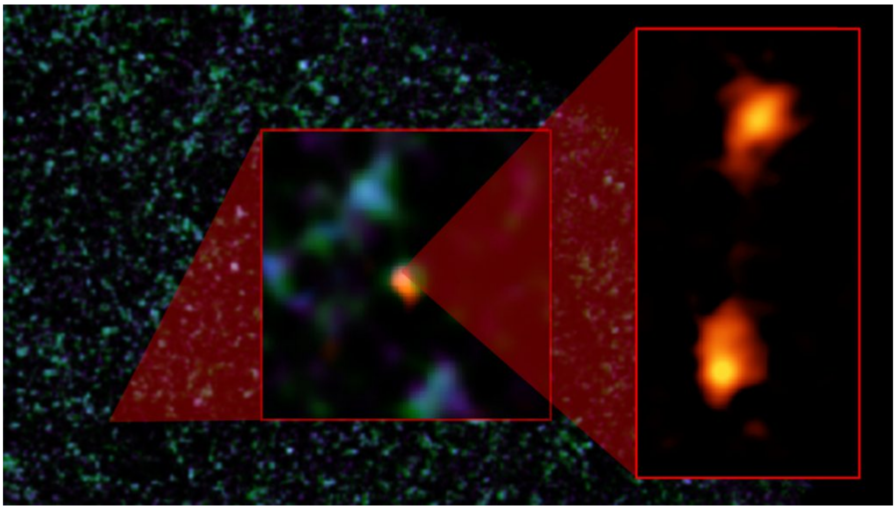

Figure 2.3: The Horse and the Dragon

2.2.2 Platform and payload

Herschel has a modular design [19] consisting of the payload module *(PLM)* supporting the telescope, the sunshade/sunshield and the service module *(SVM)*. The PLM is dominated by the cryostat vacuum vessel *(CVV)* from which the helium tank is suspended, surrounded by three vapour - cooled shields to minimise parasitic heat loads. The optical bench with the three instrument focal plane units (FPUs) is supported on top of the tank. A phase separator allows a continuous evaporation of the liquid into cold gas. The FPUs and their detectors are kept at their required temperatures by thermal connections to the liquid cryogen in the tank and to pick - off points at different temperatures of the piping that carries the helium gas from the tank, which is routed around the instruments for this purpose, and to the vapour - cooled shields for eventual release into free space. The SVM houses "warm" payload electronics on four of its eight panels and provides the necessary infrastructure for the satellite such as power, attitude and orbit control, the on - board data handling and command execution, communications, and safety monitoring. It also provides a thermally controlled environment, which is critical for some of the instrument units. Finally, the SVM also provides mechanical support for the PLM, the sunshield/sunshade, a thermal shield to thermally decouple the PLM from the SVM, and it ensures the main mechanical load path during the launch. Figure 2.4 shows, on the left, the payload module with all the components mentioned above, in the middle, a close - up image on the payload module itself displaying the optical bench for the FPUs on top of the helium tank and the focal plane cover with the vapour - cooled shields inside the CVV and finally, on the right, the telescope being prepared for acoustic testing in the Large European Acoustic Facility *(LEAF)* in the European Space and Technology Test Centre.

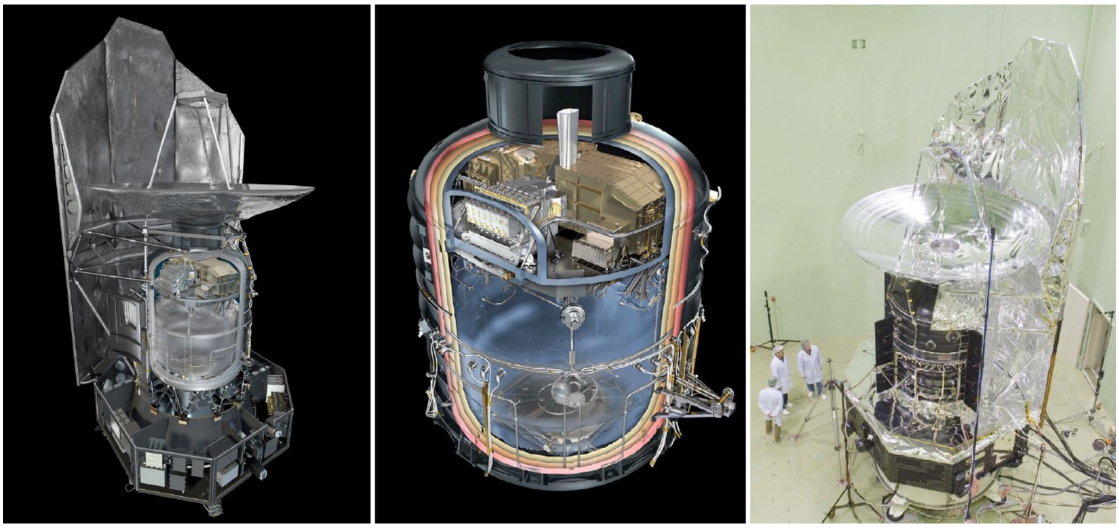

Figure 2.4: *Left:* Herschel with PLM, cryostat, FPUs, telescope, and SVM. *Middle:* close-up of the PLM. *Right:* Preparation for acoustic testing

Table 2.1 provides the physical features of the observatory.

The three payloads carried are:

- **HIFI** (Heterodyne Instrument for the Far Infrared), a very high resolution heterodyne spectrometer;

Wet mass (helium)	3400 (335) kg
Dry mass	2800 kg
Height	7.5 m
Cross section	4×4 m
Wavelength	$[55 \div 672]$ μm
Telescope	Cassegrain
Mirrors	3.5 m primary 0.3 m secondary

Table 2.1: Platform

- **PACS** (Photodetector Array Camera and Spectrometer), an imaging photometer and an integral field line spectrometer;
- **SPIRE** (Spectral and Photometric Imaging Receiver), another imaging photometer and an imaging Fourier transform spectrometer.

2.2.3 Herschel Resupply Mission

The Herschel resupply mission was envisaged to put the Space Observatory *(SO)* back on line. Moreover, the same logic can be exploited for every SO located in a similar orbit.
The depletion of coolant prevented the payloads to be cooled down to their operating temperatures. Indeed, simply by functioning, they emit radiations heating up the environment around them and disturbing the measurements. The HRSM aims at refueling the cryostat with the coolant extracted on the Moon. In order to do so, the regolith of the lunar surface will be turned into Helium (^{4}He) and placed into an adapted cargo S/C. The latter will then leave the Moon and embark on an interplanetary trajectory towards SEL$_2$ until it is close enough to start the CPO phase, including rendezvous and final approach. During these phases attitude control will assure that the cargo spacecraft would be oriented in compliance with the constraints of the mission. At the end of the docking phase, when the two vehicles are connected, the refueling starts. During this operation, the new system will be controlled so that Herschel would remain on its orbit after the refueling is completed. The end of the mission foresees a safe receding phase of the cargo S/C and its return on the Moon, to be reloaded of coolant and prepared to depart again when another refueling of the observatory is needed.
The first phase of the HRSM had the objective of identifying and comparing alternative designs of the cargo spacecraft and lay foundations for the next phase.

The key point of the mission is the refueling of Herschel's cryostat by storing and delivering 3000L of ^{4}He. This is one of the drivers of the mission, together with the possibility of reusing the cargo S/C and performing multiple ascent/descent manoeuvres from/to the Moon's surface. In order to do this a lunar infrastructure and space mining technologies are assumed to be available and all the subsystems selection have been done according to this assumption. Three power systems were considered: Solar Arrays, RTG and Fuel Cells. Considering that the Moon is a huge source of Hydrogen and Oxygen, fuel cells have been selected as power source, and the same logic has been used for the propulsion system, choosing a liquid propellant rocket instead of a solid or an electric one. For the landing mechanism an honeycomb crushable has been selected for its simplicity and the possibility of manufacturing it on the Moon, whereas the same couldn't be done for an electromechanical or metal bellow shock mechanism. Once these decisions have been taken, the cargo module is designed in a modular architecture: a payload module on the top and a service module below it. The former houses the cryostat, the docking arm, the transfer line and the close proximity sensors, but it can be changed according to the mission. On the other hand, the latter, which is the S/C bus, houses all the other subsystems including the propellant tanks, the avionics and the fuel cells (see figure 2.5 for a representative concept of the cargo S/C). The other task fulfilled during the phase I of the mission is the transfer of Helium from Caroline[1] to Herschel, where the majority of constraints on the attitude are established in order to prevent the sun rays from warming the coolant during the cruise.

The constraints to ensure the feasibility of this mission are:

- Approaching Herschel from the rear side, where the docking port is located, since the front is covered by the sunshield protecting the structure from the heat of the sun rays;
- Not crossing of the orbits for safety reasons;
- Maximum a month of journey to reach Herschel.

2.3 Lunar infrastructure

Last time mankind went to the Moon, technologies in our possession were not modern enough to allow the development of a proper lunar infrastructure that would

[1] The cargo S/C was named after William Herschel's sister because she assisted him in designing and maintaining the first Herschel telescope

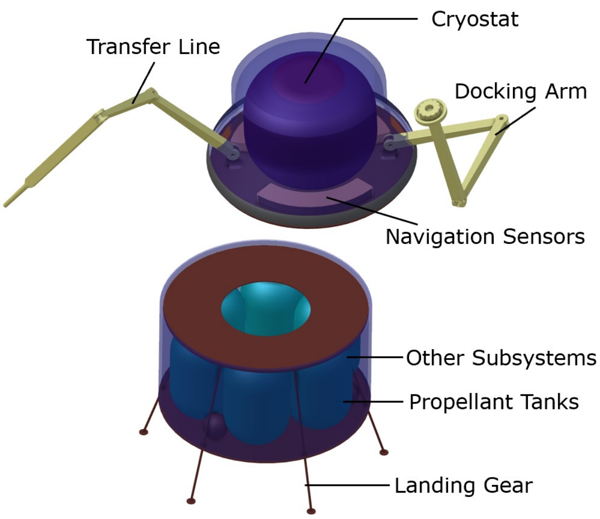

Figure 2.5: Cargo S/C. *Up*: Payload module. *Down*: Service module

assist astronauts in performing multiple activities on the lunar surface. Nowadays, after countless steps forward in the engineering field, mankind is much more ready to establish an almost autonomous settlement where scientists can carry on their studies in a new environment, opening up new windows for space missions. Plans have been made by NASA and ESA in collaboration with other space agencies all around the globe to realize a safe and sustainable establishment on the Moon to make new steps in the field of space exploration and conduct different kinds of mission, such as the HRSM described in this paper. These plans ended up in a three phased mission, named ARTEMIS[2] [20] that has the objective of landing the first woman and the next man onto the lunar surface and exploit lunar resources to prepare mankind for the exploration of Mars. The services the infrastructure will be provided with, may range from power systems to communication and navigation systems, from mobility systems to life support systems for human habitats. They should be able to support human missions from a few days to several months with minimal maintenance and replacement of parts, exploiting directly the in loco resources, such as water from ice deposits or oxygen and other metals from lunar regolith, in order to reduce mass and cost of the shipments coming from Earth. Thanks to the experience and expertise gained over the years, many features of the infrastructure conceived for the Artemis mission were taken from the International Space Station *(ISS)*, which also presented comparable environmental challenges to

[2]Artemis was the name of the Greek goddess of the Moon, twin sister of Apollo, who gave the name to the first human mission to the Moon

those that the lunar outpost will have to face. The realization of a human outpost on the Moon is a very difficult task, therefore many actors will be involved to accomplish this goal, from the launching system, that will take the astronauts in a lunar orbit, to the landing system and a lunar camp that will let them live on the surface of the Moon.

2.3.1 Moon base

In order to manufacture raw materials from the lunar soil and exploit them in different fields, astronauts need to reside on the Moon for long periods of time in order to bring forth their activities. This means that the Moon base has to assure them protection from the rough external environment and allow them to rest and work in the best possible conditions. The ISS had already satisfied these requirements, hence many elements of its structure were adapted to the lunar environment. On the Moon, in fact, the atmosphere is significantly weaker than that of the Earth and the negligible magnetic field doesn't provide enough protection from radiations (mainly solar wind, solar flares' particles and galactic cosmic rays). Moreover the temperature ranges from + 120 °C in daylight to - 180 °C at night and the dust from the lunar regolith is made up of sharp and glassy grains. All these characteristics make life on the Moon really dangerous for living beings, but also represent unique engineering challenges since most electronic devices and S/C subsystems would soon become inoperative under these conditions. That's why the construction of a proper settlement is studied carefully, in order to assure that the mission can be carried out in the safest way possible. The result of the studies brought to the so called 'Artemis Base Camp' [20] composed of three main mission elements: the Lunar Terrain Vehicle *(LTV)*, the habitable mobility platform and the foundation surface habitat, as shown in figure 2.6. The former is an unpressurized rover used to transport astronauts around the site, the second is a pressurized rover that can enable long duration trips away from the camp and the latter is a habitat that will accommodate four crew members on the lunar surface. Because of the difficult conditions listed before, these habitats should provide a radiation and micrometeorite resilient structure providing an internal environment similar to the ISS one, with airlocks able to remove the lunar dust particles and provide an acceptable air quality w.r.t. the air quality index with particulate matter 2.5 and 10 at 35 μg/m^3 and 150 μg/m^3 over a 24 - hour exposure period. In order to reduce the environmental threats and produce low cost systems, it is recommended to locate the outpost in places with extended periods of illumination, like the Shackleton crater at the Lunar South Pole. Such locations provide near constant access to sunlight which will enable continuous solar power generation that will reduce the cost of power production and storage systems. The temperatures are also constant which avoids the need for complex thermal management systems.

Moreover, the nearby permanently shadowed craters may contain large amounts of water - ice deposits that can be extracted and exploited for different purposes [21].

Figure 2.6: Artist concept of the Artemis Base Camp

2.3.2 Lunar Gateway

The Gateway [22] will be an outpost orbiting the Moon to provide vital support for a long term human return to the lunar surface, as well as being a staging point for deep space exploration and robotic lunar missions. It will be a destination for astronaut expeditions and science investigations, as well as a port for deep space transportation such as landers en route to the lunar surface or spacecraft embarking to destinations beyond the Moon. Astronauts will be supposed to reach the Gateway with the Orion spacecraft, as shown in figure 2.7. NASA has focused the Gateway development on four initial critical elements:

- The Power and Propulsion Element *(PPE)*, a high-power, 60 - kilowatt solar electric propulsion module that will provide power, high - rate communications, attitude control, and orbital transfer capabilities for the Gateway. It will also be able to provide accommodation for science and technology demonstration payloads. For the Artemis mission Maxar Technologies of Westminster, Colorado, has been chosen to develop, build, and support an in - space demonstration of this element, managed out of NASA's Glenn Research Center in Ohio;
- The Habitation And Logistics Outpost *(HALO)*, the initial crew cabin for astronauts visiting the Gateway. Its primary purpose will be the provision

of basic life support needs for the visiting astronauts after their arrival in the Orion S/C and the preparation of their trip to the lunar surface. It will provide command, control, and data handling capabilities, energy storage, power distribution, thermal control, communications and tracking capabilities, as well as environmental control and life support systems to augment Orion potentialities and support crew members. It will also have several docking ports for visiting vehicles and future modules, as well as space for science and stowage. The HALO is being developed by Northrop Grumman and is managed out of NASA's Johnson Space Center in Houston;

- The International Habitat Module *(I - HAB)* will be the second habitable module complementing habitability functions such as life support systems, a crew sleeping area, a gallery with food warmers, water dispenser, dining areas and additional research facilities. The structure will be composed of a radial docking port for the crew and a scientific airlock accommodation as well as a back up docking port for the lunar human lander module and an axial port for the Orion S/C;
- Deep Space Logistics, aimed at preparing astronauts for missions to the lunar surface, since they will need deliveries of critical pressurized and unpressurized cargo, science experiments and supplies, such as sample collection materials and other items or food and water for crew. SpaceX has been selected as the first U.S. commercial provider under the Gateway Logistics Services contract to deliver cargo and other supplies to the Gateway.

The Gateway will be designed to operate autonomously and its closeness to the Moon will allow astronauts to live outside the Van Allen radiation belts and perform multiple ascent/descent missions from/to the lunar surface without wasting too many resources. ESA's radiation investigation, the European Radiation Sensors Array *(ERSA)*, will help provide an understanding of how to keep astronauts safe by monitoring the radiation exposure in the Gateway's orbit. On the other hand NASA's space weather instrument suite, the Heliophysics Environmental and Radiation Measurement Experiment Suite *(HERMES)*, will monitor solar particles and solar wind. The Gateway will also pay a crucial role in Mars mission simulations at the Moon, for which a four - person crew traveling mission to the Gateway is envisioned, followed by a multi - month stay aboard to simulate the outbound trip to Mars and a descent to the Moon base for two of the four members of the crew to explore the lunar surface with the habitable mobility platform [20].

2.3.3 Lunar resources

Every element in the periodic table is likely to be found on the Moon at some level, just as they do on Earth. Whether or not these resources will be exploitable

Figure 2.7: Full Gateway with Orion approaching

depends on their amount, location and physic state, since not all of them are worth mining from an economical point of view. The choice of which elements is better looking for could be carried on by considering the use they could have in future missions on the Moon or elsewhere in the Solar System. This is what is called In - Situ Resource Utilization, the idea thanks to which there would be no need of sending supplies from the Earth anymore, decreasing the cost of a space mission or making it possible if it wasn't before. Part of them could also be sent on the Earth's surface to contribute directly to the global economy and avoid consuming all the resources of the planet. Studying the geology of the Moon, it was found out that the lunar surface is divided into two main geological units: the ancient, light - coloured lunar highlands and the darker, circular lunar mare. The highlands are composed predominantly of Ca, Al, Si and O, whereas the maria are richer in Mg, Fe and Ti [23]. Furthermore the entire lunar surface is covered in an unconsolidated layer of regolith, a dust with sharp, glassy grains of size between 45 μm and 100 μm characterized by extremely low electrical and dielectric losses allowing electrostatic charges to build up under UV radiation [21]. The regolith has been produced by billions of years of meteorite and micro - meteorite impacts and it's several meters thick in mare regions and just 10 or a little bit more metres thick in the highlands areas. The uppermost few centimeters have a very powdery consistency, making the activity of astronauts during moonwalks very dangerous and annoying, while, by a depth of 30 cm, it becomes more compacted. Besides the general regolith, there are some deposits of volcanic ash produced by volcanic eruptions in some mare areas. Such deposits are identified via remote - sensing techniques as they have a low albedo, appearing darker to the camera and may have significant resource implications for several reasons:

- They are relatively enhanced in volatiles if compared to most lunar regoliths;
- The glass component is more easily broken down for the extraction of oxygen than crystalline silicates;
- They are much more homogeneous in size and composition and less compacted than the general regolith which will make their use a feedstock more straightforward.

Since the Moon has no atmosphere or magnetic field, solar winds strike directly onto the surface and the particles carried by them are implanted into the regolith. The solar wind mainly consists of hydrogen and helium nuclei (see Table 2.2 for the entire list of components found in the lunar regolith at low latitudes), that have been accumulating for hundreds of millions of years. Thanks to the Apollo mission it is known that these volatiles can be degassed from the regolith by heating it to around 700 °C in order to release most of the trapped H and He, but this would be a quite energy expensive activity, requiring about 10^9 J to raise one cubic metre of regolith by 720 °C. This is approximately the amount of energy which falls on a square metre of the equatorial lunar surface in nine days, so focusing the sunlight or using microwave heating could speed up the process. Once extracted these materials can be used in different ways:

- H could be used as a rocket fuel or as a reducing agent for the extraction of Oxygen and metal from oxides;
- N could be an appropriate buffer breathable gas for long - term human operations or as support for lunar agriculture together with C and S;
- He is the most interesting component of the lunar regolith, especially the ^{3}He isotope, although its concentration in the soil is quite low. It can mainly be found in the mineral ilmenite ($FeTiO_3$) which means that it is mostly abundant in the maria. This element can be fused with deuterium (D) on Earth (where this element is much rarer because the particles are screened by the magnetic field) or on the Moon itself to generate electric energy through a nuclear reaction. The process of extraction of ^{3}He consists in the cooling of the volatile gases in the regolith which then can be separated from each other. This leads to the isolation of another isotope, ^{4}He which is much more abundant, as Table 2.2 states, and, in the liquefied form, is the element that the HRSM foresees to use for the resupply of Herschel and for cooling down its instruments back to 1.4 K, their operating temperature.

Volatile	Concentration ppm ($\mu g/g$)	Average mass per m^3 of regolith (g)
H	46 ± 16	76
^{3}He	0.0042 ± 0.0034	0.007
^{4}He	14.0 ± 11.3	23
C	124 ± 45	206
N	81 ± 37	135
F	70 ± 47	116
Cl	30 ± 20	50

Table 2.2: Average concentrations of solar wind volatiles in the lunar regolith where the quoted errors reflect the range (± refers to one standard deviation) of values found at different sampling locations

Another vital resource is clearly water, discovered only recently in some craters near the lunar poles, where there is a permanent shadow throughout all the year that takes the temperatures below 40 K, which means that the water will be frozen. These reservoirs are called 'cold traps' *(CT)* and were created by the impacts of hydrated meteorites on the surface or by of the interaction between the solar wind and the regolith at lower altitudes and the successive migration toward the polar regions. The possibility of obtaining water directly from the Moon instead of having it transferred from Earth would significantly simplify the operations, since it could be used primarily for human support in the habitats, but also for other systems, such as regenerative fuel cells, thermal management or radiation shielding. To reach these deposits, architectures with large excavators and drills have been developed but their cost was too high. A revolutionary concept consists in using lightweight capture tents and heating to sublimate the ice and transport the water vapor produced through the surface. Figure 2.8 shows how the vapor is then captured by a dome - shaped tent covering the heated surface and vented into Cold Traps outside to refreeze. Once the CTs are full, they're moved to a central processing plant for refinement into purified water, liquid oxygen (LOX) and liquid hydrogen (LH2) and replaced with new ones. As stated, water mining allows to extract oxygen as secondary product, but it can also be obtained directly from the regolith by mining anhydrous oxides and silicate minerals. In fact samples collected during previous missions on the Moon confirm that the regolith is made up of 40 - 45 % oxygen by weight [24], even though the process of extracting it is quite energy intensive. In figure 2.9 the appearance of regolith before and after the extraction of oxygen is portrayed. Thinking about the infrastructures humans will build to dwell on the Moon, it is clear that also the extraction of metals can come in handy. Iron, Titanium or Aluminium to repair or substitute parts of the structures can be found.

Iron and Titanium are present in all mare basalts, although the first is locked into silicates, so an extraction process would be pretty energy intensive. Nevertheless, it would be a natural product of the oxygen production through ilmenite reduction or it could be fetched by the regolith even if in less quantity. The second could be extracted by electrochemical processes which would also lead to the production of oxygen as secondary product. Aluminium is found in the highlands regolith and can be obtained by breaking down anorthitic plagioclase ($CaAl_2Si_2O_8$) via magma electrolysis or carbothermal reduction, two costly methods that could be replaced by an acid digestion of regolith to produce oxides followed by a reduction of Al_2O_3.

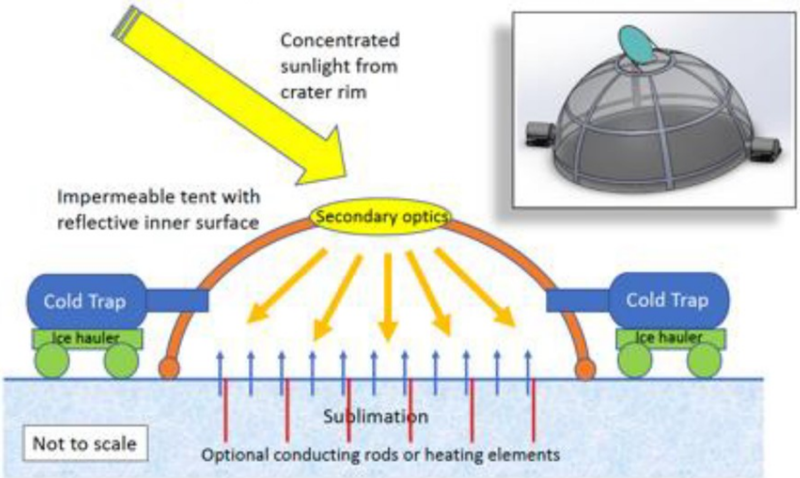

Figure 2.8: Capture Tent concept for sublimating ice

2.4 Spice

The SPICE Toolkit is offered by the NASA's Navigation and Ancillary Information Facility *(NAIF)* to assist scientists in planning and interpreting scientific observations, and engineers in modelling and planning activities for planetary exploration missions. The Toolkit is free to use for space agencies, scientists and engineers all over the world and its use is explained in a dedicated website [25]. SPICE data and software can be used in different computing environments, such as C, FORTRAN, JAVA or `MATLAB`, like in this case, thanks to the application programme interfaces *(APIs)* that users incorporate in their own programmes to read SPICE files. SPICE data sets are called *kernels* or *kernel files* and are usually accompanied by metadata, flight project data system to provide more information to the user. They are divided in:

Figure 2.9: *Left*: regolith before oxygen extraction. *Right*: regolith after oxygen extraction

- **S**PK: Spacecraft ephemeris and location of any target body, may it be a planet, a comet or a satellite, given as a function of time;
- **P**CK: Physical, dynamical and cartographic constants for target bodies, such as size, shape or orientation of the spin axis;
- **I**K: Instrument information to define geometric aspects of payloads, such as size or FoV;
- **C**K: Information on the orientation containing a transformation, called C - matrix, which provides orientation angles for a bus or structure instruments which are mounted on;
- **E**K: Events information on mission activities planned or not.

Apart from the ones listed, there are other kernels such as the frames kernel (FK) containing specifications on different reference frames, spacecraft clock (SCLK) and leap seconds (LSK) kernels to convert time tags between time measurements systems, and the digital shape model kernel (DSK) that provides higher fidelity shape models for bodies that have been studied in more detail. These kernels are additional components and are less used than the ones that appear in the acronym. The toolkit will come in handy to extract the ephemeris of the celestial bodies needed, in the most suited reference frame and relative to the time span considered for the mission.

Chapter 3

Trajectory Design

This chapters describes how the trajectory design has been carried out in order to find a set of feasible trajectories to bring the cargo spacecraft from the Moon to Herschel in compliance with the constraints of the mission.
As stated before, the working environment is the synodic frame, centered in the barycenter of the system composed of the Sun, the Earth and the Moon and rotating with the Earth - Moon angular rate. The ephemerides of the celestial bodies involved and Herschel are taken from SPICE kernels using a function called *cspice_spkezr* [26]. The toolkit contains the ephemerides of the main celestial bodies in the main reference frames, so it is not possible to directly obtain the states needed in the CR3BP. There are two possible procedures: the first consists in creating the frame in question using the SPICE routine specifying its features in an external file. The second is a more direct solution since it involves the extraction of the data in the Sun inertial frame, fixed and centered on the Sun, that are then rotated and translated to be expressed in the synodic frame. This second option has been chosen because the translation consists just in the subtraction of μ to the x components of the vectors to change the origin and the rotation occurs in the plane of motion of the Earth. Appendix A contains the procedure of extraction of data from the kernels and the files loaded.
After the extraction of data from the kernels, the coordinates of the bodies are normalized relative to the astronomical distance $\mathrm{l} = 1.4964 \cdot 10^8$ km for the positions, to the EM circular velocity $\mathrm{V_c} = 29.7834$ km/s for the velocities and to the EM angular rate $\mathrm{n} = 1.9907 \cdot 10^{-7}$ rad/s for the times.
Since the ephemerides taken from the Toolkit are relative to the J2000 reference frame, they consider the inclination and the eccentricity of the EM orbit, meaning that the astronomical unit, the tangential velocity and the angular motion vary during a revolution of the second primary around the first. Therefore, the values used for the normalization are calculated as the average of these variables, as shown in figure 3.1, where θ is the angular position of the second primary during its

revolution around the first.

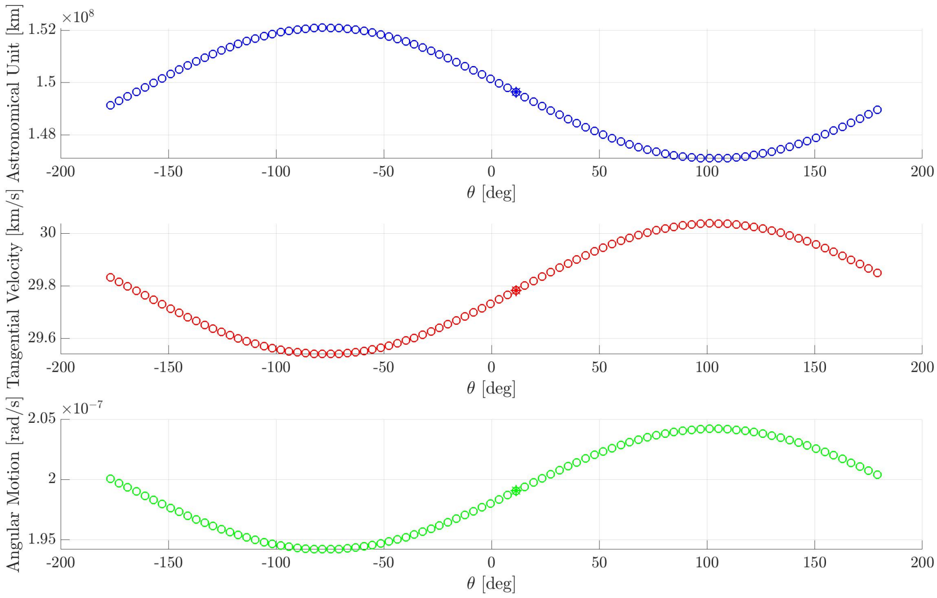

Figure 3.1: Variation of astronomical distance, tangential velocity and angular motion over one revolution

The normalization allows the software to work with smaller numbers (1 instead of $1.4964 \cdot 10^8$ for example) and to use the dynamics expressed in (2.3).
Before these equations can be used, however, the vectors need to be rotated and translated in the rotating frame. The rotation matrix is calculated using three unit vectors as columns of a 3 - by - 3 matrix (3.1) representing respectively the x, y and z axis of the reference frame. Thus, the first vector is the EM position, the third is the direction of the angular momentum vector and the second is calculated through the cross product between the previous ones (3.2).

$$\boldsymbol{R} = \begin{bmatrix} \hat{\boldsymbol{i}} & \hat{\boldsymbol{j}} & \hat{\boldsymbol{k}} \end{bmatrix} \tag{3.1}$$

with

$$\hat{\boldsymbol{i}} = \frac{\boldsymbol{r}_{EM}}{l} \qquad \hat{\boldsymbol{k}} = \frac{\boldsymbol{r}_{EM} \times \boldsymbol{v}_{EM}}{|\boldsymbol{r}_{EM} \times \boldsymbol{v}_{EM}|} \qquad \hat{\boldsymbol{j}} = \frac{\hat{\boldsymbol{k}} \times \hat{\boldsymbol{i}}}{|\hat{\boldsymbol{k}} \times \hat{\boldsymbol{i}}|} \tag{3.2}$$

The rotation of coordinates will be:

$$\boldsymbol{r}_{synodic} = \boldsymbol{R}^T \cdot \boldsymbol{r}_{inertial} \qquad \boldsymbol{v}_{synodic} = \boldsymbol{R}^T \cdot \boldsymbol{r}_{inertial} - \boldsymbol{\omega} \times \boldsymbol{r}_{synodic} \tag{3.3}$$

with $\boldsymbol{\omega} = [0\ 0\ n]^T$.

After the rotation, the position of the EM system is $\begin{bmatrix}1-\mu & 0 & 0\end{bmatrix}^{\mathrm{T}}$ at every instant of time, since the x - axis of the frame will always point towards the EM system and rotate with it. On the other hand its velocity should always be $\begin{bmatrix}0\ 0\ 0\end{bmatrix}^T$. Since eccentricity and inclination are different from zero, the velocity is not exactly null, but has a small component changing from instant to instant. The ephemeris in the inertial frame are represented in figure 3.2, whereas the ephemeris rotated are shown in figure 3.3. The Lissajous orbit, drawn in blue, is quite irregular but it extends mainly on a plane perpendicular to the plane of motion of the primaries, as shown by the y - z projection of figure 3.4

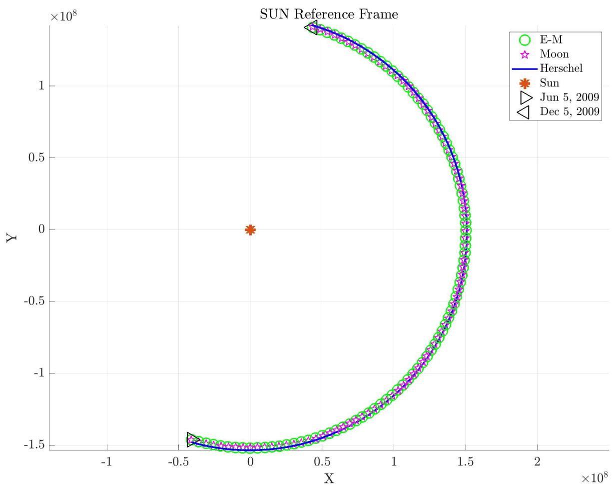

Figure 3.2: Sun Inertial Frame as extracted from SPICE

Figure 3.3 shows also how the Moon's orbit changes in inclination as it revolves around the Earth - Moon barycenter, spanning the equivalent of a hollow cylinder over time. Therefore, it is convenient to represent the Moon's trajectory exactly as a cylinder with axis passing through the EM barycenter and perpendicular to the primaries' orbital plane, radius equivalent to the maximum distance of the Moon from it, that is r $= 4.07 \cdot 10^5$ km and height equal to the difference between the highest and the lowest point of the orbit, h $= 6.968 \cdot 10^4$ km

After setting the working environment the next step is performing a grid search to find a family of feasible trajectories to go from the Moon to Herschel. In order to do so, it is appropriate to interpolate Herschel's orbit to have a proper amount of trial starting points to assess which part of the orbit enables a good solution,

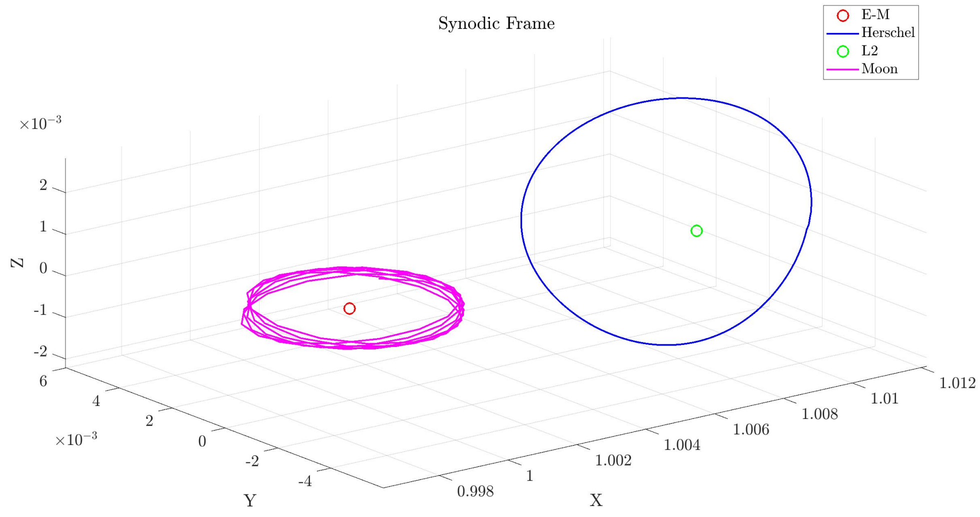

Figure 3.3: Earth - Moon barycenter, Herschel, L_2, Moon in the synodic reference frame

possibly with a low ΔV cost. In figure 3.6 it can be seen that 90 is a reasonable compromise, because it allows to maintain a good continuity of the orbit, but at the same time, doesn't foresee too many trial points that would increase the too much computational time needed to perform the grid search. It is believed, in fact, that some of the points would give similar solutions.

The interpolation is performed using the angular position θ of Herschel around the Lissajous orbit in the range $[-\pi, \pi]$, since the orbit is closed.
The procedure applied foresees a backward propagation from each of the 90 trial points of the Lissajous orbit perturbing Herschel's velocity adding a ΔV to the velocity itself as expressed in the equation below:

$$\boldsymbol{v} := \boldsymbol{v} + \Delta V \cdot \hat{\boldsymbol{v}} \tag{3.4}$$

where ΔV is a velocity magnitude, normalized relative to V_c and added to Herschel's velocity in order to perturb its state, and $\hat{\boldsymbol{v}}$ is the velocity unit vector.
The decision of using a backward propagation comes from the fact that the meeting point with the space observatory is constrained to be on the orbit, whereas the point of departure from the Moon can be any. The propagation of the orbits has been done with the `MATLAB` function `ode45`, providing the normalized three

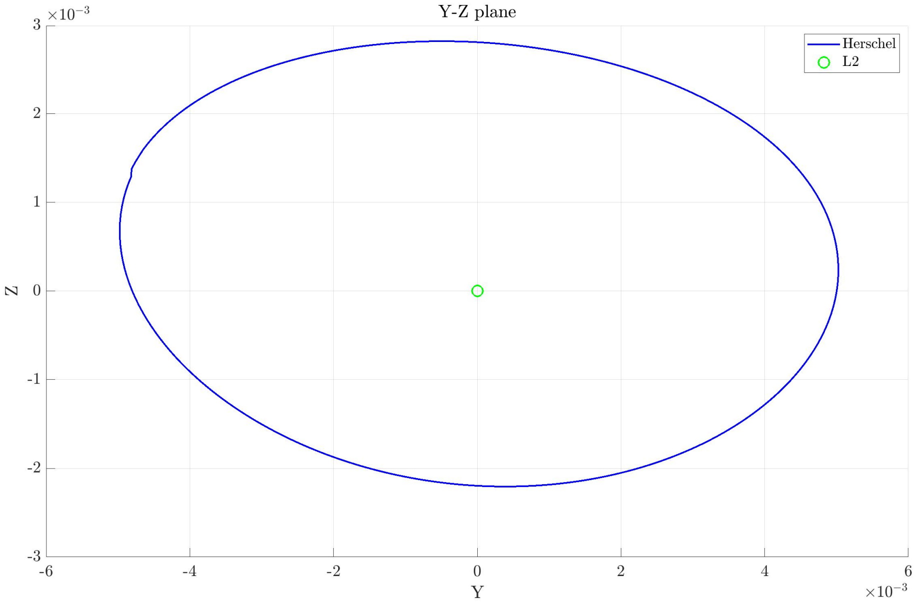

Figure 3.4: Herschel's orbit projection on the y - z synodic plane

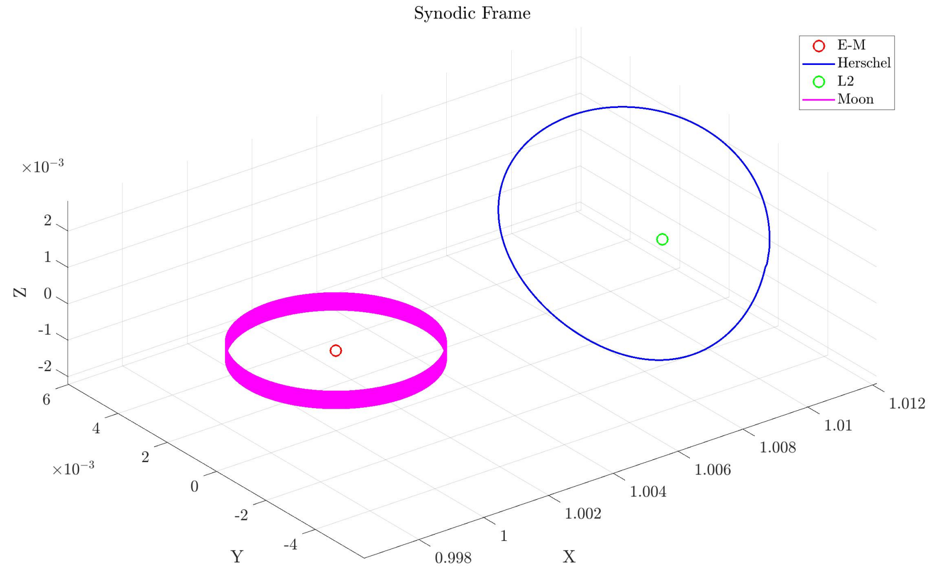

Figure 3.5: Synodic frame with cylinder for the Moon's orbit

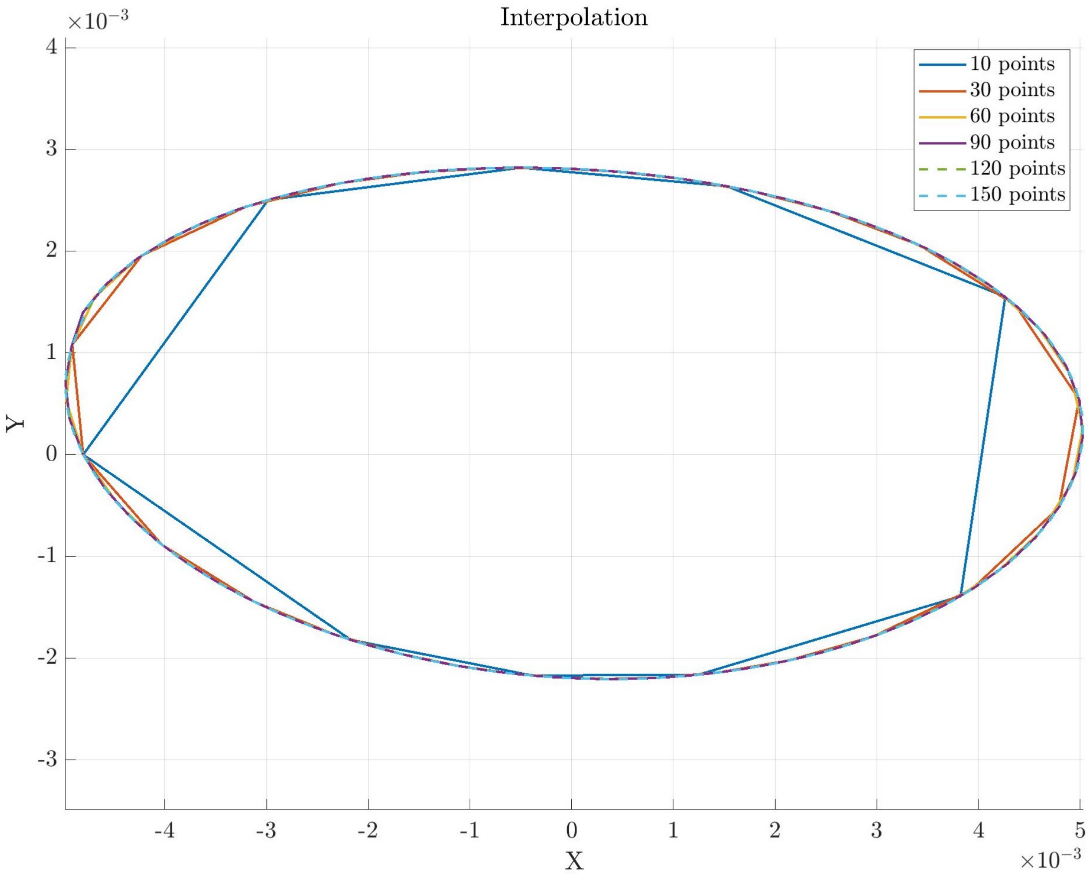

Figure 3.6: Herschel's orbit interpolation

- body dynamics, as described in (2.3), the maximum time of propagation and the initial condition. One of the constraints of the mission is on the duration of the journey to Herschel, that must not be more than a month, so the maximum propagation time is set to - 30 days, where the negative sign serves to backward propagate. Nevertheless, it is possible that some trajectories reach the Moon before, therefore, in order to avoid passing it, an event function has been created to stop the propagation once the trajectories hit the Moon's cylinder.

The event function works by observing a value until it changes sign and uses a direction specified with + 1 or - 1 to stop the propagation when the value is crossing the zero increasing or decreasing respectively. The event function in this case has been written as

Algorithm 1 Event function for stopping at the Moon cylinder

if $|z| \leq h/2$ **then**
  $value \leftarrow x^2 + y^2 - r^2$;
  $isterminal \leftarrow 1$;
  $direction \leftarrow 0$;
end if

where x and y are the in - plane coordinates of the cargo S/C changing as the propagation proceeds, and r is the Moon's cylinder radius. The event applies only if $-h/2 \leq z \leq h/2$ with z the out - of - plane component of the trajectory and h the cylinder height.
For each state of the 90 points of the Lissajous orbit, 20 ΔV trials are given, equally spanning from - 1 km/s to + 1 km/s, for a total of 1800 propagation. There are no constraints on the ΔV value to be given to establish the transfer trajectory, but going over 1 km/s might be excessive considering that the literature contains examples of trajectories with values under that amount [18]. Both positive and negative values are considered for the perturbation, so that the search is made more general.
The algorithm is summarized in 2.

With the initial conditions given, the trajectories couldn't reach the Moon, but wandered afar from it, in various directions. Some of them are shown in figure 3.7, in two different planes.

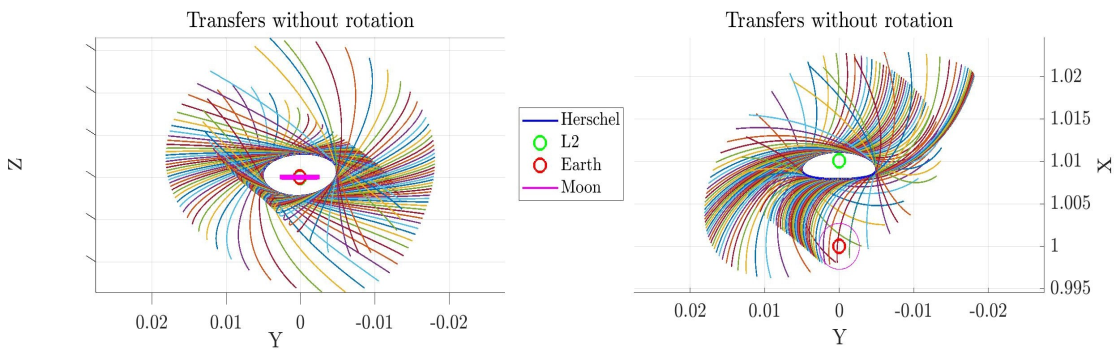

Figure 3.7: Transfers obtained perturbing Herschel with a ΔV given in the velocity direction. *Left*: y - z plane. *Right*: y - x plane

The initial conditions, then, are changed by rotating the unit vector along which the ΔV is given. Not knowing in advance which would be the right rotation angle α and around which axis the rotation should be performed, the grid search extends

Algorithm 2 Algorithm used for the grid search

$month \leftarrow 30 \cdot 24 \cdot 3600 \cdot n$;
$burn \leftarrow 20$;
$dV \leftarrow linspace(-1, 1, burns)/V_c$;
$angle \leftarrow deg2grad(45 : 45 : 315)$;
$dVmax \leftarrow 1000/V_c$;
for all *states* **do**
  $\hat{\boldsymbol{v}}_H(i) = \boldsymbol{v}_H(i)/|\boldsymbol{v}_H(i)|$;
  for all *angles* **do**
    Rotation of the unit vector of $angle(j)$;
    for all dV **do**
      $\boldsymbol{v}_H(i) = \boldsymbol{v}_H(i) + dV(k) \cdot \hat{\boldsymbol{v}}_H(i)$;
      Trajectory propagation with `ode45`;
      if *event verified* & $dV(k) < dVmax$ **then**
        Store trajectory;
        Store time of flight;
        $dVmax = dV(k)$;
      end if
    end for
  end for
end for

to these variables. Thus, for each trial ΔV the velocity unit vector is rotated of seven angles, from $\alpha = 45°$ to $\alpha = 315°$ with a step of 45° around the three axes of the reference frame in which the coordinates are expressed, raising the number of propagation to 37800. For those conditions that allowed reaching the Moon an extended grid search has been carried out to find the minimum velocity to establish the trajectory. In particular variations from - 10° to + 10° around the angle and from - 100 m/s to + 100 m/s around the velocity have been considered. At the end of the grid search at least one trajectory ending up on the Moon was found for almost every starting point considered. Figure 3.8 shows an overview of all these trajectories, whereas figure 3.9 contains the ΔV given at Herschel to set the trajectory in blue and the time of flight needed to reach the Moon in red, per angular position of the starting point on the orbit. The first pictures underlines what was already expected. Some trajectories, departing from the same side of the Lissajous, are very similar and reach almost the same point of the cylinder representing the Moon's orbit. The second picture highlights the properties of these transfers. The position equivalent to $\theta = 0°$ is on the left side of the orbit, meaning that most of the trajectories departing from the upper side, with $0° < \theta < 180°$, are those requiring a bigger impulse to reach the Moon and, as a consequence,

require less days. On the other side, most of those leaving from the lower side of the orbit, with $180° < \theta < 360°$, require half of the impulse and last more time, almost the entire month set as boundary.
Moreover, table 3.1 contains further details on the transfers for more clarity. For each angular position θ the time of flight expressed in days, hours, minutes and seconds, the ΔV, specifying if given along Herschel's velocity or opposite to it, the rotation angle α of the direction of the impulse and axis around which the rotation is given are presented. Most of the trajectories found require a rotation around the z - axis of the synodic frame and the main rotation angles are 30°, 60° or 90°.
Only 8 points didn't give a good result with these trials. For them a deeper search could be executed, considering a multiple rotations around more than one axis. Nevertheless, this has not been considered necessary, given the high number of feasible trajectories already obtained.

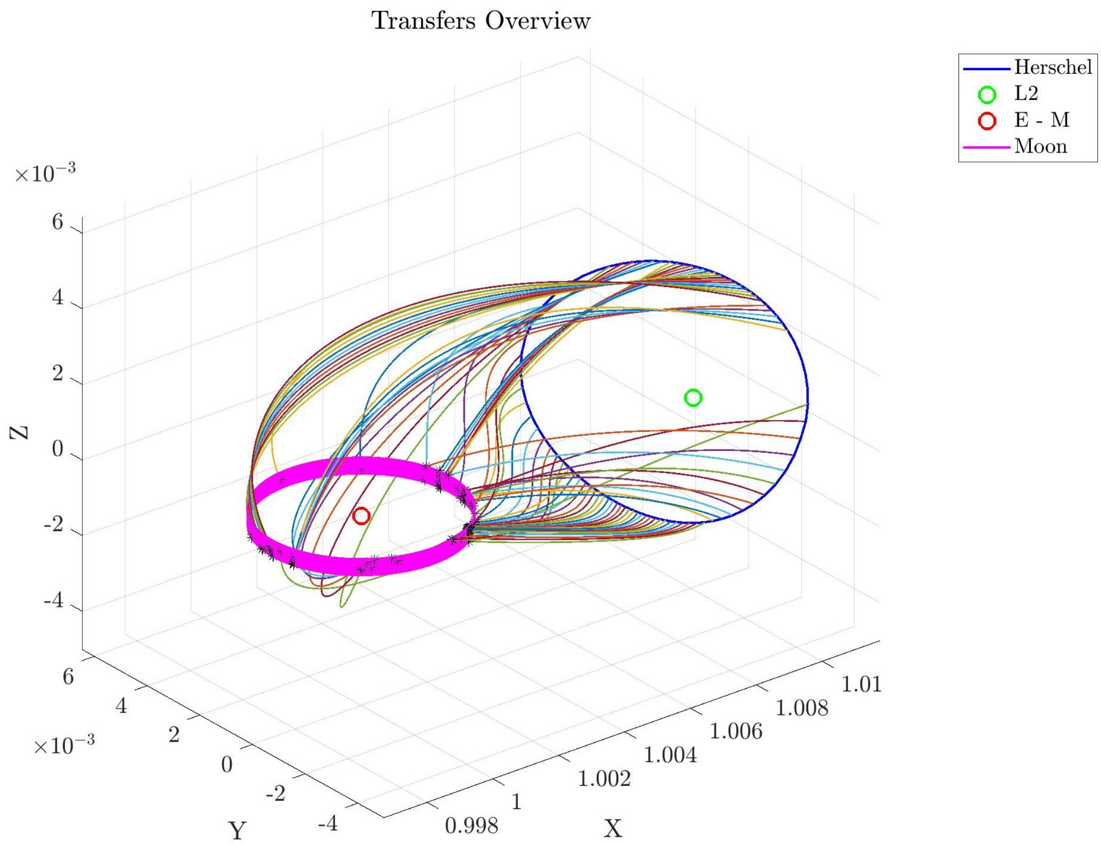

Figure 3.8: Overview of the transfers found reaching the Moon. One for each considered departing point of the orbit

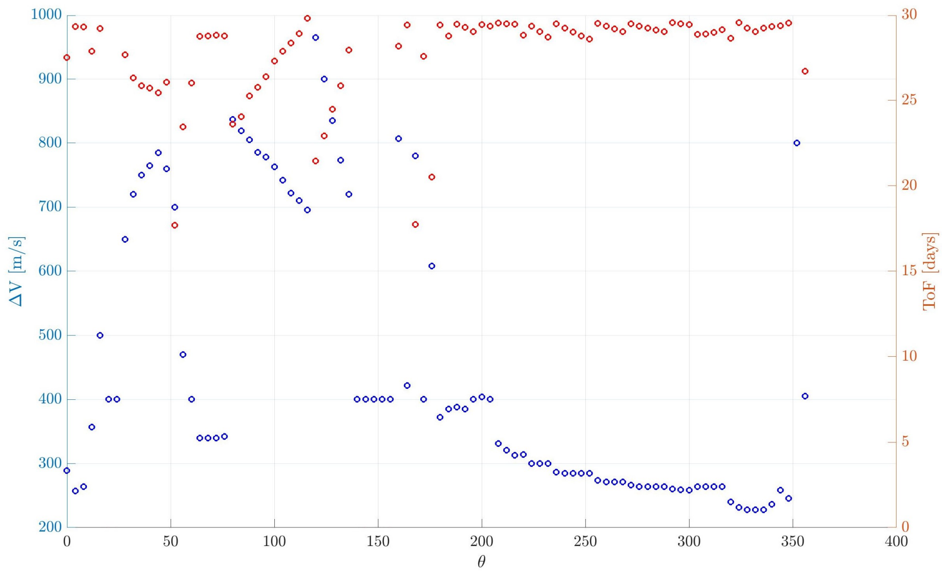

Figure 3.9: Summary of ΔV and time of flight of each transfer w.r.t. the angular position of the starting point on the Lissajous orbit

θ [°]	ΔV @ Herschel [m/s]	Time of Flight	α [°]	Axis of Rotation
0	289	27 d 12 h 25 m 48 s	90	y
4	257	29 d 7 h 58 m 6 s	90	y
8	264	29 d 7 h 10 m 45 s	80	y
12	357	27 d 21 h 5 m 28 s	70	y
16	500	29 d 5 h 16 m 23 s	65	y
20	-	-	-	-
24	-	-	-	-
28	650	27 d 15 h 58 m 17 s	60	z
32	720	26 d 7 h 45 m 14 s	60	z
36	750	25 d 20 h 35 m 44 s	60	z
40	765	25 d 17 h 21 m 27 s	60	z
44	785	25 d 10 h 54 m 36 s	60	z
48	760	26 d 1 h 24 m 1 s	60	z
52	700	17 d 16 h 37 m 47 s	90	z
56	470	23 d 10 h 45 m 38 s	90	z
60	400	26 d 0 h 24 m 43 s	90	z
64	340	28 d 17 h 57 m 35 s	90	z
68	340	28 d 18 h 44 m 20 s	90	z
72	340	28 d 19 h 49 m 13 s	90	z
76	432	28 d 18 h 40 m 31 s	90	z
80	837	23 d 14 h 36 m 0 s	60	z
84	819	24 d 0 h 59 m 54 s	60	z
88	805	25 d 6 h 29 m 32 s	60	z
92	785	25 d 18 h 39 m 26 s	60	z
96	778	26 d 9 h 25 m 59 s	60	z
100	763	27 d 7 h 24 m 54 s	60	z
104	742	27 d 21 h 15 m 34 s	60	z
108	722	28 d 8 h 43 m 9 s	60	z
112	710	28 21 h 57 m 19 s	60	z
116	696	29 d 19 h 33 m 26 s	60	z
120	965	21 d 10 h 58 m 4 s	90	z
124	900	22 d 22 h 14 m 32 s	90	z
128	835	24 d 11 h 21 m 6 s	90	z
132	774	25 d 20 h 23 m 25 s	90	z
136	720	27 d 22 h 53 m 14 s	90	z
140	-	-	-	-
144	-	-	-	-
148	-	-	-	-
152	-	-	-	-
156	-	-	-	-
160	- 807	28 d 4 h 10 m 57 s	90	x
164	- 420	29 d 10 h 5 m 27 s	60	x
168	- 780	17 d 17 h 31 m 46 s	90	x
172	- 400	27 d 13 h 52 m 6 s	60	x
176	- 608	20 d 12 h 19 m 33 s	60	x
180	- 371	29 d 10 h 13 m 33 s	35	x
184	- 385	28 d 18 h 47 m 0 s	30	x

θ [°]	ΔV @ Herschel [m/s]	Time of Flight	α [°]	Axis of Rotation
188	- 388	29 d 10 h 59 m 51 s	20	x
192	- 385	29 d 6 h 44 m 46 s	20	x
196	- 400	29 d 0 h 26 m 37 s	15	x
200	- 404	29 d 10 h 44 m 59 s	10	x
204	- 400	29 d 8 h 27 m 27 s	10	x
208	- 331	29 d 12 h 35 m 14 s	30	z
212	- 321	29 d 11 h 31 m 56 s	30	z
216	- 313	29 d 11 h 7 m 19 s	30	z
220	- 314	28 d 19 h 38 m 10 s	30	z
224	- 300	29 d 8 h 32 m 45 s	30	z
228	- 300	29 d 0 h 20 m 26 s	30	z
232	- 300	28 d 16 h 43 m 5 s	30	z
236	- 287	29 d 11 h 38 m 14 s	30	z
240	- 285	29 d 5 h 39 m 47 s	30	z
244	- 285	29 d 0 h 3 m 28 s	30	z
248	- 285	28 d 18 h 45 m 31 s	30	z
252	- 285	28 d 14 h 12 m 40 s	30	z
256	- 274	29 d 12 h 8 m 55 s	30	z
260	- 271	29 d 8 h 4 m 27 s	30	z
264	- 271	29 d 4 h 15 m 21 s	30	z
268	- 271	29 d 0 h 45 m 58 s	30	z
272	- 266	29 d 11 h 24 m 25 s	30	z
276	- 264	29 d 8 h 29 m 2 s	30	z
280	- 264	29 d 5 h 34 m 52 s	30	z
284	- 264	29 d 2 h 54 m 0 s	30	z
288	- 264	29 d 0 h 47 m 57 s	30	z
292	- 260	29 d 13 h 18 m 34 s	30	z
296	- 259	29 d 11 h 30 m 43 s	30	z
300	- 258	29 d 10 h 31 m 2 s	30	z
304	- 264	28 d 20 h 36 m 32 s	30	z
308	- 264	28 d 21 h 12 m 35 s	30	z
312	- 264	28 d 23 h 25 m 4 s	30	z
316	- 264	29 d 3 h 17 m 53 s	30	z
320	- 240	28 d 15 h 13 m 55 s	60	z
324	- 232	29 d 13 h 5 m 29 s	60	z
328	- 228	29 d 5 h 21 m 39 s	60	z
332	- 228	29 d 0 h 42 m 13 s	60	z
336	- 228	29 d 5 h 25 m 11 s	60	z
340	- 236	29 d 8 h 1 m 25 s	60	z
344	- 258	29 d 8 h 37 m 18 s	60	z
348	- 246	29 d 12 h 42 m 40 s	90	z
352	-	-	-	-
356	405	26 d 16 h 54 m 27 s	85	y

Table 3.1: Details of the feasible transfers in terms of angular starting position from the Lissajous, ΔV at Herschel, time of flight, angle and axis of rotation of the direction of the perturbation given

Chapter 4

Linearization

This chapters discusses the simplified equations of motion adopted and the linearization process carried out, explaining the assumptions behind it and showing the results obtained.
Indeed, the equations of motion in the CR3BP are non - linear (2.3), requiring a numerical scheme to be solved. The resolution, however, could be much faster if the equations were linear, because the propagation could be achieved just by solving a linear system that approximates the real solution. Undoubtedly this method is worth applying only if the error due to the approximation is not too big.
For this mission scenario, the linearization could be a useful tool to speed up the simulations for the rendezvous phase during the close proximity operations, since it is believed that the linearization error should be very small when the cargo spacecraft travels close to the equilibrium point. In fact, given that the forces are at equilibrium around L_2, the dynamics tends to be more similar to a linear one, therefore the accuracy of the approximation should worsen while getting far away from the Lagrangian point [27].

Two different simplifications have been introduced:

- Linearization via Taylor series expansion;
- Hill dynamics.

4.1 Taylor series expansion

Conte and Spencer [27] adopted a linearization method for a preliminary study of a rendezvous between two spacecrafts exploiting a Taylor expansion. In order to linearize the equations in (2.3), the non - linear terms must be taken out and turned linear. A Taylor expansion at the first order needs a linearization point

$(\mathrm{x}_0,\ \mathrm{y}_0,\ \mathrm{z}_0)$ and the computation of the first derivatives. It is executed applying the following substitutions

$$\begin{cases} x = x_0 + \delta x \to \dot{x} = \frac{d}{dt}(x_0 + \delta x) = \dot{x}_0 + \dot{\delta x} \to \ddot{x} = \frac{d}{dt}(\dot{x}_0 + \dot{\delta x}) = \ddot{x}_0 + \ddot{\delta x} \\ y = y_0 + \delta y \to \dot{y} = \frac{d}{dt}(y_0 + \delta y) = \dot{y}_0 + \dot{\delta y} \to \ddot{y} = \frac{d}{dt}(\dot{y}_0 + \dot{\delta y}) = \ddot{y}_0 + \ddot{\delta y} \\ z = z_0 + \delta z \to \dot{z} = \frac{d}{dt}(z_0 + \delta z) = \dot{z}_0 + \dot{\delta z} \to \ddot{z} = \frac{d}{dt}(\dot{z}_0 + \dot{\delta z}) = \ddot{z}_0 + \ddot{\delta z} \end{cases} \tag{4.1}$$

and computing the first derivatives of the non - linear terms as

$$r_1 = \Big[(x+\mu)^2 + y^2 + z^2\Big]^{1/2} \quad \to \quad r_1^{-3} = f_1 = \Big[(x+\mu)^2 + y^2 + z^2\Big]^{-3/2}$$

$$\begin{cases} \frac{d}{dx}(r_1^{-3/2}) = -3\,(x+\mu)\,r_1^{-5} = f_{1x} \\ \frac{d}{dy}(r_1^{-3/2}) = -3\,y\,r_1^{-5} = f_{1y} \\ \frac{d}{dz}(r_1^{-3/2}) = -3\,z\,r_1^{-5} = f_{1z} \end{cases} \tag{4.2}$$

$$r_2 = \Big[(x-1+\mu)^2 + y^2 + z^2\Big]^{1/2} \quad \to \quad r_2^{-3} = f_2 = \Big[(x-1+\mu)^2 + y^2 + z^2\Big]^{-3/2}$$

$$\begin{cases} \frac{d}{dx}(r_2^{-3/2}) = -3\,(x-1+\mu)\,r_2^{-5} = f_{2x} \\ \frac{d}{dy}(r_2^{-3/2}) = -3\,y\,r_2^{-5} = f_{2y} \\ \frac{d}{dz}(r_2^{-3/2}) = -3\,z\,r_2^{-5} = f_{2z} \end{cases} \tag{4.3}$$

By doing so, the non - linear terms can be rewritten as:

$$\begin{aligned} r_1^{-3} = f_1 = \bar{f}_1 + \delta f_1 = \bar{f}_1 + \bar{f}_{1x}\cdot\delta x + \bar{f}_{1y}\cdot\delta y + \bar{f}_{1z}\cdot\delta z \\ r_2^{-3} = f_2 = \bar{f}_2 + \delta f_2 = \bar{f}_2 + \bar{f}_{2x}\cdot\delta x + \bar{f}_{2y}\cdot\delta y + \bar{f}_{2z}\cdot\delta z \end{aligned} \tag{4.4}$$

where for any arbitrary function $g(x_0,\ y_0,\ z_0)$, $\bar{g} \coloneqq g(x_0,\ y_0,\ z_0)$. The linearization point $\begin{bmatrix} x_0 & y_0 & z_0 \end{bmatrix}^T$ in this context is the L_2 point.

The terms in (4.4) are replaced with the derivatives in (4.2) and (4.3) and the result is substituted in (2.3) applying the expansion in (4.1). The linearized equations of motion for the 3 - body dynamics are obtained:

$$
\begin{aligned}
\ddot{\delta x} = & \underbrace{\left[1 + \frac{3\,(x_0+\mu)^2\,(1-\mu)\,\bar{r_2}^5 + 3\,(x_0-1+\mu)^2\,\mu\,\bar{r_1}^5}{\bar{r_1}^5\,\bar{r_2}^5} - (1-\mu)\,\bar{f_1} - \mu\,\bar{f_2}\right]}_{A_{\dot{x}x}} \cdot \delta x + \\
& + \underbrace{3\,y_0\,\frac{(x_0+\mu)\,(1-\mu)\,\bar{r_2}^5 + (x_0-1+\mu)\,\mu\,\bar{r_1}^5}{\bar{r_1}^5\,\bar{r_2}^5}}_{A_{\dot{x}y}} \cdot \delta y + \underbrace{2}_{A_{\dot{x}\dot{y}}} \cdot \dot{\delta y} + \\
& + \underbrace{3\,z_0\,\frac{(x_0+\mu)\,(1-\mu)\,\bar{r_2}^5 + (x_0-1+\mu)\,\mu\,\bar{r_1}^5}{\bar{r_1}^5\,\bar{r_2}^5}}_{A_{\dot{x}z}} \cdot \delta z
\end{aligned}
$$

$$
\begin{aligned}
\ddot{\delta y} = & \underbrace{3\,y_0\,\frac{(x_0+\mu)\,(1-\mu)\,\bar{r_2}^5 + (x_0-1+\mu)\,\mu\,\bar{r_1}^5}{\bar{r_1}^5\,\bar{r_2}^5}}_{A_{\dot{y}x}} \cdot \delta x - \underbrace{2}_{A_{\dot{y}\dot{x}}} \cdot \dot{\delta x} + \\
& + \underbrace{\left[1 + 3\,y_0^2\,\frac{(1-\mu)\,r_2^5 + \mu\bar{r_1}^5}{\bar{r_1}^5\,\bar{r_2}^5} - (1-\mu)\,\bar{f_1} - \mu\,\bar{f_2}\right]}_{A_{\dot{y}y}} \cdot\ \delta y + \\
& + \underbrace{3\,y_0\,z_0\,\frac{(1-\mu)\,\bar{r_2}^5 + \mu\,\bar{r_1}^5}{\bar{r_1}^5\,\bar{r_2}^5}}_{A_{\dot{y}z}} \cdot \delta z
\end{aligned}
\tag{4.5}
$$

$$
\begin{aligned}
\ddot{\delta z} = & \underbrace{3\,z_0\frac{(x_0+\mu)\,(1-\mu)\,\bar{r_2}^5 + (x_0-1+\mu)\,\mu\bar{r_1}^5}{\bar{r_1}^5\,\bar{r_2}^5}}_{A_{\dot{z}x}} \cdot \delta x + \\
& + \underbrace{3\,y_0\,z_0\,\frac{(1-\mu)\,\bar{r_2}^5 + \mu\,\bar{r_1}^5}{\bar{r_1}^5\,\bar{r_2}^5}}_{A_{\dot{z}y}} \cdot \delta y + \\
& + \underbrace{\left[3\,z_0^2\,\frac{(1-\mu)\,\bar{r_2}^5 + \mu\,\bar{r_1}^5}{\bar{r_1}^5\,\bar{r_2}^5} - (1-\mu)\,\bar{f_1} - \mu\bar{f_2}\right]}_{A_{\dot{z}z}} \cdot\ \delta z
\end{aligned}
$$

The linearized system (4.5) can be rewritten as:

$$\begin{bmatrix} \dot{\delta x} \\ \dot{\delta y} \\ \dot{\delta z} \\ \ddot{\delta x} \\ \ddot{\delta y} \\ \ddot{\delta z} \end{bmatrix} = \begin{bmatrix} 0 & 0 & 0 & 1 & 0 & 0 \\ 0 & 0 & 0 & 0 & 1 & 0 \\ 0 & 0 & 0 & 0 & 0 & 1 \\ A_{\dot{x}x} & A_{\dot{x}y} & A_{\dot{x}z} & 0 & 2 & 0 \\ A_{\dot{y}x} & A_{\dot{y}y} & A_{\dot{y}z} & -2 & 0 & 0 \\ A_{\dot{z}x} & A_{\dot{z}y} & A_{\dot{z}z} & 0 & 0 & 0 \end{bmatrix} \begin{bmatrix} \delta x \\ \delta y \\ \delta z \\ \dot{\delta x} \\ \dot{\delta y} \\ \dot{\delta z} \end{bmatrix} \tag{4.6}$$

where $A_{\dot{x}x}$, $A_{\dot{x}y}$, $A_{\dot{x}z}$, $A_{\dot{y}x}$, $A_{\dot{y}y}$, $A_{\dot{y}z}$, $A_{\dot{z}x}$, $A_{\dot{z}y}$, and $A_{\dot{z}z}$ can be easily drawn from (4.5). In the sequel, the Jacobian matrix of this system is referred to as $\mathbf{A}$.

4.2 Hill dynamics

In its full generality, the Hill problem [28] has several applications in astronomy, especially in the exploration of planetary ring dynamics and rigid systems. While the 3 - body problem is an approximation for a mass perturbed by two larger ones, the Hill problem is valid in case two of the three masses are small when compared to the other and in case these two masses are close to each other relative to their distance from the third. In the HRSM the cargo S/C is moving under the perturbations of the Earth - Moon binary system, considered as a single body, and the Sun. The latter is much bigger than the first two bodies and it is further away from Herschel than the EM system and the cargo. To quantify, the Hill approximation is accurate as long as the distance between the two smaller masses is within $\mu^{1/3} \approx 0.0145$. The distance between the EM barycenter and the further point reached by Herschel around its orbit is 0.0112, thus acceptable results are expected.

Hill equations of motion are expressed as follows:

$$\begin{cases} \ddot{x} = 2\dot{y} + (3 - \frac{1}{r^3})x \\ \ddot{y} = -2\dot{x} - \frac{y}{r^3} \\ \ddot{z} = -(1 + \frac{1}{r^3})z \end{cases} \tag{4.7}$$

Again, the system can be linearized and the Jacobian matrix of the system can be built.

$$\boldsymbol{A} = \begin{bmatrix} 0 & 0 & 0 & 1 & 0 & 0 \\ 0 & 0 & 0 & 0 & 1 & 0 \\ 0 & 0 & 0 & 0 & 0 & 1 \\ 3-\frac{1}{r^3} & 0 & 0 & 0 & 2 & 0 \\ 0 & -\frac{1}{r^3} & 0 & -2 & 0 & 0 \\ 0 & 0 & -(1+\frac{1}{r^3}) & 0 & 0 & 0 \end{bmatrix}$$

where $r = \sqrt{x^2 + y^2 + z^2}$.

4.3 Simulations - Close Proximity Operations

The linear system can be solved using the following equation

$$\boldsymbol{x}(t_{k+1}) = \boldsymbol{\Phi}(t_k,\ t_{k+1}) \cdot \boldsymbol{x}(t_k) \tag{4.8}$$

where $\mathrm{t_{k+1}}$ is the time step successive to $\mathrm{t_k}$. $\boldsymbol{\Phi}$ is the state transition matrix (STM) and it can be computed in two different ways:

1. $\boldsymbol{\Phi}_1 = \mathbb{1}_{6\times 6} + \boldsymbol{A} \cdot \Delta t$
2. $\boldsymbol{\Phi}_2 = e^{\boldsymbol{A} \cdot \Delta t}$

In all cases the variable $\Delta t \coloneqq t_{k+1} - t_k$ is negative to perform a backward propagation.
The second type has been used by Mand [15] in one of the proposed algorithms, whereas the first is of simple derivation: starting from the linear system representation in absence of control forces $\dot{\boldsymbol{x}} = \boldsymbol{A}\boldsymbol{x}$, the derived state can be rewritten as an incremental ratio

$$\frac{\boldsymbol{x}_{k+1} - \boldsymbol{x}_k}{\Delta t} = \boldsymbol{A}\boldsymbol{x}_k$$

By computing $\frac{\partial \boldsymbol{x}_{k+1}}{\partial \boldsymbol{x}_k}$ the state transition matrix $\boldsymbol{\Phi}_1 = \mathbb{1}_{6\times 6} + \boldsymbol{A} \cdot \Delta\mathrm{t}$ is obtained.

In order to assess the efficiency and fastness of the linear resolution of the equations of motion, the linearized dynamics is also propagated through `ode45` and the results compared in term of accuracy and computational time.
To sum up, a list of all the equations of motion that will be used for the linearization of the 3 - body dynamics and how they will be propagated is presented:

- Linear 3 - body dynamics (4.5) propagated with the linear system resolution as described in (4.8), using the two different methodologies of STM;

- Linear 3 - body dynamics (4.5) propagated with `ode45`;
- Hill dynamics (4.7) propagated with the approximation (4.8), using the two different methodologies of STM;
- Hill dynamics (4.7) propagated with `ode45`.

Therefore, in order to decide which approximation works best, the different equations are used on the trajectory requiring the minimum amount of ΔV among those found previously, shown in figure 4.1. This trajectory requires 228 m/s of thrust at Herschel and takes 29 d 5 h 21 m and 39 s.

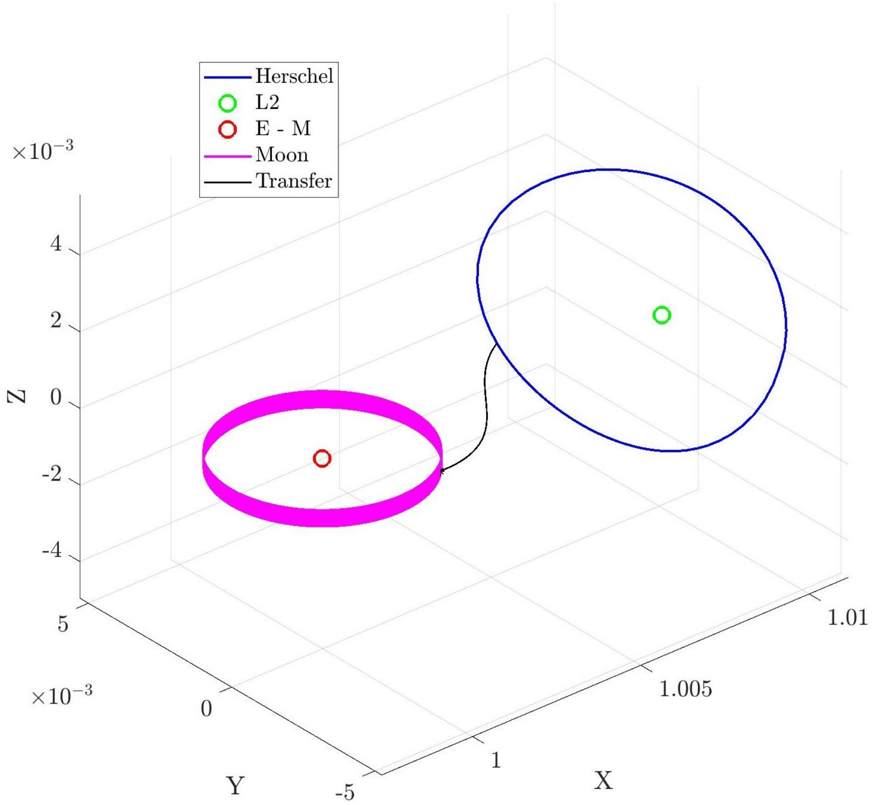

Figure 4.1: Trajectory requiring the lowest impulse at Herschel to reach the Moon among the set

However, the rendezvous phase will take place only in the last few kilometers from Herschel, as will be discussed in Chapter 5, thus, 5 km from the SO have been considered. In order to analyse only this segment of track, the event function used to stop the propagation (1) has been changed, setting the value variable to

$$\sqrt{(x - x_H)^2 + (y - y_H)^2 + (z - z_H)^2} - distance$$

with x, y, z coordinates of the current propagation, x_H, y_H, z_H coordinates of the reference point, Herschel, and distance equal to 5 km normalized relative to the astronomical unit. By doing so the backward propagation will stop exactly at 5 km from Herschel, as figure 4.2 shows.

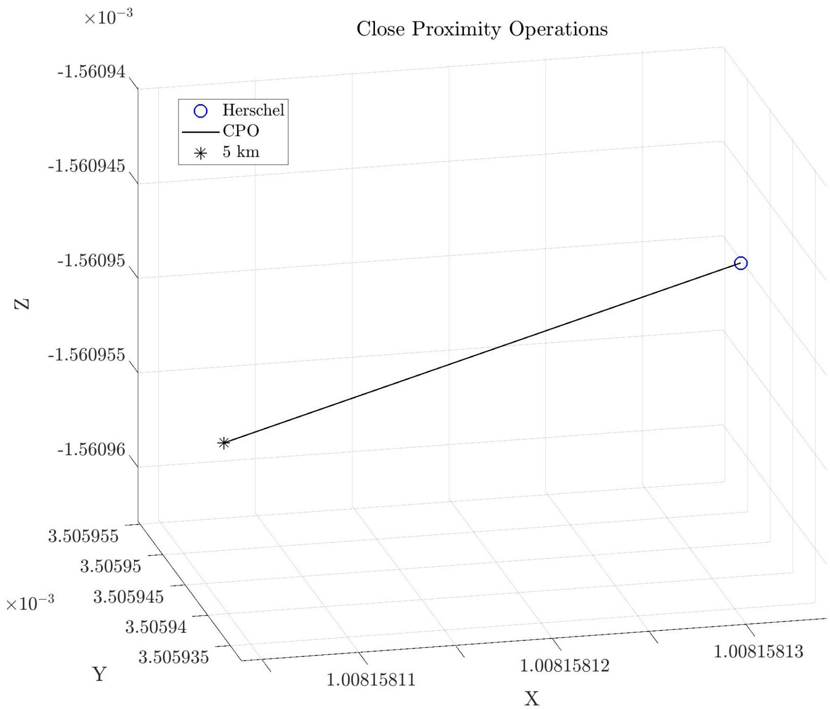

Figure 4.2: First 5 km from Herschel of the trajectory requiring the lowest impulse to reach the Moon

Implementing the aforementioned methods for the linearization in the case of the Taylor expansion, some considerations can be made. By looking at figure 4.3, it is clear that the propagation with $\mathbf{\Phi}_1$ performs better for the position error, whereas there are very little differences for the velocity. The results obtained with $\mathbf{\Phi}_2$, on the other hand, are comparable to the use of the `ode45` function for efficiency. Moreover, the linear system solved with $\mathbf{\Phi}_1$ is about three times faster than the one solved using $\mathbf{\Phi}_2$, while the propagation with the Runge - Kutta method is 1000 times slower than using any of the state transition matrices.
The same logic is used for the Hill dynamics, obtaining the results in figure 4.4. They point out that, in this case as well, the use of $\mathbf{\Phi}_1$ is the best for what concerns the position, while unlike in the Taylor approximation, $\mathbf{\Phi}_2$ performs worse than the other two. Furthermore, the propagation with `ode45` performs better for

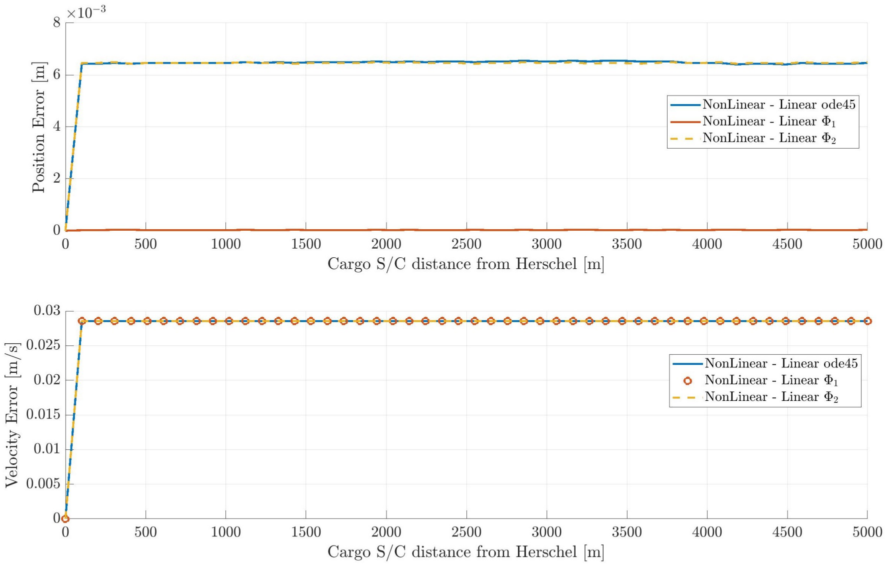

Figure 4.3: Position and velocity errors for the CPO trajectory propagated with the linear dynamics obtained via Taylor series expansion

what regards the velocity. As well as for the Taylor approximation, the linear resolution with $\mathbf{\Phi}_1$ is the fastest, followed by the resolution with $\mathbf{\Phi}_2$ and then by the propagation with `ode45`.

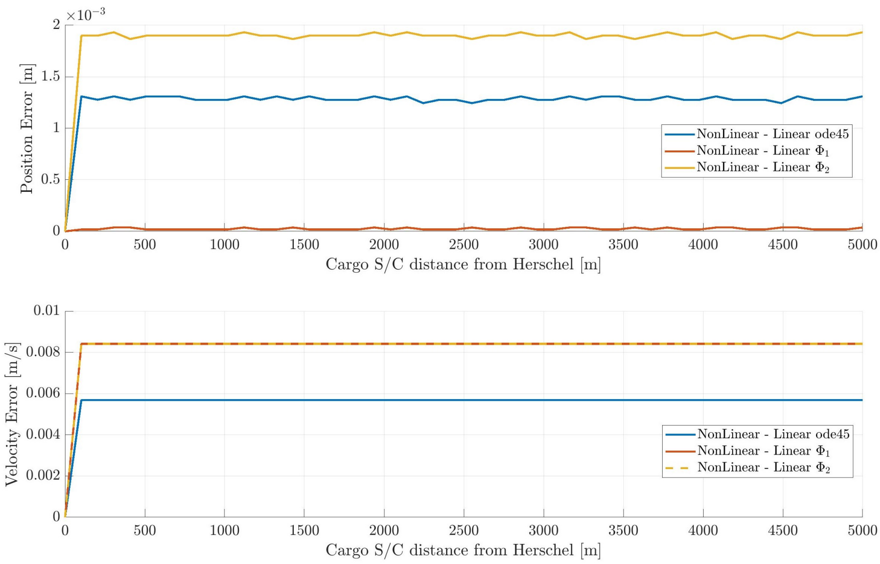

Figure 4.4: Position and velocity errors for the CPO trajectory propagated with the Hill's dynamics

Considering the previous results, both the propagation with $\mathbf{\Phi}_1$ and with `ode45` present one advantage and one disadvantage, therefore a compromise must be found. The propagation with $\mathbf{\Phi}_1$ brings to better results in position for both the Taylor and the Hill approximation, whereas the resolution with `ode45` brings to better results in velocity for the Hill approximation. However, the latter, requires a much higher computational time, therefore the propagation with the $\mathbf{\Phi}_1$ is preferred also considering that the error introduced is just slightly bigger. The linear system solved with $\mathbf{\Phi}_2$ and the propagation of the linear system with `ode45` are then discarded.
Eventually, the two linearization procedures propagated with $\mathbf{\Phi}_1$ are compared and, in figure 4.5, it can be seen that the Hill approximation performs slightly better in velocity while giving the same errors in position. These results show position errors in the order of cents of millimeter for both the approximations and velocity errors in the order of dozens of millimeters per second for the Taylor expansion and millimeters per second for the Hill approximation. They are obtained with 50 steps of resolution of the linear system, where the linearization point was fixed on the starting point on the Lissajous orbit, while the initial state for each state computation is the one obtained with the non - linear propagation at the previous step. In contrast, using the state obtained with the linear propagation at the previous step, the errors would rise to dozens of meters and some meters per second respectively.
In conclusion, the state propagation with a linear system resolution using the Hill dynamics and the STM $\mathbf{\Phi}_1$ results being better, therefore it will be used as a linearization technique in the rendezvous phase together with the non - linear dynamics.

4.4 Simulations - Whole Transfer

For thoroughness, the linearization is performed on the whole chosen trajectory, following the same logic of the close proximity operations and using only the chosen approximation, the Hill dynamics. Figure 4.6 shows how the error increases as the cargo moves away from the Lagrangian point reaching the order of meters and meters per second for position and velocity respectively. The number of steps to reach this result has been set to 50000 after a fast analysis of the errors for different steps. Figure 4.7 shows how the errors decrease as the step increases, but a higher computational time must also be taken into account.

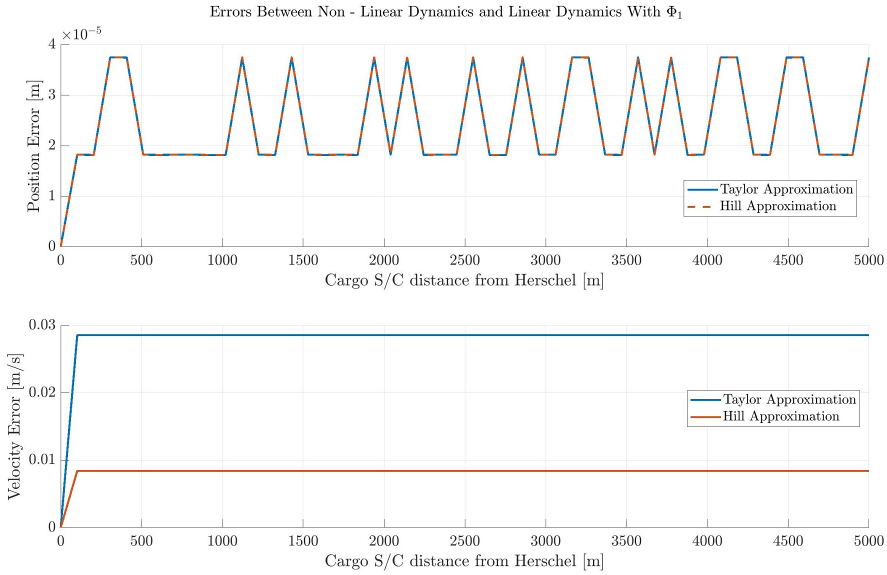

Figure 4.5: Comparison between Taylor and Hill's approximations for position and velocity in CPO

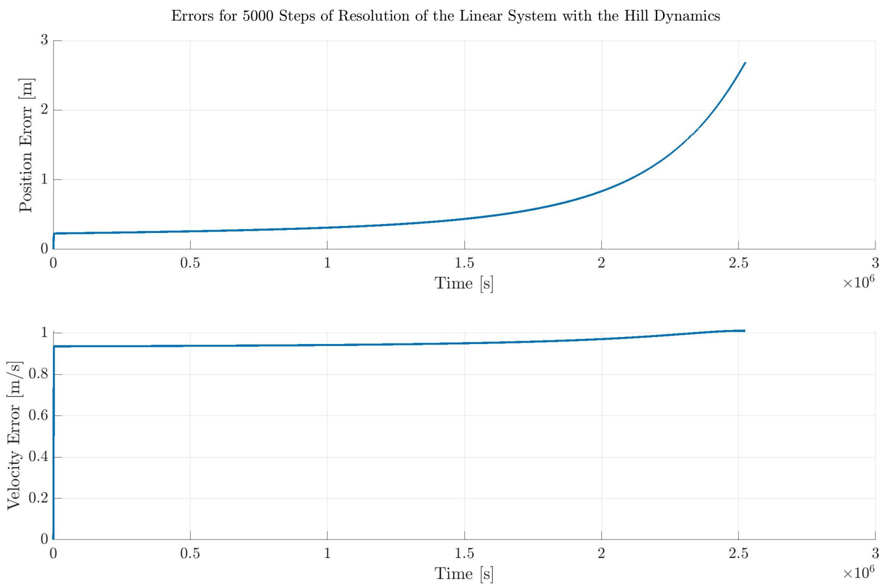

Figure 4.6: Position and velocity linearization errors for the whole trajectory

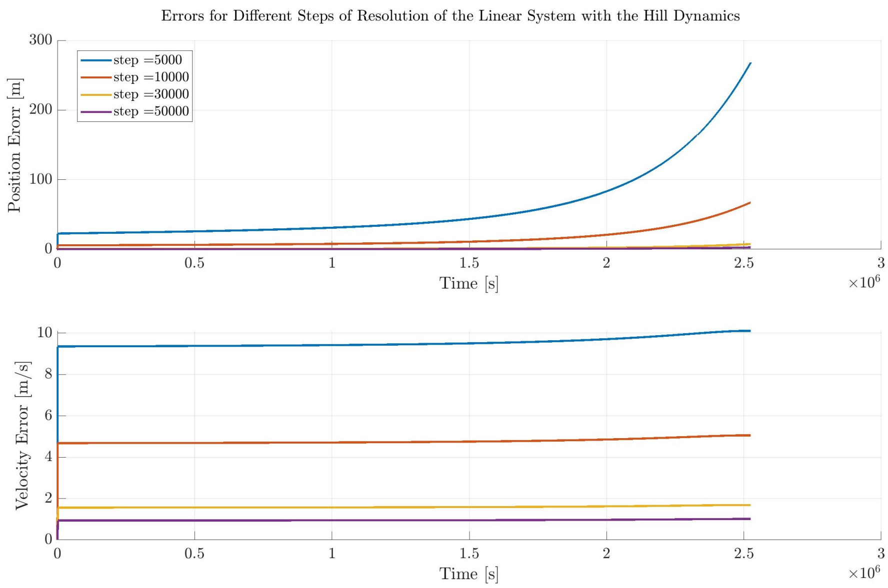

Figure 4.7: Position and velocity linearization errors for the whole trajectory for different number of resolution of the linear system

Chapter 5

Rendezvous

This chapter deals with the Rendezvous phase, presenting the methodology employed to perform a manoeuvre to approach Herschel.
The International Rendezvous System Interoperability Standards *(IRSIS)* [29] provides basic common parameters to design compatible rendezvous operations that will enable interoperability in cislunar and deep space environments. According to these regulations there are areas of space in which the different CPO phases can be executed:

- Rendezvous Sphere *(RS)*, a 10 km radius sphere centered on the CoM of the target S/C;
- Approach Sphere *(AS)*, a 1 km radius sphere centered on the CoM of the target S/C;
- Keep Out Sphere *(KOS)*, a 200 m radius sphere centered on the CoM of the target S/C;
- Approach/Departure Corridors, volume of a cone of $\pm 10°$ of opening, centered on the CoM of the target S/C;

A representation of these spheres and corridor is displayed in figure 5.1. In order to be compliant with the regulations the same regions have been adopted to carry out CPO for the HRSM, initiating RdV at 5 km from Herschel and starting the approach from outside the KOS. Moreover, the approach has to be performed with a low relative velocity w.r.t. the target in order to actuate abortion manoeuvres in case one of the systems doesn't work as expected or the approach cannot be performed in a safe way for other reasons. In addition, for the HRSM, the approach corridor can be expanded thanks to the possibility of the SO to rotate around two of its body axis. Figure 5.2 shows the Herschel's body frame in red. The sunshield is pointed at the Sun, therefore the y body axis is directed opposite to the x synodic axis (in black). In order to avoid the sun rays to hit the cryostat Herschel's rotations are bounded within $\pm 30°$ around the x body axis and $\pm 10°$ around the z body axis.

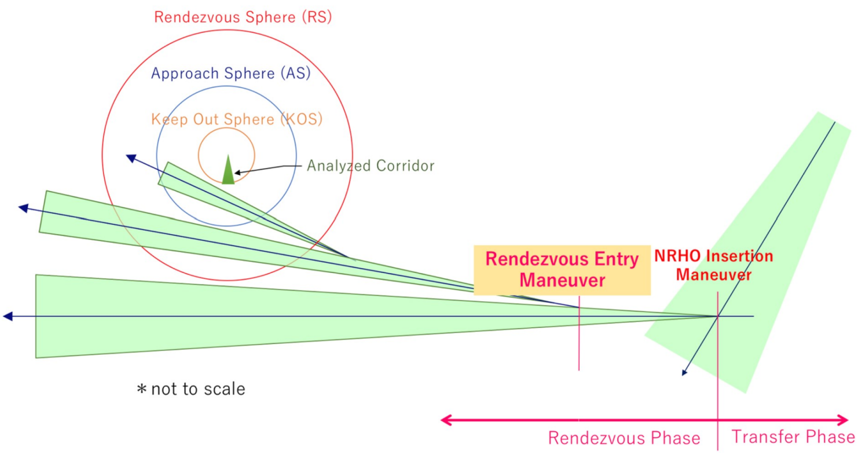

Figure 5.1: Rendezvous regions

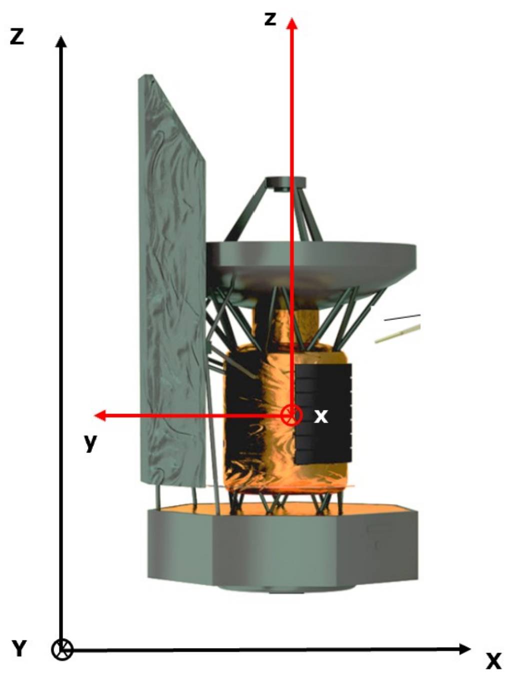

Figure 5.2: Herschel body frame

The baseline trajectory identified in the previous chapter comes with two problems: it takes the Cargo to Herschel from the front, where the sunshield is located, and foresees a very fast approach with a sudden, massive brake once the SO is reached. The time needed to cover the 5 km of distance represented in figure 4.2 is, in fact, only 22.3 seconds, clearly too short to perform an abortion manoeuvre in case a system doesn't work as expected.
In order to avoid these two problems a flanking manoeuvre has been implemented, so that the time rises and the approach takes place from the back of the observatory, where the docking port is located. Moreover the last impulse given at the SO needs to be very small, a few meters per second or less, in order to be compliant with the regulations. A multiple shooting technique has been employed to perform this manoeuvre.
Multiple shooting [30] foresees the breaking up of a trajectory into sub intervals and the definition of an initial value problem for each of them. Starting from the initial condition given, that it is not likely to solve the problem, a certain number of iterations is performed until boundary conditions and continuity properties at the end of each sub interval are satisfied.
Considering the high approaching speed, the shots given are necessary to progressively brake the cargo spacecraft until its velocity almost matches Herschel's one. The manoeuvre is implemented as an optimization problem following the scheme in figure 5.3.

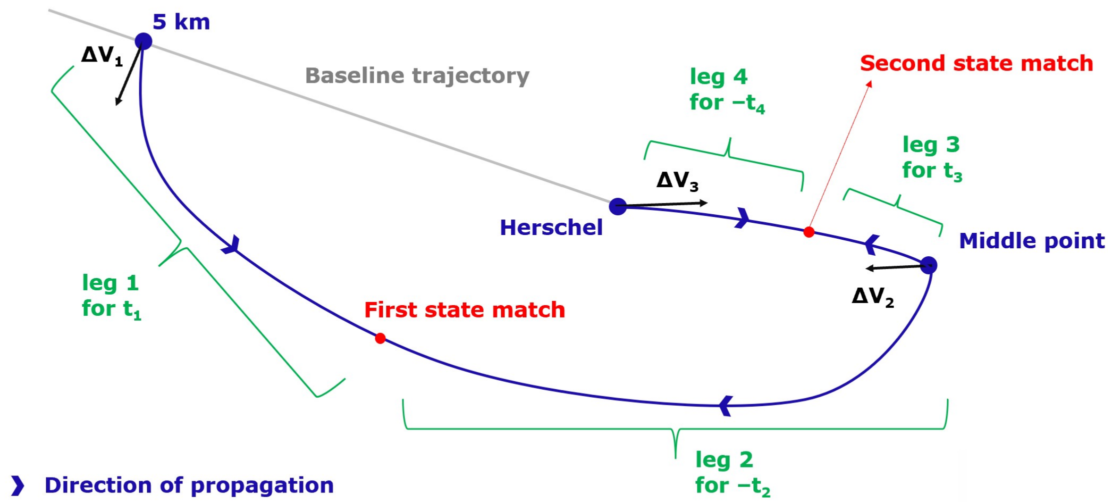

Figure 5.3: Optimization Scheme

The strategy makes use of three brakes: one at the start at 5 km, the second at a point behind Herschel (middle point) and the last one at few meters from Herschel itself. The first one deviates the cargo from the baseline trajectory, allowing it

to turn around Herschel, the second acts as a checkpoint and directs the cargo towards the observatory, the third aligns the chaser's velocity to the target's one, making Caroline almost still w.r.t. Herschel.
The optimization has been set up in different ways before finding a final solution. Each one is an improvement of the previous one, obtained by changing constraints or the variables given to the optimizer. The following section contains the details on how the successful optimization has been carried out.

5.1 Optimization

The propagation is performed in two directions, backward and forward, for each piece of trajectory between the impulses given. A total of four legs is obtained, that are constrained to match two by two.

5.1.1 Optimization variables

- 3 $\boldsymbol{\Delta V}_\mathrm{s}$ as vectors ($\boldsymbol{\Delta V}_1,\ \boldsymbol{\Delta V}_2,\ \boldsymbol{\Delta V}_3$) $\longrightarrow$ 9 variables;
- 4 times of flight ($\mathrm{t}_1,\ \mathrm{t}_2,\ \mathrm{t}_3,\ \mathrm{t}_4$) $\longrightarrow$ 4 variables;
- State of the middle point ($\mathrm{x},\ \mathrm{y},\ \mathrm{z},\ \dot{\mathrm{x}},\ \dot{\mathrm{y}},\ \dot{\mathrm{z}}$) $\longrightarrow$ 6 variables.

In total there are 19 optimization variables.

5.1.2 Constraints

- State forward propagated from the starting point for t_1 seconds perturbed with $\boldsymbol{\Delta V}_1$ matches the state backward propagated from the middle point for $-\,\mathrm{t}_2$ seconds;
- State forward propagated from the middle point for t_3 seconds perturbed with $\boldsymbol{\Delta V}_2$ matches the state backward propagated from Herschel for $-\,\mathrm{t}_4$ seconds perturbed with $\boldsymbol{\Delta V}_3$;
- $\Delta \mathrm{V}_3 < 10\ \ \mathrm{m/s}$

In total there are 12 equality constraints on the matching of the states and 1 inequality constraint on the magnitude of the last impulse.

5.1.3 Cost function

The cost function for the optimization has been initially set to 1 to study the feasibility of the problem.

5.1.4 Boundaries

To assure a solution compliant with the constraints of the mission, the middle point has been bounded behind Herschel, in an ellipsoid of axes 2 x 1 x 1 km aligned to the synodic axes as shown in figure 5.4. This volume has been chosen considering that the approach must happen within the approach cone, therefore avoiding the middle point to be too far from Herschel in the y and z direction can simplify the approach. The x direction is less problematic since the docking port is aligned to the x - axis. However, a boundary has been set in this direction too in order not to pointlessly waste fuel in going far behind Herschel and then going back towards it. On the other hand, the times of flight have been bounded between 1 and 23 hours each, since employing less time than the former boundary or more than the latter boundary would result in a manoeuvre too fast or too slow respectively. The other variables have been left unbounded.

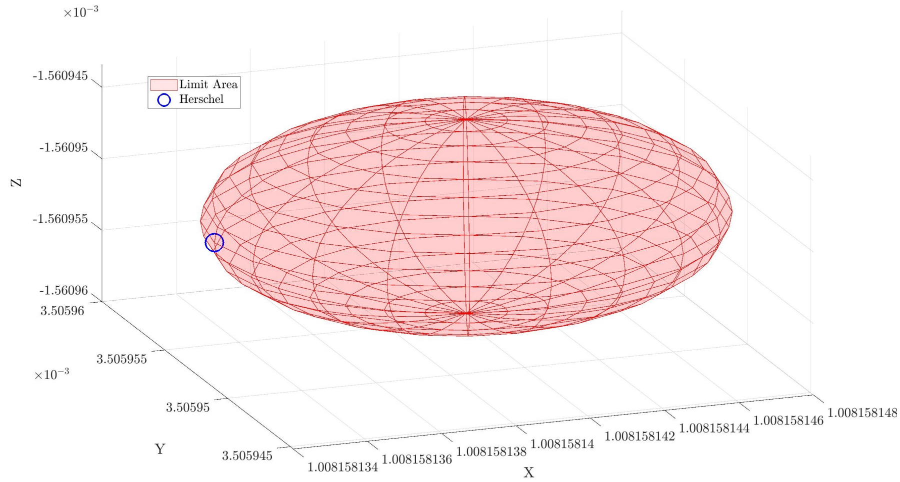

Figure 5.4: Volume in which the middle point has been bounded for the optimization

5.1.5 Initial Conditions

The initial conditions given are the following:

- $[0\ 0\ 0]^{\mathrm{T}}$ for the three $\boldsymbol{\Delta V}_{\mathrm{s}}$;
- The time of flight of the baseline trajectory to reach Herschel from the starting point for the four times (22.3 seconds);
- Herschel's state at rendezvous for the middle point.

5.1.6 Results

Non - linear dynamics The first simulations proved that changing the initial conditions fixing the boundaries brought exactly to the same results. On the contrary, changing the boundaries and fixing the initial conditions allowed a good variation of the manoeuvre. Therefore, the only parameters that have been changed in the search for a good solution are the boundaries on the position of the middle point, varied within the red area in figure 5.4, and the times of flight, varied from 1 to 23 hours.

The dynamics on the left side of the Lissajous orbit, however, didn't allow the approach from behind with a very low relative velocity. The problem appeared to be unfeasible, thus the constraint on the ΔV_3 has been lifted bringing to trajectories needing a total $\Delta V \approx 11$ km/s and a total approach time of 46 hours.

The rendezvous point on the Lissajous orbit, then, has been changed to a different one, close to the previous point, at an angular position of 8° requiring few dozens of meters per seconds of impulse at Herschel to reach the Moon more than the previously studied trajectory. However, this point too didn't bring to acceptable results, even though the total ΔV needed for the manoeuvre has been lowered to about 500 m/s. The problem is that manoeuvre comes with a $\Delta V_3 \approx 190$ m/s, which is not low enough for a safe approach. Moreover, the velocity error w.r.t. the arrival point is of the same order of the last impulse. These results imply that the direction of the Herschel's velocity on the left side of the Lissajous orbit is not suited for the desired approach, because the cargo needs to be given a high impulse to match it. Furthermore, figure 5.5 points out that, even though the middle point is set inside the approach corridor, the last leg follows a hop - like trajectory going out of it and approaching Herschel from the y - axis. As the figure shows, more trials have been executed, changing the initial conditions, but resulting in the same path.

According to these solutions, then, the opposite side of the Lissajous orbit is believed to be more suited for the approach. The baseline trajectory is moved to the one showed in figure 5.6, requiring 420 m/s of ΔV and a little bit more than 29 days of travel. The previous trajectory needed only 228 m/s of ΔV at Herschel and about the same time of flight. The cost of the mission has been raised in order to perform a rendezvous according to the regulations.

By doing so, two main solutions were obtained. The first is essentially the baseline trajectory found in the grid search, but since the cargo spacecraft approaches Herschel in few seconds with a high velocity before the final brake, it's discarded. The details of this solution are in table 5.1 and a portrayal is shown in figure 5.7.

The second solution, portrayed in figure 5.8, is more feasible since it takes several hours to reach the space observatory allowing a slower approach.

Table 5.2 contains the details of this manoeuvre in terms of magnitude of the

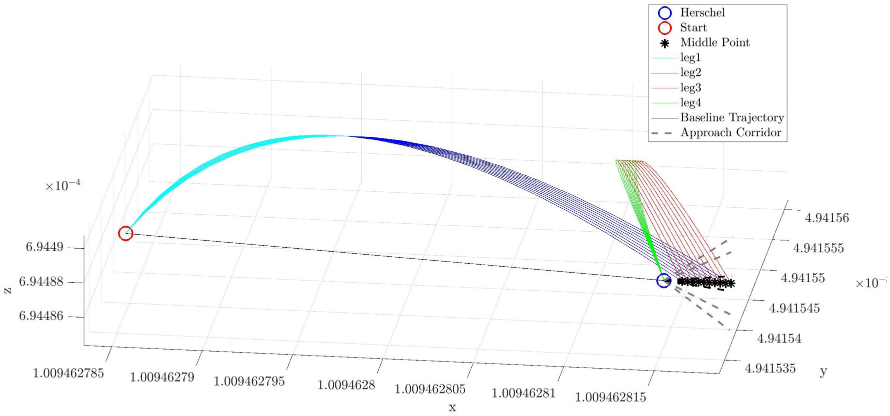

Figure 5.5: Rendezvous at Herschel on the left side of the Lissajous orbit requiring a high ΔV

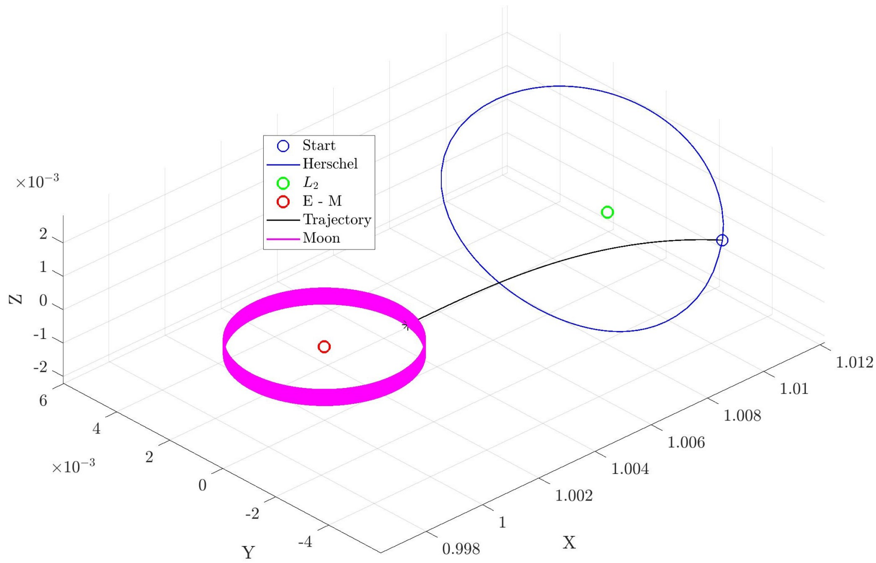

Figure 5.6: Trajectory reaching Herschel on the right side of the Lissajous orbit

impulses and times of flight. Even if performed in two different environments, these results can be compared to the ones obtained with the AVANTI mission [7], with some considerations. In the case of AVANTI, the rendezvous happened in a LEO orbit, thus a stronger gravitational attraction was exerted on the vehicles. Moreover, the rendezvous time was in the range of days. The ΔV needed for a far - mid range RdV was about 360 m/s. The environment close to L_2 is less influenced by the atmospheric drag in comparison to a LEO orbit, but the need to perform a flanking manoeuvre from 5 km of distance and in a much shorter time makes the

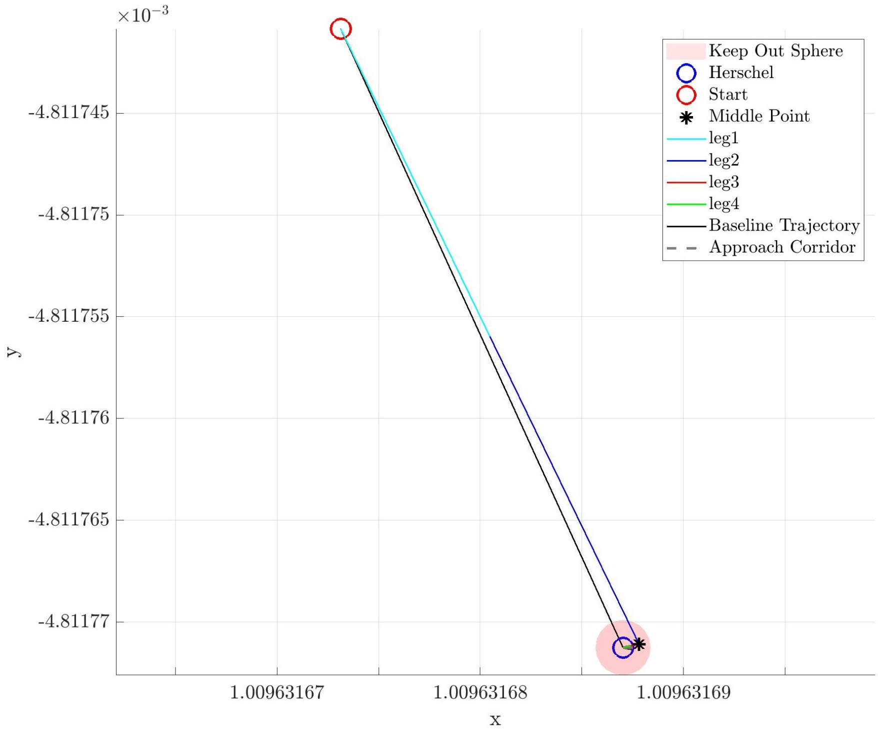

Figure 5.7: Fast Rendezvous

ΔV_1	330.4 m/s
ΔV_2	171.2 m/s
ΔV_3	10 m/s
ΔV_{TOT}	511.6 m/s
Time of Flight	0 h 50 m 56 s
Position Error	3.75 mm
Velocity Error	20 m/s

Table 5.1: Details on the time of flight, impulses magnitude and errors for the fast rendezvous

results obtained, needing only about 150 m/s more, quite reasonable.

Table 5.3 contains the errors from the desired point reached at the end of the rendezvous. The low velocity error makes the cargo spacecraft almost still w.r.t. Herschel so that the docking phase can be executed.

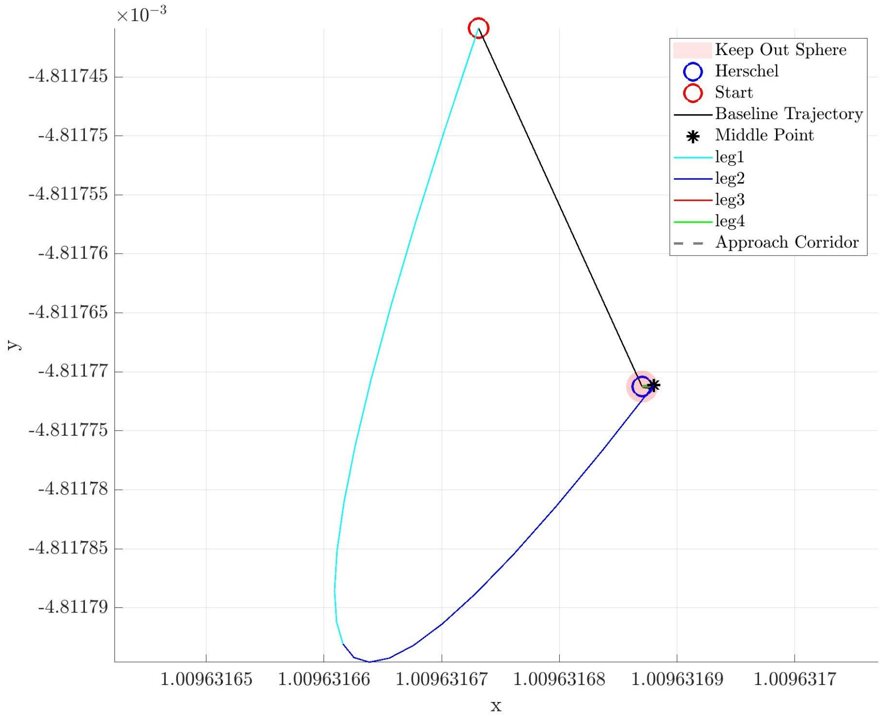

Figure 5.8: Rendezvous phase

ΔV_1 [m/s]	ΔV_2 [m/s]	ΔV_3 [m/s]	ΔV_{TOT} [m/s]	ToF
331.3	180.6	$8.4 \cdot 10^{-2}$	511.9	7 h 0 m 1 s

Table 5.2: Magnitude of the three impulses and total time of flight of the rendezvous phase

The only drawback of this solution is that the final leg of the approach is not restrained in the approach cone in the x - z plane, as shown in figure 5.9. No problems are encountered in the x - y plane, as shown in figure 5.10. In the two figures, the black dashed lines are the projection of the approach corridor on the two planes, whereas the grey dashed ones are the expansion of the corridor due to Herschel's rotation around its body axes.
Other solutions have been obtained by changing the boundaries on the position of the middle point, but the dynamics brought every time the trajectory to rendezvous from above in the z direction. Thus, the cost function has been set to $J = |z_{middle\ point} - z_H|$ in order to minimize the z distance between the middle point and Herschel and allow the last leg to enter the approach cone, but the simulations gave similar results. Figure 5.8 shows the best result obtained in terms of distance

Position Error [mm]	Velocity Error [mm/s]
0.459	0.17

Table 5.3: Position and Velocity errors from the desired point

from the approach cone, while respecting all the other constraints of the mission.

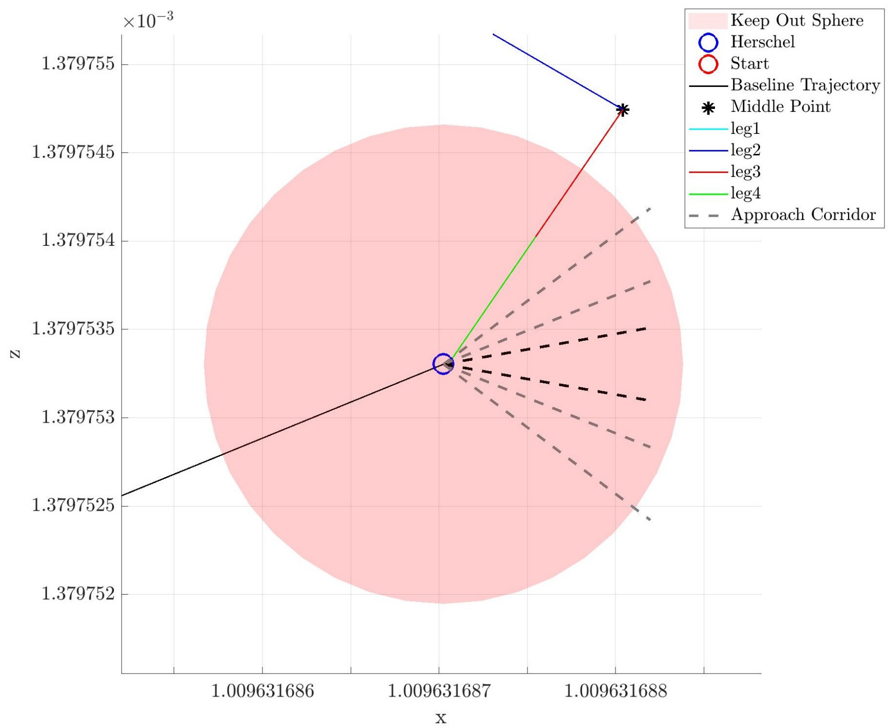

Figure 5.9: Rendezvous phase - zoom at final approach on the x - z plane

On the other hand, the asset of this manoeuvre, is the possibility of being performed with different times of flight. This means that, in case the observatory isn't visible by the antennas of the Deep Space Network (DSN) to establish a connection, the departure from the Moon can be delayed hour after hour until this condition is satisfied. In short, there are multiple launch windows for this mission and since the Earth revolves around its axis in more or less 24 hours, the mission can start at any hour of the day. Figure 5.11 shows a part of the manifold of trajectories that allow a feasible rendezvous. Only those lasting from 5 to 10 hours are inserted for visibility reasons, but the trend is an extension of the curve that takes the cargo behind Herschel for those lasting more than 10 hours and a reduction for those lasting less than 5. Table 5.4 contains the details of all the feasible rendezvous

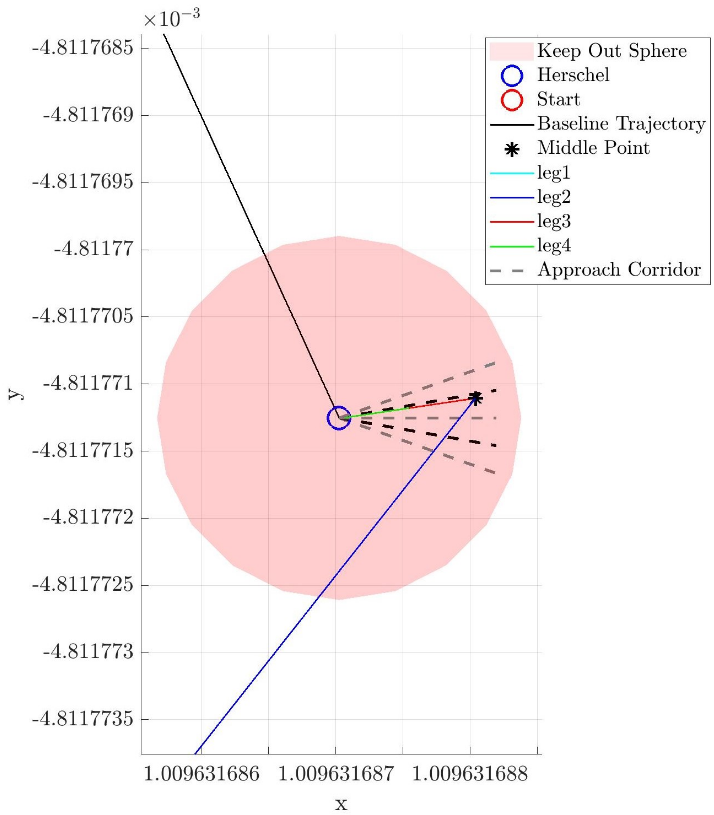

Figure 5.10: Rendezvous phase - zoom at final approach on the x - y plane

manoeuvres in terms of ΔV cost. It can be seen that, for the trajectories taking from 1 to 6 hours, the final impulse given at Herschel is in the order of few meters per second, whereas it becomes much smaller if the time of flight rises, reaching also values lower than millimeters per second. It is important to notice that the last impulse doesn't exceed the limit of 10 m/s imposed by the optimizer. Moreover, the distribution of the ΔV is mostly the same, with a big impulse at the start and approximately half of it at the middle point. The total ΔV needed for the manoeuvres is always around 510 m/s, which is about 100 m/s higher than the impulse calculated in the trajectory design from this point of the Lissajous orbit. The velocity error follows the trend of the last impulse as visible in figure 5.12, decreasing for higher times of flight. The position error is very low, in the order of 10^{-4} meters, for all the rendezvous manoeuvres.

To validate the values computed by the optimizer the trajectory in figure 5.8 has been obtained propagating forward each leg, instead of switching between backward and forward propagation, as set in the optimization problem. By doing so errors accumulate passing from one leg to another, but the overall performance remains

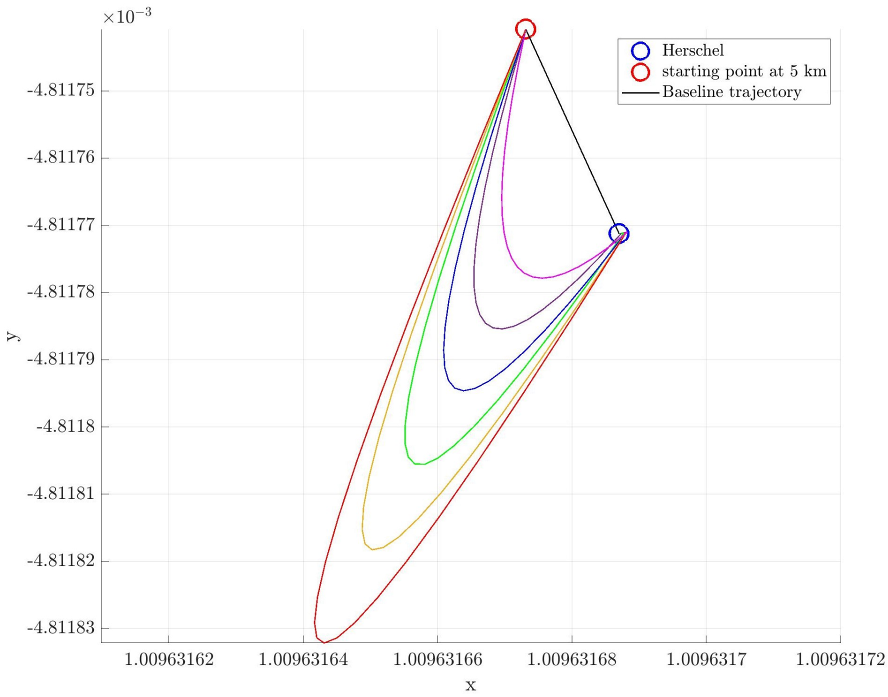

Figure 5.11: Manifold of rendezvous trajectories lasting from 5 to 10 hours

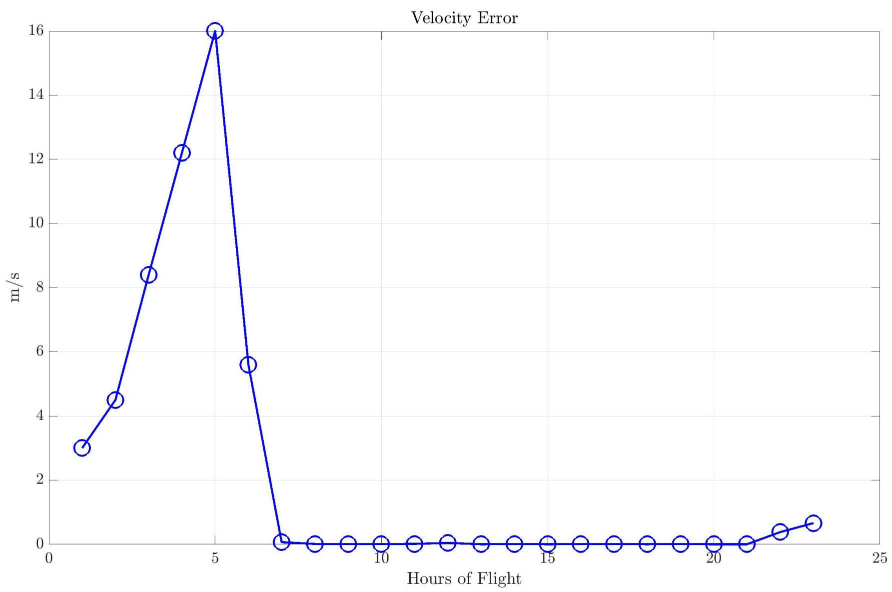

Figure 5.12: Velocity error per rendezvous manoeuvre at the final point

ToF [h]	ΔV_1 [m/s]	ΔV_2 [m/s]	ΔV_3 [m/s]	ΔV_{TOT} [m/s]
1	330.6	179.5	1.5	511.6
2	331.3	177.8	2.9	512
3	331.4	180.3	4.2	515.9
4	331.4	180.2	6.1	517.8
5	331.4	180.5	8	519.8
6	331.4	179.7	2.8	513.8
7	331.3	180.6	$7.6 \cdot 10^{-3}$	551.9
8	331.2	180.5	$5.2 \cdot 10^{-3}$	511.8
9	331.1	180.6	$1.1 \cdot 10^{-3}$	511.7
10	331.1	180.6	$2.9 \cdot 10^{-3}$	511.6
11	331	180.6	$5.8 \cdot 10^{-3}$	511.6
12	330.9	180	2.1	512.9
13	330.8	180.6	$3.4 \cdot 10^{-4}$	511.4
14	330.7	180.6	$5.1 \cdot 10^{-3}$	511.3
15	330.7	180.6	$6.2 \cdot 10^{-4}$	511.2
16	330.6	180.6	$2.9 \cdot 10^{-3}$	511.1
17	330.5	180.6	$4.9 \cdot 10^{-3}$	511
18	330.4	180.6	$7.4 \cdot 10^{-4}$	511
19	330.3	180.6	$4.5 \cdot 10^{-3}$	510.9
20	330.2	180.6	$3.7 \cdot 10^{-4}$	510.8
21	330	180.6	$4.5 \cdot 10^{-4}$	510.7
22	330	180.6	1.9	512.5
23	329.9	180.7	0.33	510.9

Table 5.4: Time of flight and magnitudes of the impulses given during each rendezvous manoeuvre

positive as shown by the final errors cited in table 5.3.

Hill dynamics The same optimization has been carried out with the Hill dynamics to compare the results with those obtained with the non - linear dynamics. The problem faced with the Hill dynamics resulted much dependent on the initial conditions given, since a small change brought to an unfeasible solution. For this reason very few simulations gave acceptable results, comparable to those obtained with the non - linear dynamics. Moreover, each leg of the trajectory needed to be propagated with at least 10 steps of resolution of the linear system in order to for the optimizer to converge. In this case, however, the error accumulated by propagating only forward from the starting point at 5 km were too big and didn't allow a feasible rendezvous. Results almost identical to the ones obtained with the non - linear dynamics can be achieved only by propagating the legs backward and forward as in the optimization problem. Only in this case, the results in terms of ΔV and times of flight are comparable to those obtained with the non - linear dynamics. The upside is that, unlike in the trajectory design, it wasn't necessary to give the point obtained by the non - linear propagation at each step of resolution of the linear system. Each point was computed from the one obtained with the linear propagation at the previous step. Moreover, the benefit of using the Hill dynamics lies in the computational time. In performing 10 optimization problems the simplified dynamics is only 10 seconds faster, in 50 is about 50 seconds faster. In short, the more optimization problems that have to be solved, the more evident the speed of the simplified dynamics is w.r.t. the non - linear one.

Chapter 6

Attitude Control

This chapter concludes the study carried on for the HRSM presenting the methodology employed for the attitude control.

Achieving and maintaining the desired attitude during a mission are the key elements that lead that mission to success. Without the right orientation of the spacecraft some activities couldn't be carried out at all, especially the ones involving an interaction between two or more vehicles. Attitude control in the CR3BP has already been addressed by Colagrossi and Lavagna [31], who developed an analysis tool applying it on a RdV scenario for a EML_2 orbit. They dealt with a coupled orbit/attitude control. Unlike it, the work carried out in this thesis, decouples the attitude dynamics from the orbital one.

The attitude of an object can be expressed in multiple ways. One of the most known parameterization is the Euclidean one, which makes use of three Euler angles used to describe a rigid - body rotation following a certain order. If the order of the rotation is changed while the angles are kept constant, then the final attitude reached changes too. The problem of this method is the presence of mathematical singularities, referred to as gimbal locks, due to the impossibility of the time derivatives of the Euler angles to represent certain angular velocities [32]. Derived from Euler parameters, there are the Rodrigues parameters. They are usually used for stabilizing only one axis instead of three, but they also present a singularity, geometrical in this case, since they are not defined for a rotation of 180° [32]. However, for the purposes of the HRSM mission, quaternions have been chosen as attitude parameterization. They are composed of 4 elements: one scalar and a vector. Through quaternions, all attitudes can be represented without singularities. For more details on quaternions, refer to Appendix B.

The following section describes how the different elements of the attitude control system have been implemented through SIMULINK. Refer to Appendix C for the visualization of the blocks of the model.

6.1 Attitude model

The model presented features the kinematics, the dynamics, the control and the actuation involved.
In general, a Guidance, Navigation & Control *(GNC)* system is made of three parts: a guidance algorithm that defines the desired path, a control algorithm that computes the needed force or torque that the actuators have to execute to achieve the desired state and a navigation algorithm, which estimates the state of the S/C after the actuation using various sensors. The output is the actual state, which is then compared to the desired state and the error between the two is given as input to the guidance law. This cycle is performed during the entire manoeuvre. Usually errors in the measurements or in the actuation, added to the external disturbances, make this algorithms very difficult to tune. The mission, however, is at a first stage of development and the structure, systems and features of the cargo spacecraft are not completely defined yet. Many assumptions, then, have been made in order to obtain results for a simple control methodology, and it is for this reason that the model doesn't include sensor noises, but it assumes that the state computed by the kinematics and the dynamics after the application of the control torques is the one estimated by the sensors.
Moreover, external disturbances are neglected for the following reasons:

- Atmospheric Drag is absent at SEL_2 because of its distance from Earth;
- Magnetic torques are excluded since the libration point is highly beyond the external Van Allen belt;
- The Gravity Gradient *(GG)* torque is very small. The observatory revolves around an equilibrium point, meaning that the sum of all the gravity forces acting on the body is almost zero. This implies that the torques exerted by these forces are negligible. A fast analysis of the GG torques points out that the magnitude of this disturbance is around 10^{-41} $N \cdot m$ for the x and y component, whereas the z component is around 10^{-60} $N \cdot m$. Figure 6.1 shows the trend of the GG torque during the RdV manoeuvre, portrayed in figure 5.8, when the S/C is not controlled. As visible, the torques can be neglected because their influence on the dynamics is almost null;
- The Solar Radiation Pressure is the most important disturbance for this scenario, since the particles coming from the Sun reach very far distances and generate torques while hitting the spacecraft. In order to compute the magnitude of this disturbance however, some details of the structure of the cargo are needed, such as the material and its reflectivity. These data are not available yet and it is believed that the effect on the control wouldn't be too high, therefore, this disturbance is neglected as well.

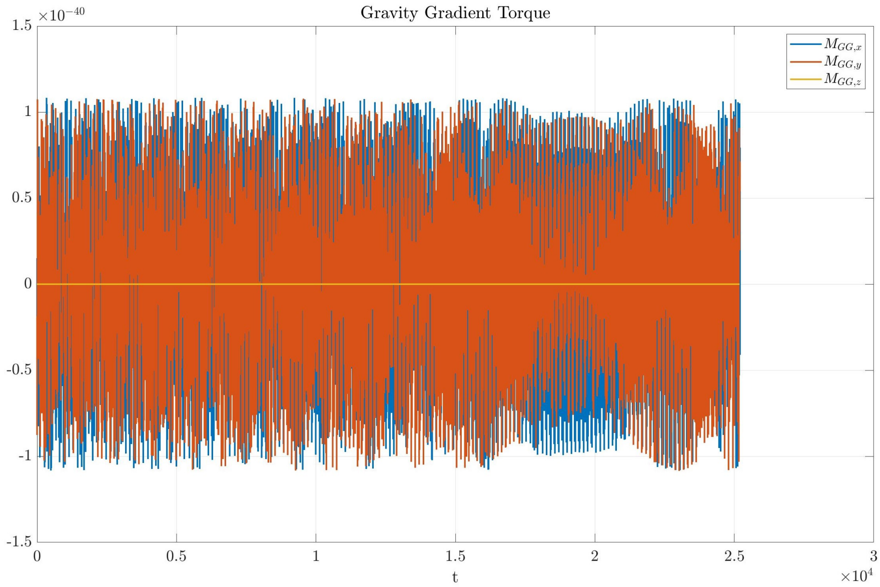

Figure 6.1: Gravity gradient torques on the uncontrolled cargo spacecraft during the rendezvous phase

The current available details of the cargo S/C are its body frame and its inertia matrix. The body frame has its origin at the cargo's centre of mass and three axes coincident with the three principal axes of inertia. It features the cryostat in the positive z direction and the main thruster opposite to it, whereas the camera is in the positive x direction. The inertia matrix provided is

$$\mathbb{J} = \begin{bmatrix} 1.3222018202455 & 0 & 0 \\ 0 & 1.3222018202455 & 0 \\ 0 & 0 & 0.5505694006284 \end{bmatrix} \cdot 10^4 \quad Kg \cdot m^2$$

calculated in the body frame of the cargo in order to be considered constant. The inertia matrix highlights that the S/C is symmetrical around the z - axis.

6.1.1 Dynamics & Kinematics

The dynamics used involves Euler's equations:

$$\mathbb{J}^b \dot{\boldsymbol{\omega}}^b = -\,\boldsymbol{\omega}^b \times \mathbb{J}^b \boldsymbol{\omega}^b + \boldsymbol{M}^b_{app} \tag{6.1}$$

where $\mathbb{J}^b$ is the aforementioned inertia matrix, $\boldsymbol{\omega}^b$ is the angular velocity vector, $\dot{\boldsymbol{\omega}}^b$ is the angular acceleration and $\boldsymbol{M}^{\mathrm{b}}_{\mathrm{app}}$ is the vector of the applied torques. Just as $\mathbb{J}^b$, all the variables are expressed in the body frame. As previously stated,

no disturbance is taken into account, therefore the applied torque is just the one generated by the controller to cancel the error relative to the desired attitude.
The kinematics of a rigid body can be expressed as:

$$\dot{\mathfrak{q}}^{ib} = \frac{1}{2}\mathfrak{q}^{ib} \circ \boldsymbol{\omega}^{b} \tag{6.2}$$

where $\mathfrak{q}^{ib}$ is the quaternion that rotates any vector expressed in the body frame to its inertial frame counterpart and $\dot{\mathfrak{q}}^{ib}$ is its time derivative.

6.1.2 Controller

The control technique employed is an error - quaternion feedback control [33], which allows the computation of the control torque needed to reach the desired attitude in absence of noise:

$$\boldsymbol{M_{ctrl}}^{b} = \boldsymbol{\omega}^{b} \times (\mathbb{J}^{b}\boldsymbol{\omega}^{b}) - \mathbb{K}_{d}\, \boldsymbol{\omega}_{e} - q_{e,0}\mathbb{K}_{p}\, \boldsymbol{q}_{\mathrm{e}} \tag{6.3}$$

where $\mathbb{K}_{\mathrm{d}}$ and $\mathbb{K}_{\mathrm{p}}$ are positive definite gain matrices, $\mathrm{q}_{\mathrm{e},0}$ is the scalar part of the error unit quaternion, $\boldsymbol{\omega}_{\mathrm{e}}$ is the error angular velocity vector and $\boldsymbol{q}_{\mathrm{e}}$ is the vectorial one.
The error quaternion is defined as:

$$\mathfrak{q}_{e} = \tilde{\mathfrak{q}}_{d} \circ \mathfrak{q}^{ib}$$

where $\tilde{\mathfrak{q}}_{d}$ is the quaternion conjugate of the desired quaternion.
On the other side, the error angular velocity is defined as:

$$\boldsymbol{\omega}_{e} = \boldsymbol{\omega}^{b} - \boldsymbol{\omega}_{d}$$

where $\boldsymbol{\omega}_{d}$ is the desired angular velocity that satisfies the kinematic constraints (6.3) and can be computed from the desired quaternion as $\boldsymbol{\omega}_{d} = 2\tilde{\mathfrak{q}}_{d} \circ \ddot{\mathfrak{q}}_{d}$.

6.1.3 Actuator

Since no actuation system has been chosen yet, simple thrusters are assumed for this study. Herschel, with its 3300 kg of mass employed 20 N monopropellant thrusters for the attitude control [34]. The weight of the cargo S/C at the moment is estimated to be 5050 kg at beginning of life *(BoL)*, with all the propellant stored inside. Thus, the same thruster are used as actuators for the mission.
By knowing only a general shape of the cargo spacecraft, 4 thrusters are dedicated to each axis, 2 per side, allowing a full attitude control around each axis. Figures 6.2 and 6.3 show the projections, on the x - y plane and y - z plane respectively, of the cargo spacecraft. The thrusters are located along the axes and positioned

so that the exhaust doesn't hit the square platform where the camera is located. The signs + and - indicate the direction of the generated torque w.r.t. the body axes. This placement allows to have a net force equal to 0 so that the orbit is not perturbed and only the attitude is changed.

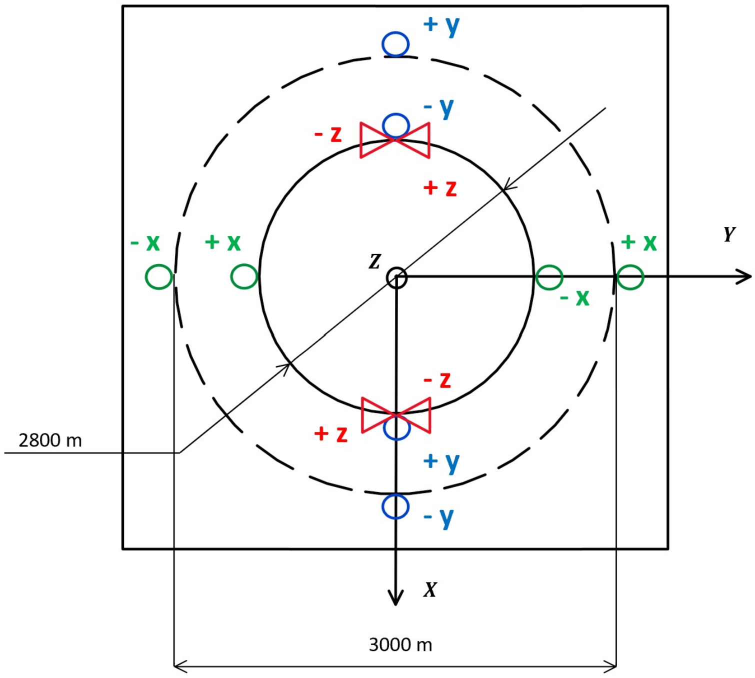

Figure 6.2: Projection on the x - y body plane of the cargo spacecraft with the thrusters location

Figure 6.2 also displays the dimension from which the arms of the torques can be derived. The arms w.r.t. the x and y axes are different because the thrusters are located on cylinders of different radii. On the contrary, the thrusters that control the rotation around the z - axis are placed on the same cylinder, thus the arms are equal. The vector of the total arm is $\mathbf{b} = [2.9 \;\; 2.9 \;\; 2.8]^{\mathrm{T}}$ m, which brings to a maximum torque vector equal to $\boldsymbol{T}_{\mathrm{c}} = \pm\mathrm{F} \cdot \boldsymbol{b} = \pm[58 \;\; 58 \;\; 56]^{\mathrm{T}}$ $\mathrm{N \cdot m}$ when all the torques are on, where F = 20 N.

In order to assure that these limits are not exceeded during the thrusts, a Schmidt Trigger *(ST)* has been implemented. The ST (see Appendix C) is mainly a relay with dead - band/hysteresis, advantageous for its simplicity, but strongly dependent on the inertia of the S/C. For single axis control, the system can be defined using two equations [35]:

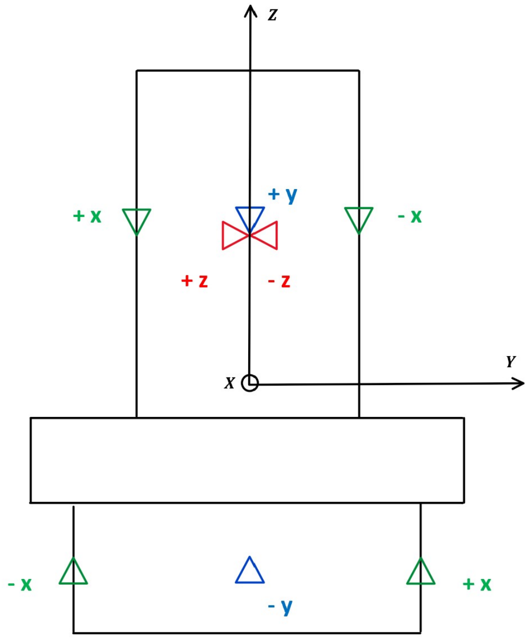

Figure 6.3: Projection on the y - z body plane of the cargo spacecraft with the thrusters location

$$\text{Minimum Pulse Width} = \frac{J\,h}{\tau\,T_c} \tag{6.4}$$

$$\text{Limit Cycle Amplitude} = \frac{T_c\,(U_{on} + U_{off})}{2} + \frac{J^2\,h^2}{8\,\tau} \tag{6.5}$$

where $\mathrm{h} = \mathrm{U_{on}} - \mathrm{U_{off}}$ and τ is the linear switching line slope, the tunable parameter dependent on the two gains $\mathrm{K_p}$ and $\mathrm{K_d}$, which are scalar values for single axis control.
The first equation delivers the width h, after the minimum pulse width is obtained. This values is linked to the minimum impulse bit *(MIB)*, acquired from the data sheets of the thrusters, as $\mathrm{MIB} = \Delta\mathrm{t} \cdot \mathrm{T_c}$, with Δt being the minimum pulse width. For the 20 N monopropellant thrusters used, $\mathrm{MIB} = 0.238\ \mathrm{N \cdot m \cdot s}$. The parameter h is calculated considering the worst case scenario, meaning that $\mathrm{J} = \mathrm{J_z}$ because it is the lowest value of the inertia matrix and is more affected by the dynamics, therefore it needs to be controlled more than the other axes. Consequently $\mathrm{T_c} = \mathrm{T_{c,z}} = 56\ \mathrm{N \cdot m}$. Once h is found, either $\mathrm{U_{on}}$ or $\mathrm{U_{off}}$ has to be chosen. The equation (6.5) links both of them to the limit cycle amplitude *(LCA)*, which becomes the second tunable parameter.

The tuning is performed by observing how the control law improves the convergence to the desired attitude by changing the gains and how the actuators perform better by changing the LCA. The parameters obtained from the tuning of the system are shown in table 6.1.

K_p	K_d	τ	LCA	U_{on}	U_{off}	h
1	17.0213	17.0213	0.025	-0.0013	-0.0021	$7.358 \cdot 10^{-4}$

Table 6.1: PD gains and Schmidt Trigger parameters

6.2 Simulations

The goal of the attitude control is double:

- Aligning the main cargo thruster to the direction of the $\boldsymbol{\Delta V}_s$ at each burn;
- Maximizing Herschel's visibility for the camera.

Firstly, the simulations carried out are focused on achieving each condition separately and only after a final simulation for both is executed.
Knowing how the body frame of the cargo S/C is oriented, the first point implies that the negative z - axis of the cargo has to be aligned to the $\mathbf{\Delta V}$ vectors at 5 km, at the middle point and at the final point. The starting point at 5 km is set as initial condition, therefore the cargo is assumed to be already oriented correctly. The attitude control in this case consists only in a sequence of slew manoeuvres in which the cargo's attitude is changed during the trajectory to reach the final desired attitude at the burns, but without chasing any particular condition in between. The second condition implies that the positive x - axis points always to Herschel. In this case the attitude control consists in a tracking manoeuvre in which the desired attitude changes every instant while the cargo moves in space.

6.2.1 Slew Manoeuvre

The slew manoeuvre is aimed at aligning the main cargo thruster, positioned along the negative z body axis, to the direction of the $\boldsymbol{\Delta V}_s$ given during the rendezvous phase. The S/C starts with the main thruster aligned with the direction of $\boldsymbol{\Delta V}_1$ at 5 km and a random $\boldsymbol{\omega}^{\mathrm{b}}$, then the attitude control system aligns it to the $\boldsymbol{\Delta V}_2$ and, after the impulsive burn, the desired alignment direction switches to $\boldsymbol{\Delta V}_3$, where the manoeuvre ends. The PD controller included in the error - quaternion feedback control is optimal for the slew manoeuvre and its performance can be assessed in

figure 6.4, which presents the variation of the quaternion error, quaternions and angular error during the whole manoeuvre. Zooming in (figure 6.5) it can be seen that the controller takes less than 4 minutes to bring the angular error below 1°. For the rest of the manoeuvre, the error remains between 0.1° and 0.2°, except for the peak visible in figure 6.4 that represents the change of the desired quaternion after the burn at the middle point is executed. At that moment, the control system starts chasing the final attitude in which the negative z body axis is aligned to $\boldsymbol{\Delta V}_3$. This simulation shows how the control is considerably fast if compared to the duration of the leg from the starting to the middle point, therefore, in case only the slew manoeuvre was to be performed, the control can be started few minutes before the middle point is reached in order not to waste fuel for nothing. The mass flow rate for a single thruster ranges between $\dot{m} = 3.2$ g/s and $\dot{m} = 10.4$ g/s. The average of this range is $\dot{m} = 6.8$ g/s, therefore, in case the control was performed for the entire RdV phase the total mass burnt would be 100 g of propellant. Instead, by choosing to activate the actuators 1500 seconds before it, the fuel consumption lowers to 24.6 g of propellant, less than a fourth of the previous case. The system is uncontrolled until the controller is activated, as figures 6.6 and 6.7 show. By activating the controller 1500 seconds before reaching the middle point the angular error at that point is 0.1786°. As a matter of fact, the convergence of the manoeuvre is much faster, therefore the controller could be activated only 300 or 400 seconds before the middle point is reached. Nevertheless, by doing so, the angular error at the final point would be higher than it is with this configuration, that is to say 0.0619°. Priority has been given to reducing the error at the final point instead that having it lower at the middle point, since the former is the closest point to Herschel, where the mating operations should begin.
Figure 6.8 shows the control and the applied torques during the whole manoeuvre. The control torques point out as well how the control ends in few minutes, but the limitations due to the thrusters capabilities cause the applied torques to be distributed all over the transfer. The number of burns of the thrusters can be subject of an optimization problem aimed at minimizing the total fuel burnt.

6.2.2 Tracking Manoeuvre

In order to maximize Herschel's visibility, the camera of the cargo spacecraft needs to be pointed towards the observatory. Therefore, between the impulse at 5 km and the one at the middle point, the x body axis must be aligned to the vector that links Caroline to Herschel. This vector is essentially the opposite of the relative position of the chaser w.r.t. the target. The tracking control is implemented only between the first two impulses because the time employed to go from the middle to the final point is too short and allows to execute only the slew manoeuvre. The results in terms of attitude are shown in figure 6.9. The error quaternion decreases

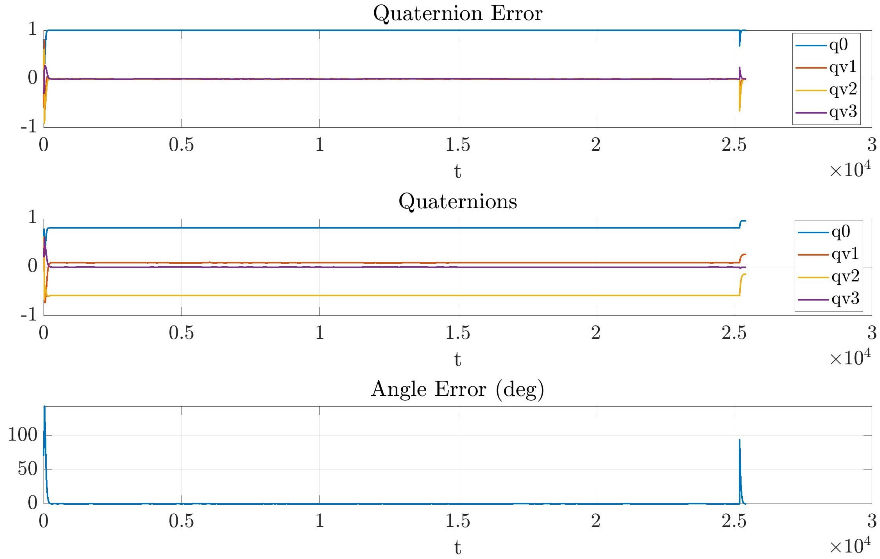

Figure 6.4: Slew manoeuvre

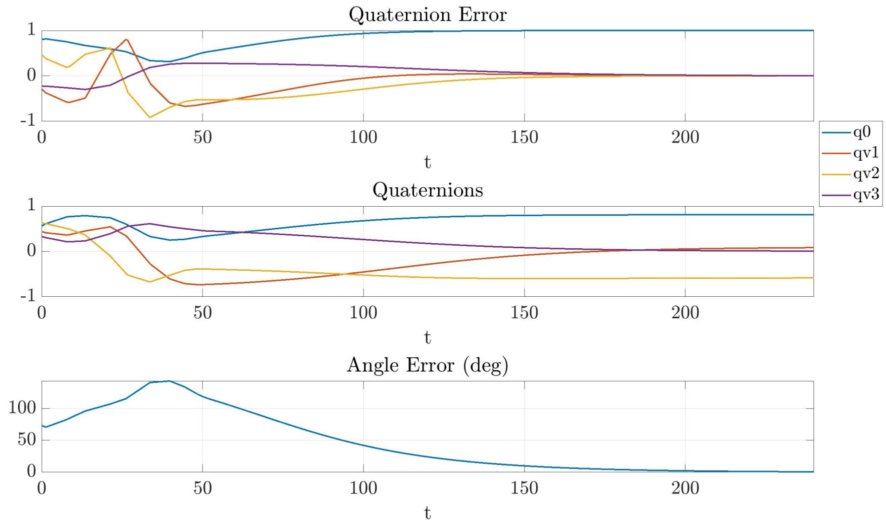

Figure 6.5: Slew manoeuvre zoomed in the first 4 minutes

to 0.28° very fast, as highlighted in the zoom of the first 4 minutes in figure 6.10, and stays below 0.3° for all the duration of the tracking manoeuvre. In this case the angular error goes to 360° which is the same as 0°. Normally this kind of controller would be too simple for a tracking problem, but the simulations proved that the slow changing rate of the quaternions, visible in the second graph of figure 6.9, enhanced the performance of this simple controller for this particular case and

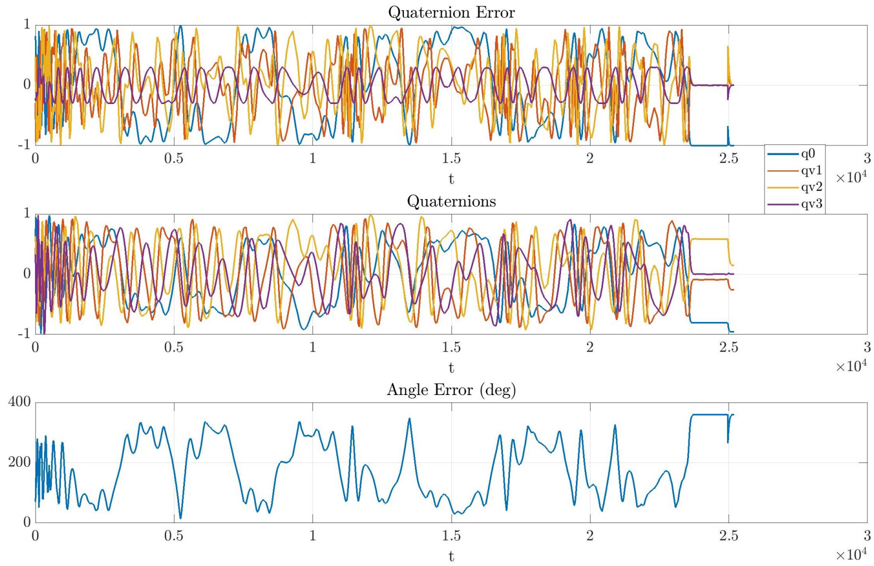

Figure 6.6: Quaternion error, quaternions and angular error starting the control 1500 seconds before reaching the middle point

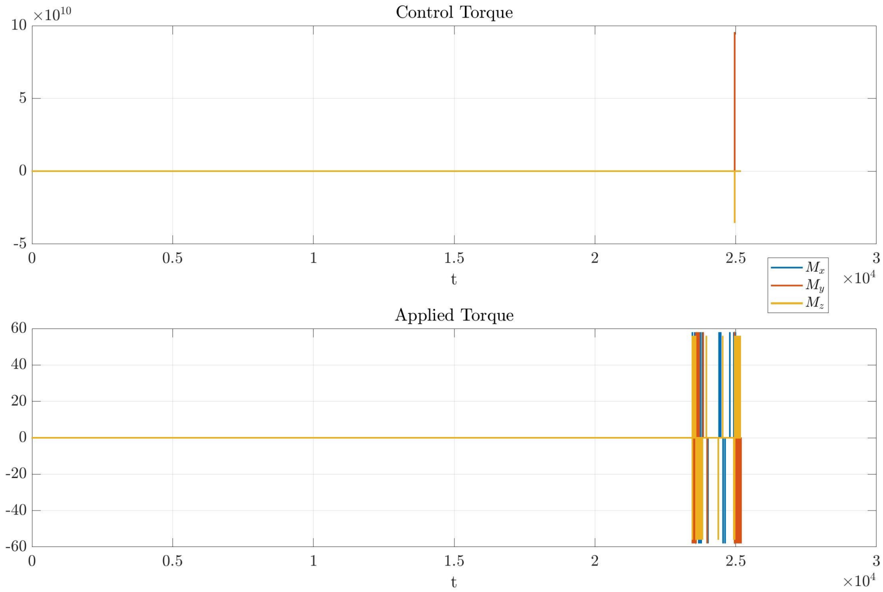

Figure 6.7: Control and applied torques starting the control 1500 seconds before reaching the middle point

allowed it to perform well nonetheless.

Figure 6.11 displays the control and applied torques. As well as for the slew

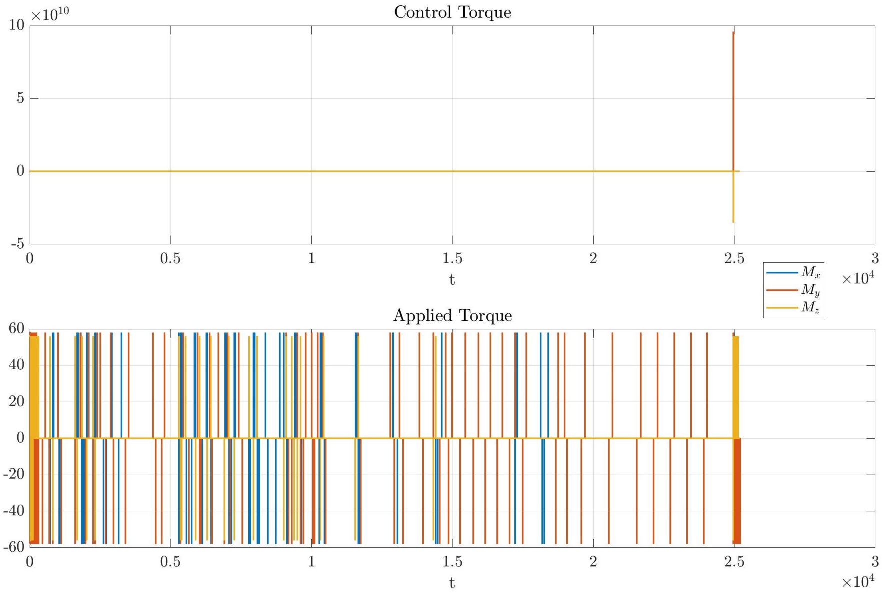

Figure 6.8: Control and applied torques during the slew manoeuvre

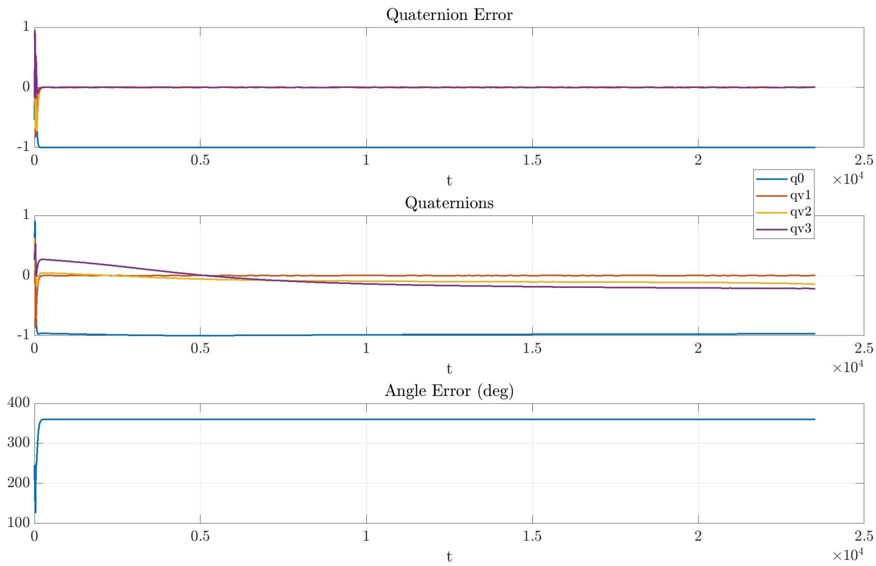

Figure 6.9: Tracking manoeuvre

manoeuvre, the thrusters work for all the duration of the simulation, even though the control torque is different from 0 only at the beginning, when the system struggles to align the cargo to the desired attitude. Once again, this is due to the short working time of the thrusters, linked to the h parameter, and it can be

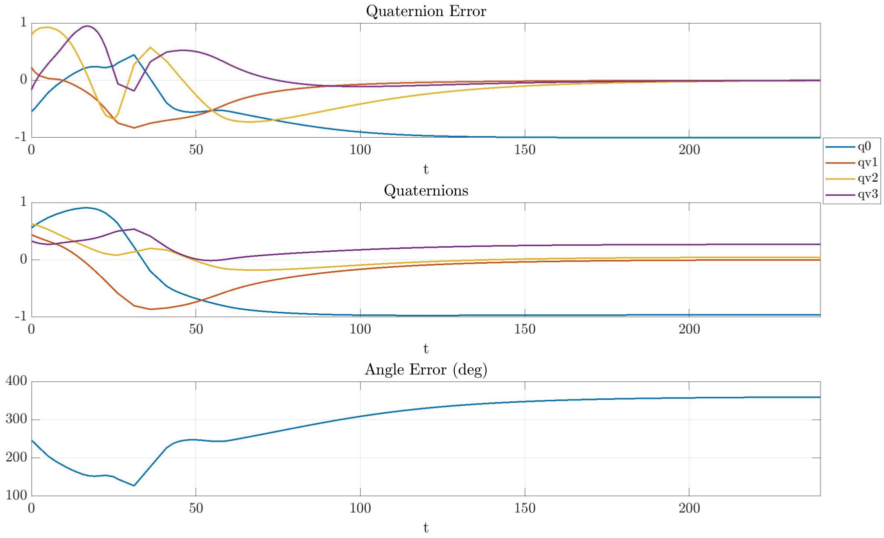

Figure 6.10: Tracking manoeuvre zoomed in the first 4 minutes

subject of an optimization problem once again.

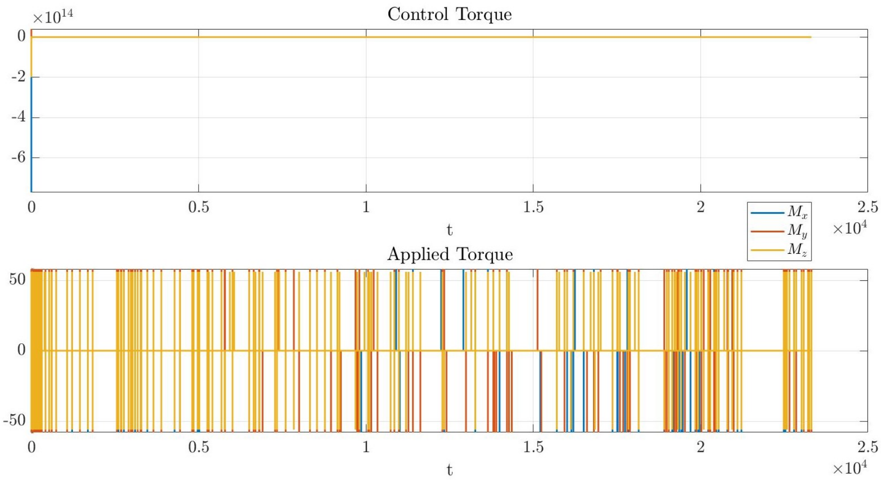

Figure 6.11: Control and applied torques during the tracking manoeuvre

The mass of fuel consumed for the tracking manoeuvre is m = 24.3288 kg, much higher than the slew one. This result was expected since the spacecraft needs to be controlled all the time until the slew manoeuvre starts, which, in fact, represents only the 7 % of all the RdV phase.

6.2.3 Slew + Tracking

The complete manoeuvre is finally implemented. Starting from the 5 km of distance from Herschel, tracking starts, in order to align the camera towards Herschel. This attitude is maintained during most of the trajectory until the cargo S/C is close to the middle point. 1500 seconds before reaching it, the desired quaternion switches to the direction of $\boldsymbol{\Delta V}_2$ and the first slew manoeuvre starts. After the burn is executed, the second slew manoeuvre starts in order to align the main thruster to the direction of $\boldsymbol{\Delta V}_3$, where the control ends. Figure 6.12 shows the variation of the quaternion error, quaternions and angular error for the whole simulation. It can be seen that, when the desired attitude is changed to start the two slew manoeuvres, there is a peak, but they are soon flattened by the control system that brings the error close to 0 again. The peaks are visible in the angular velocity and angular velocity error as well, displayed in figure 6.13, just in the position where the attitude control starts chasing another configuration.

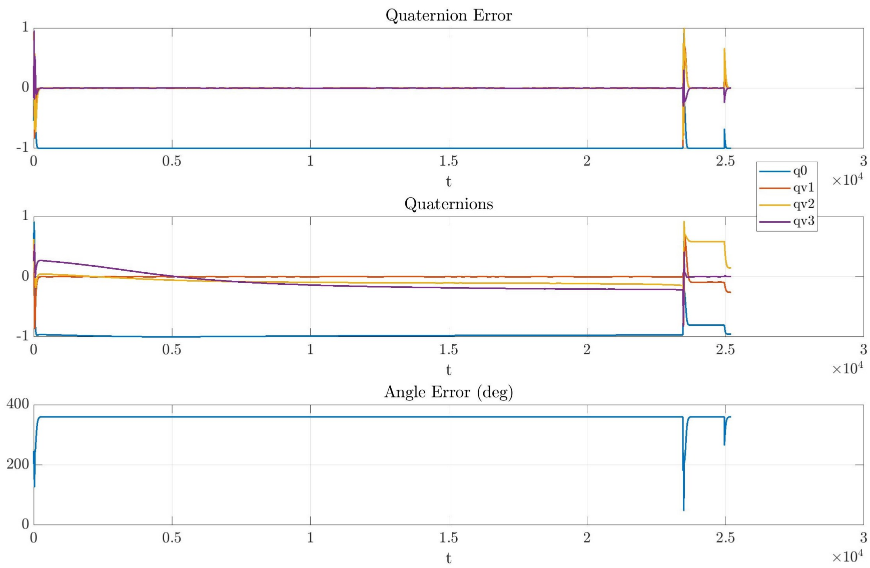

Figure 6.12: Quaternion error, quaternions and angular error for the whole manoeuvre

Figure 6.14 shows the control and applied torques, which, similarly to the previous cases, point out how the high torque necessary to align the chaser to the desired attitude is spread all over the rendezvous phase. The zoom in figure 6.15 shows two smaller peaks in the control torques that the control system generates at the switch from one desired attitude to the other. Therefore, the first one represent the switch from tracking to slew 1 and the second from slew 1 to slew 2.
The fuel needed in case both the manoeuvres are performed is m = 24.3652 kg,

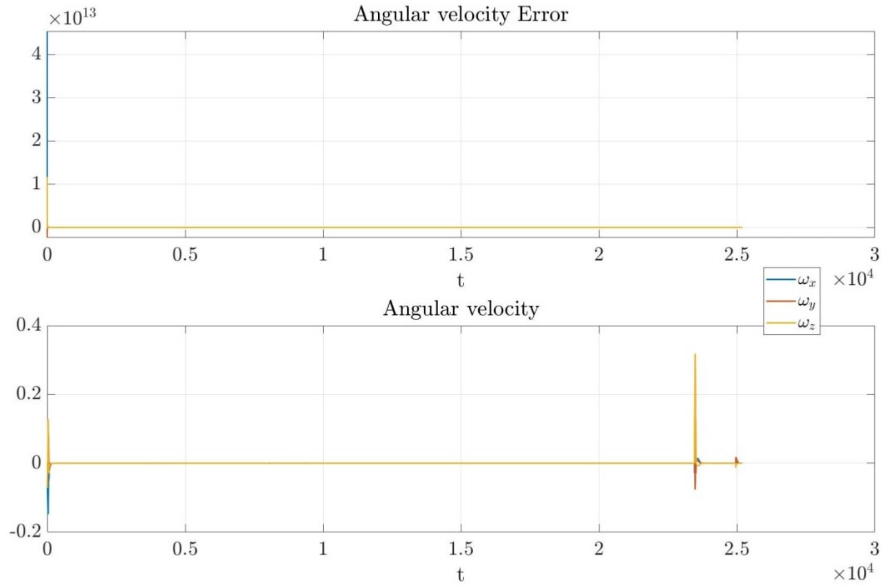

Figure 6.13: Angular velocity error and angular velocity for the whole manoeuvre

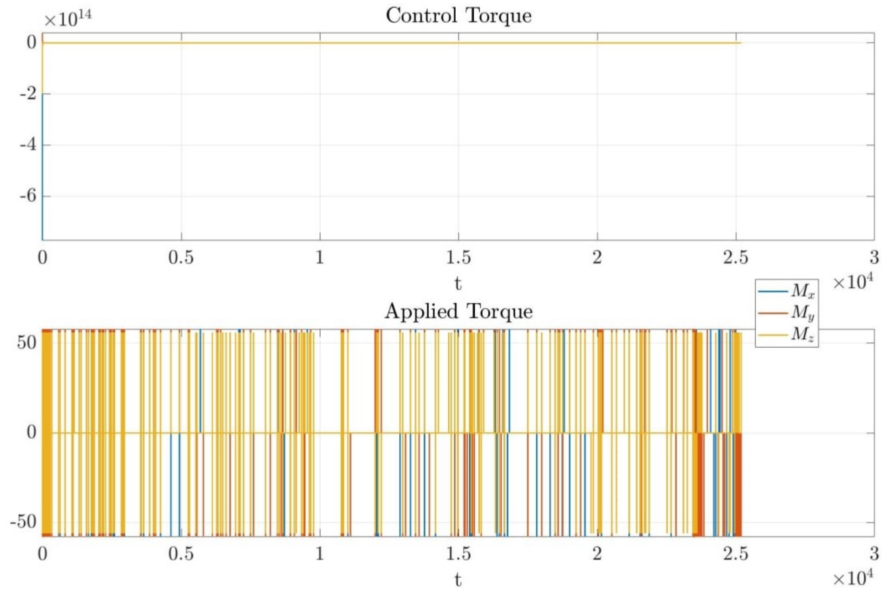

Figure 6.14: Control and applied torque for the whole manoeuvre

where the fuel consumed for the tracking manoeuvre is 99 % of the total, the 24.3288 kg seen before. The remaining 36.4 g are used for the slew manoeuvres in the last part of the RdV phase. The amount of fuel consumed when only the two slew manoeuvres are performed is slightly lower, 24.6 g, and this is due to the fact

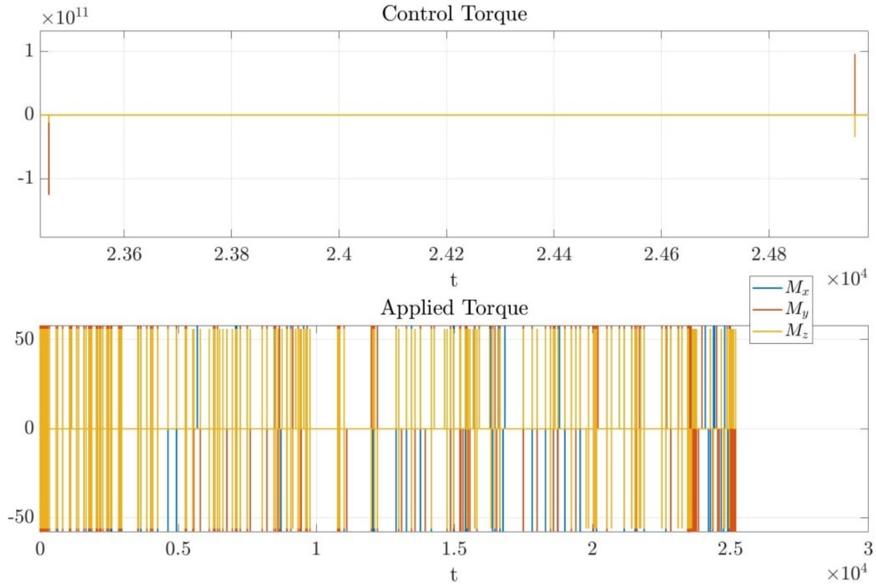

Figure 6.15: Peaks in the control torques needed to re - align the cargo S/C after the switch in the desired attitude

that, in this case, the attitude when the first slew manoeuvre starts is different from the case studied previously, since the S/C was in the tracking mode. The difference, however, consists only in few g of propellant.
The results obtained could be changed according to the needs of the mission. If the main objective is minimizing the mass on board, the tunable parameters of the ST can be changed so that the thrusters would activate less times during the manoeuvre, ending up with a higher final angular error, but gaining in quantity of fuel consumed.
The attitude control is independent of the orbit described by the chaser during the rendezvous phase. This is mainly due by the absence of perturbation in the model used. Therefore, each one of the manoeuvres computed in the previous chapter, lasting different times, can be controlled in the same way this one was. Clearly, those taking less time will have a lower fuel consumption that those employing more hours to reach Herschel. By taking into account the departure time from the Moon, the time of flight of the RdV phase and the transportable mass on board, the final path for the HRSM mission can be determined.

Chapter 7

Conclusions & Future Work

This thesis presents a study involved in the assessment of a possible baseline mission for the re - supply of the Herschel space observatory, launched by the European Space Agency into a Lissajous orbit around the Sun - Earth L_2 point, that has run out of its coolant. The mission is envisaged in a near future where a modern and autonomous human outpost will be available on the Moon to exploit its resources and extend space missions. The mission foresees the adaptation of one of the vehicles used on the lunar base to a cargo spacecraft, that will be launched from the Moon itself and travel towards Herschel to perform rendezvous and docking operations in order for the refueling to start. The system composed of the two vehicles will be controlled until the cargo spacecraft recedes and returns on the Moon, where it will be refilled again for another departure. This mission, in fact, is intended to be performed multiple times, until the space observatory is fully working. The cargo spacecraft will be filled with 3000L of ^{4}He, the coolant needed by the observatory to work, therefore the first part of the mission is aimed at collecting, storing and liquefying the Helium. The thesis deals with the orbit and attitude control of the spacecraft for rendezvous and docking at Herschel.
Chapter 3 displays the work done to find a feasible trajectory that connects Herschel to the Moon. 90 points of the Lissajous orbit have been considered and a grid search has been performed on each of them to find such trajectory, obtained by backward propagating Herschel's state on the Lissajous orbit perturbed by an impulse. The grid search allowed finding the ΔV that needs to be added to Herschel's velocity in order to reach the Moon.
Chapter 4 presents two linearization techniques introduced to simplify the 3 - body dynamics and speed up the simulations. A first order Taylor expansion of the equations of motion and the Hill dynamics have been compared and applied to the trajectories found in order to assess which is faster and displays less linearization errors. Different propagation techniques have been introduced, such as numerical methods employed by the `ode45` `MATLAB` function and linear system resolution

by computing a state transition matrix in two different ways. Since the thesis deals with the close proximity operation phase, the different techniques have been compared on the last 5 km from Herschel and one of them has been chosen. The fastness of the two approximations turned out to be comparable, but the Hill dynamics performed slightly better than the Taylor approximation, therefore has been chosen as linearization technique.
Chapter 5 presents a multiple shooting technique employed to approach Herschel according to the constraints of the mission. Herschel's sunshield faces the Sun, forcing the approach to take place on its back, along the positive synodic x - axis. Therefore, the multiple shooting technique has the goal of deviating the cargo spacecraft from the baseline trajectory, reaching Herschel from the front, in order to achieve a flanking manoeuvre and bring the cargo spacecraft behind Herschel, with an almost null relative velocity, in a position where the mating operations can begin. The time of flight, position, magnitude and direction of the impulses given are computed for the manoeuvre. Simulations have been carried out with both the non - linear and the Hill dynamics and the results pointed out that, even if more sensitive to the initial conditions, the simplified dynamics is faster than the non - linear one and brings to similar results. Moreover, the solutions found appeared to be feasible for times of flight from 1 to 23 hours, meaning that the mission from the Moon can start at any time of the day and it is possible to wait for a full cover of the satellite link between the DSN, the cargo spacecraft and Herschel.
Chapter 6 ends the study by presenting a simple control technique performed during the rendezvous phase. The configuration of the cargo spacecraft is not completely known yet therefore, simple thrusters have been assumed for the actuation and an error - feedback quaternion control has been implemented. The goal of the attitude control is to align the cargo main thruster to the direction of the burns given during the approach and maximize Herschel's visibility for the camera provided to the cargo spacecraft. A slew manoeuvre, a tracking manoeuvre and the combination of the two have been implemented, their performance assessed and the cost in terms of fuel consumed calculated. The control low turned out to be flawlessly suited for the slew manoeuvre and performed very well for the tracking phase too thanks to the slow changing rate of quaternions during the approach.
The only drawback of the solutions obtained for the rendezvous phase is that the final leg of the approach is not restrained in the approach cone in the x - z plane, whereas no problems are encountered in the x - y plane. Therefore, future works foresee a better adaptation of the final approach to align with the corridor for docking. Furthermore, the spacecraft will be provided with robotic arms for the clamping sequence during docking operations, therefore the attitude control will be adapted to compensate for the angular rates induced by the movements of these robotic arms.

Appendix A

SPICE Kernels

In this thesis the data used for the study have been extracted from SPICE kernels. In order to do this the function *cspice_spkezr* has been used provided with the following inputs [26]:

- ID code or name of the target bodies. In this case, Sun, Earth - Moon barycenter, Moon, L_2 and Herschel;
- Time span expressed in seconds, in this case six months have been considered, from the 5^{th} of June 2009 to the 5^{th} of December 2009, that is the first half year of operation of the observatory. Actually the dates are not fundamental even though the Lissajous orbit is not periodic because adjustments are done through SK manoeuvres, making the orbit periodic;
- String name of the reference frame in which the ephemeris are represented, in this case `'ECLIPJ2000'`, that would be the mean ecliptic and equinox of J2000;
- A string to consider the planetary or stellar aberration corrections. In this case there is no aberration, so the string is put to `'none'`;
- The ID code of the observing body. In this case the ephemerides are seen from the Sun, so the string is whether `'10'` or `'Sun'`.

For the extraction of these data, other files must be loaded in the MATLAB script, so that SPICE can access the right ephemerides kernels:

- NAIF0012.TLS.PC, a leapseconds kernel file (LSK) needed for all SPICE computations involving times. There are many versions of this file, this is the latest one updated running on Windows;

- DE430.BSP, the main ephemeris kernel released by JPL's Solar System Dynamics Group, which contains data for the planets from Mercury to Pluto plus the Sun and the Moon (SPK). This file is the most accurate if compared with DE431 because the dynamical model of the Moon includes an excited lunar core/mantle rotation interaction so it results being more accurate. The only limit of this data file is that it doesn't work well in the far past, so its use is recommended between January 01 1550 and January 22 2650, a period that perfectly covers Herschel lifetime;
- L2_DE431.BSP, the SPK file for the second Lagrangian point of the Sun - Earth/Moon system, based on the DE431 planetary ephemeris. It is valid from January 01 1900 to January 01 2151;
- GM_DE431.TPC, a mass kernel that contains the gravitational constants μ of the Sun, planets, planetary systems and some asteroids. The values are likewise based on the DE431 file;
- PCK00010.TPC, PCK file that contains orientation data for planets, natural satellites, Sun and some asteroids.

Appendix B

Quaternions Fundamentals

Quaternions have been used in this thesis as attitude parameterization method and to transform a vector from a frame to another. In this section the fundamental mathematical relations of quaternions are reported.
A quaternion is a 4 element vector that describes the rotation of an angle θ about an axis defined by a unit vector $\boldsymbol{a} = a_1 \hat{\boldsymbol{i}} + a_2 \hat{\boldsymbol{j}} + a_3 \hat{\boldsymbol{k}}$. The elements are defined as

$$\begin{cases} q_0 = \cos\frac{\theta}{2} \\ q_1 = a_1 \sin\frac{\theta}{2} \\ q_2 = a_2 \sin\frac{\theta}{2} \\ q_3 = a_3 \sin\frac{\theta}{2} \end{cases}$$

A 3D vector is considered to be a quaternion with a 0 scalar part.
A unit quaternion $\mathfrak{q} = \begin{bmatrix} q_0 & \boldsymbol{q} \end{bmatrix}^T$ satisfies the relation $\boldsymbol{q}^T\boldsymbol{q} + q_0^2 = 1$. This quaternion implies that no rotation is verified between the two reference systems. The unit quaternion that describes the transformation of a vector from frame $\mathcal{F}^x$ to the frame $\mathcal{F}^y$ is $\mathfrak{q}^{yx} = \begin{bmatrix} q_0 & \boldsymbol{q} \end{bmatrix}^T$ and it implies that the representations of any vector in these frames are related by

$$\boldsymbol{r}^y = \mathfrak{q}^{yx} \circ \boldsymbol{r}^x \circ \tilde{\mathfrak{q}}^{yx}$$

where $\circ$ denotes the quaternion multiplication operator and $\tilde{\mathfrak{q}}^{yx} = \mathfrak{q}^{xy} = \begin{bmatrix} q_0 & -\boldsymbol{q} \end{bmatrix}^T$ is the conjugate quaternion of $\mathfrak{q}^{yx}$.
Given two quaternions $\mathfrak{q} = \begin{bmatrix} q_0 & \boldsymbol{q} \end{bmatrix}^T$ and $\mathfrak{p} = \begin{bmatrix} p_0 & \boldsymbol{p} \end{bmatrix}^T$ the quaternion multiplication is performed as:

$$\mathfrak{q} \circ \mathfrak{p} = \begin{bmatrix} q_0\, p_0 - \langle \boldsymbol{q}, \boldsymbol{p} \rangle \\ q_0\, \boldsymbol{p} + p_0\, \boldsymbol{q} + \boldsymbol{q} \times \boldsymbol{p}. \end{bmatrix}$$

According to the previous equation, the following property can be proven for any two unit quaternions $\mathfrak{q}$ and $\mathfrak{p}$:

$$\widetilde{(\mathfrak{q} \circ \mathfrak{p})} = \tilde{\mathfrak{p}} \circ \tilde{\mathfrak{q}}$$

The direction cosine matrix *(DCM)* is the matrix of dot products representing the orientation of each of the three axes of one frame w.r.t. each of the three of the other. The DCM is connected to quaternions through the following relations:

$$DCM = \begin{bmatrix} q_0^2 + q_1^2 - q_2^2 - q_3^2 & 2\,(q_1\,q_2 - q_0\,q_3) & 2\,(q_1\,q_3 + q_0\,q_2) \\ 2\,(q_1\,q_2 + q_0\,q_3) & q_0^2 - q_1^2 + q_2^2 - q_3^2 & 2\,(q_2\,q_3 - q_0\,q_1) \\ 2\,(q_1\,q_3 - q_0\,q_2) & 2\,(q_2\,q_3 + q_0\,q_1) & q_0^2 - q_1^2 - q_2^2 + q_3^2 \end{bmatrix}$$

to get the DCM from a quaternion and

$$q_0 = \frac{1}{2}\sqrt{DCM_{1,1} + DCM_{2,2} + DCM_{3,3} + 1}$$

$$\boldsymbol{q} = \frac{1}{4\,q_0} \begin{bmatrix} DCM_{3,2} - DCM_{2,3} \\ DCM_{1,3} - DCM_{3,1} \\ DCM_{2,1} - DCM_{1,2} \end{bmatrix}$$

to get the quaternion from a DCM.

Appendix C

Simulink Blocks

The simulink model is here presented.

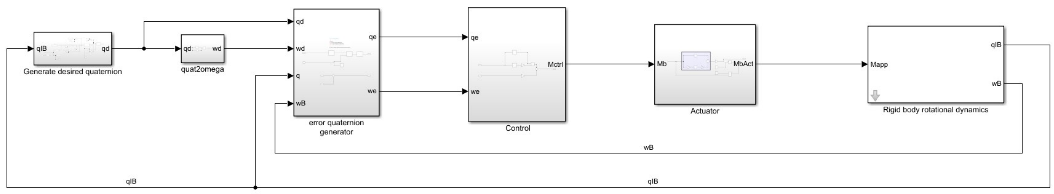

Figure C.1: Simulink model for the attitude control

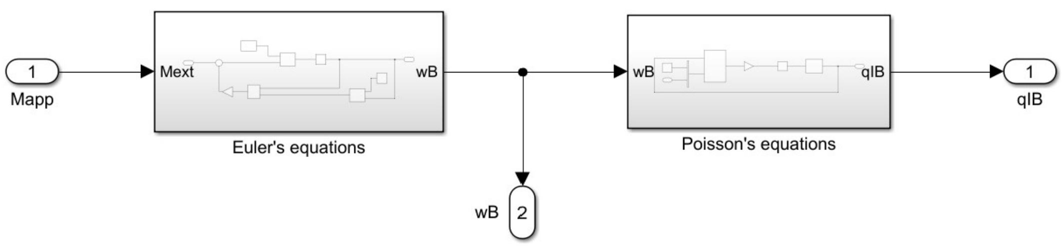

Figure C.2: Rigid body rotational dynamics block

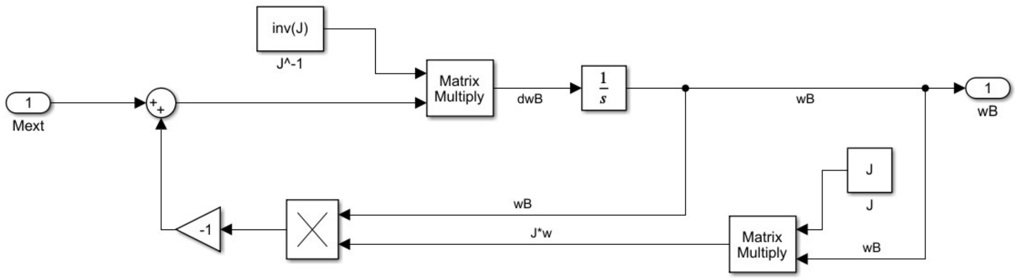

Figure C.3: Euler's equations block

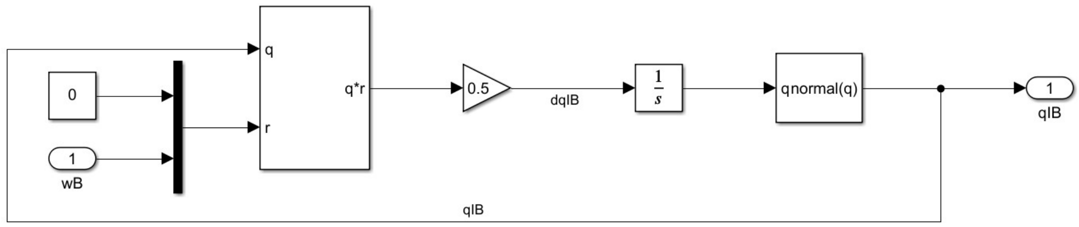

Figure C.4: Poisson's equations block

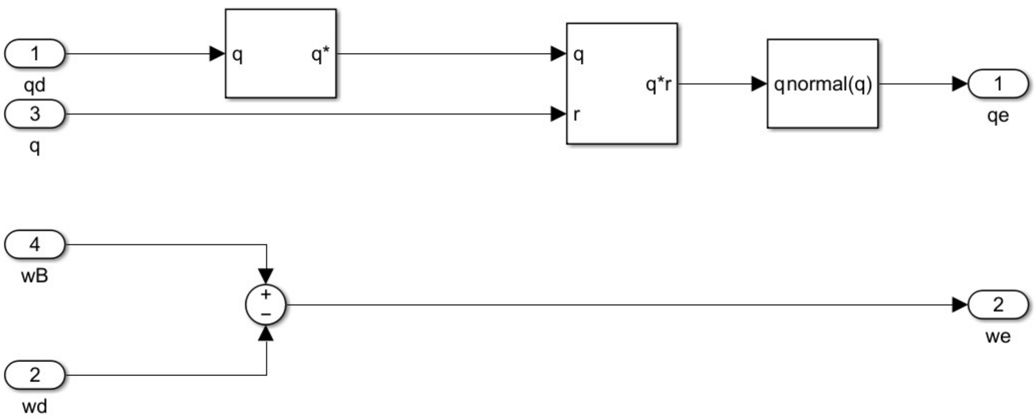

Figure C.5: Error - quaternion feedback control block

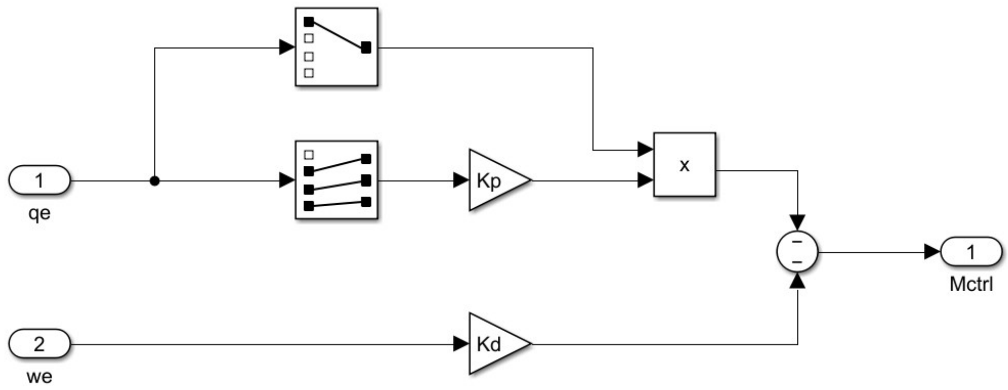

Figure C.6: Control block

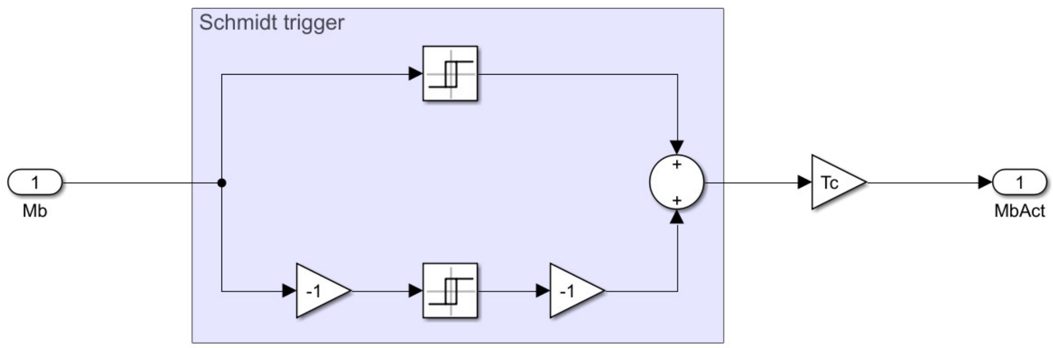

Figure C.7: Actuator block with Schmidt Trigger

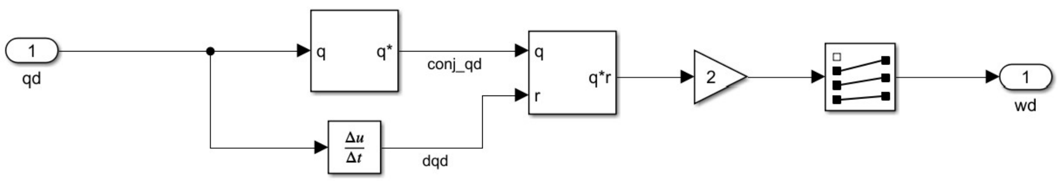

Figure C.8: Quaternions to angular velocity block

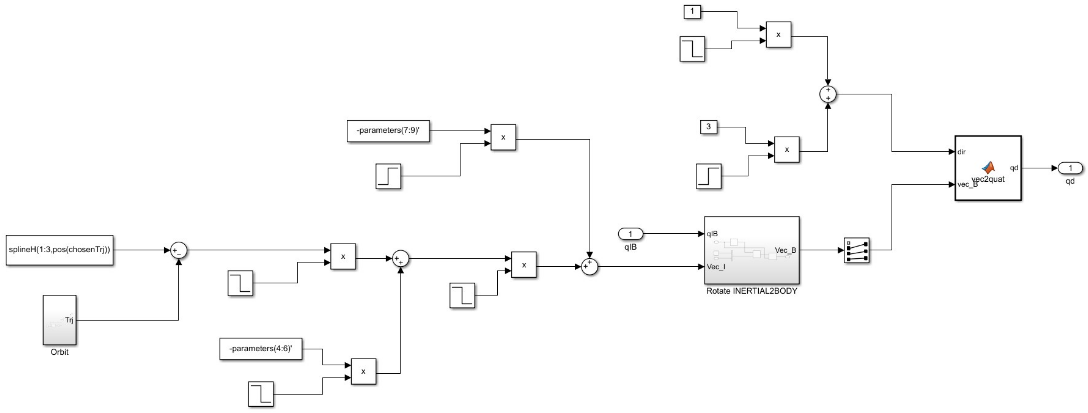

Figure C.9: Desired quaternion generation block. The orbit subsystem propagates the RdV manoeuvre, the rotate INERTIAL2BODY subsystem turns the desired attitude vector from the inertial to the body frame and the vec2quat function turns the vector into a quaternion

Bibliography

[1] JR Burton and WE Hayes. «Gemini rendezvous». In: *Journal of Spacecraft and Rockets* 3.1 (1966), pp. 145–147 (cit. on p. 1).

[2] Manny R Leinz, Chih-Tsai Chen, Peter Scott, William Gaumer, Peter Sabasteanski, and Michael Beaven. «Modeling, simulation, testing, and verification of the orbital express autonomous rendezvous and capture sensor system (arcss)». In: *Sensors and Systems for Space Applications II*. Vol. 6958. International Society for Optics and Photonics. 2008, p. 69580C (cit. on p. 1).

[3] Thomas V Peters, João Branco, Diego Escorial, Lorenzo Tarabini Castellani, and Alex Cropp. «Mission analysis for PROBA-3 nominal operations». In: *Acta Astronautica* 102 (2014), pp. 296–310 (cit. on p. 1).

[4] Simone D'Amico, J-S Ardaens, Gabriella Gaias, Heike Benninghoff, Benjamin Schlepp, and JL Jørgensen. «Noncooperative rendezvous using angles-only optical navigation: system design and flight results». In: *Journal of Guidance, Control, and Dynamics* 36.6 (2013), pp. 1576–1595 (cit. on p. 2).

[5] Jean-Sébastien Ardaens and Gabriella Gaias. «Angles-only relative orbit determination in low earth orbit». In: *Advances in Space Research* 61.11 (2018), pp. 2740–2760 (cit. on p. 2).

[6] Jean-Sébastien Ardaens and Gabriella Gaias. «Flight demonstration of spaceborne real-time angles-only navigation to a noncooperative target in low earth orbit». In: *Acta Astronautica* 153 (2018), pp. 367–382 (cit. on p. 2).

[7] Gabriella Gaias and Jean-Sébastien Ardaens. «Flight demonstration of autonomous noncooperative rendezvous in low earth orbit». In: *Journal of Guidance, Control, and Dynamics* 41.6 (2018), pp. 1337–1354 (cit. on pp. 2, 57).

[8] Sumant Sharma, Jacopo Ventura, and Simone D'Amico. «Robust model-based monocular pose initialization for noncooperative spacecraft rendezvous». In: *Journal of Spacecraft and Rockets* 55.6 (2018), pp. 1414–1429 (cit. on p. 3).

[9] JM Rebordão. «Space optical navigation techniques: an overview». In: *8th Iberoamerican Optics Meeting and 11th Latin American Meeting on Optics, Lasers, and Applications.* Vol. 8785. International Society for Optics and Photonics. 2013, 87850J (cit. on p. 3).

[10] Josep Virgili Llop. «Autonomous optical navigation for orbits around Earth–Moon collinear libration points». In: *Acta Astronautica* 86 (2013), pp. 119–125 (cit. on p. 3).

[11] Andrew Ogilvie, Justin Allport, Michael Hannah, and John Lymer. «Autonomous satellite servicing using the orbital express demonstration manipulator system». In: *Proc. of the 9th International Symposium on Artificial Intelligence, Robotics and Automation in Space (i-SAIRAS'08).* 2008, pp. 25–29 (cit. on p. 4).

[12] Juergen Telaar, Stephane Estable, Marco De Stefano, Wolfgang Rackl, Roberto Lampariello, Finn Ankersen, and J Gil Fernandez. «Coupled control of chaser platform and robot arm for the e. deorbit mission». In: *10th Int. ESA conference on Guidance Navigation and Control Systems (GNC), May 2017.* 2017 (cit. on p. 4).

[13] David Folta, Steven Cooley, Kathleen Howell, and Frank H Bauer. «Trajectory design strategies for the NGST L2 libration point mission». In: *Space Flight Mechanics.* 2001 (cit. on p. 5).

[14] David C Folta and Cassandra Webster. «Transfer trajectory options for servicing Sun-Earth-Moon libration point missions». In: *Proc. 29th AAS/AIAA Space Flight Mech. Meeting.* 2019 (cit. on p. 5).

[15] Kuljit Mand. «Rendezvous and proximity operations at the Earth-Moon L2 Lagrange point: navigation analysis for preliminary trajectory design». PhD thesis. 2014 (cit. on pp. 5, 43).

[16] Victory Szebehely. *Theory of orbit: The restricted problem of three Bodies.* Elsevier, 2012 (cit. on p. 10).

[17] ESA. *Herschel.* 2021. URL: `https://sci.esa.int/web/herschel/-/34682-summary` (visited on 09/27/2021) (cit. on p. 12).

[18] Martin Hechler and Jordi Cobos. «Herschel, Planck and Gaia orbit design». In: *Libration Point Orbits and Applications.* World Scientific, 2003, pp. 115–135 (cit. on pp. 13, 33).

[19] GL Pilbratt et al. «Herschel Space Observatory-An ESA facility for far-infrared and submillimetre astronomy». In: *Astronomy & Astrophysics* 518 (2010), p. L1 (cit. on p. 13).

[20] NASA. *Moon to Mars.* 2021. URL: `https://www.nasa.gov/specials/artemis/` (visited on 09/29/2021) (cit. on pp. 17, 18, 20).

[21] Allison Zuniga, Hemil Modi, Aurelio Kaluthantrige, and Heloise Vertadier. «Building an Economical and Sustainable Lunar Infrastructure to Enable Human Lunar Missions». In: *International Astronautical Congress (cited on p. 6)*. 2019 (cit. on pp. 19, 21).

[22] NASA. *Gateway*. 2021. URL: `https://www.nasa.gov/gateway/overview` (visited on 09/29/2021) (cit. on p. 19).

[23] Ian A Crawford. «Lunar resources: A review». In: *Progress in Physical Geography* 39.2 (2015), pp. 137–167 (cit. on p. 21).

[24] ESA. *Lunar resources*. 2021. URL: `https://www.esa.int/ESA_Multimedia/Images/2019/10/Oxygen_and_metal_from_lunar_regolith` (visited on 09/29/2021) (cit. on p. 23).

[25] NASA. *Spice*. 2021. URL: `https://naif.jpl.nasa.gov/naif/index.html` (visited on 12/12/2021) (cit. on p. 24).

[26] NASA. *cspicespkezr*. 2017. URL: `https://naif.jpl.nasa.gov/pub/naif/toolkit_docs/IDL/icy/cspice_spkezr.html` (visited on 01/04/2022) (cit. on pp. 27, 83).

[27] Davide Conte and David B Spencer. «Preliminary study on relative motion and rendezvous between spacecraft in the restricted three-body problem». In: *26th AAS/AIAA Space Flight Mechanics Meeting*. 2016 (cit. on p. 39).

[28] Benjamin Francois Villac. *Dynamics in the Hill problem with applications to spacecraft maneuvers*. University of Michigan, 2003 (cit. on p. 42).

[29] NASA. *rdvstandards*. 2019. URL: `https://nasasitebuilder.nasawestprime.com/wp-content/uploads/sites/45/2019/09/rendezvous_baseline_final_3-2019.pdf` (visited on 03/15/2022) (cit. on p. 51).

[30] G Fraser-Andrews. «A multiple-shooting technique for optimal control». In: *Journal of Optimization theory and Applications* 102.2 (1999), pp. 299–313 (cit. on p. 53).

[31] Andrea Colagrossi and Michèle Lavagna. «Dynamical analysis of rendezvous and docking with very large space infrastructures in non-Keplerian orbits». In: *CEAS Space Journal* 10.1 (2018), pp. 87–99 (cit. on p. 65).

[32] Nalin A Chaturvedi, Amit K Sanyal, and N Harris McClamroch. «Rigid-body attitude control». In: *IEEE control systems magazine* 31.3 (2011), pp. 30–51 (cit. on p. 65).

[33] Bong Wie, Haim Weiss, and Ari Arapostathis. «Quarternion feedback regulator for spacecraft eigenaxis rotations». In: *Journal of Guidance, Control, and Dynamics* 12.3 (1989), pp. 375–380 (cit. on p. 68).

[34] arianegroup. *thrusters*. 2002. URL: `https://www.space-propulsion.com/spacecraft-propulsion/hydrazine-thrusters/20n-hydrazine-thruster.html` (visited on 02/17/2022) (cit. on p. 68).

[35] Bong Wie. *Space Vehicle Guidance, Control and Astrodynamics*. American Institute of Aeronautics and Astronautics, Inc., 2015 (cit. on p. 69).